ORIENTATIONAL ORDERING IN SOLID METHANE AT LOW TEMPERATURES

ORIENTATIONAL ORDERING IN SOLID METHANE AT LOW TEMPERATURES

By

MARY ANNE WHITE, B.Sc.

A Thesis

Submitted to the School of Graduate Studies

in Partial Fulfilment of the Requirements

for the Degree

Doctor of Philosophy

McMaster University

November 1979

DOCTOR OF PHILOSOPHY (1979)
(Chemistry)

McMASTER UNIVERSITY
Hamilton, Ontario

TITLE: Orientational Ordering in Solid Methane at Low Temperatures

AUTHOR: Mary Anne White, B.Sc. (University of Western Ontario)

SUPERVISOR: Professor J. A. Morrison

NUMBER OF PAGES: xvii, 184

ABSTRACT

The solid isotopic methanes (CH_nD_{4-n}, $0 \leq n \leq 4$) are known to exist in at least three solid phases, called phases I, II and III in order of decreasing temperature domain. There have been many studies, both experimental and theoretical, of the properties of solid methane, and the structures of phases I and II are known. In phase I, the molecules form a face-centred cubic lattice, and are freely, or nearly freely, rotating on the lattice sites. In phase II, the solid has a complex sublattice structure: 3/4 of the molecules are orientationally ordered and 1/4 are orientationally disordered. The structure of phase III is not known, and one of the main aims of this thesis is to draw conclusions about the orientational order in this phase.

The heat capacities of isotopically purified CH_2D_2, CHD_3 and CD_4 were measured accurately in the temperature range $0.15K \leq T \leq 3.5K$ where Schottky anomalies were known to occur in the partially deuterated methanes. From the heat capacity measurements, the residual entropies at T = 0K of CH_2D_2 and CHD_3 were determined, and used to deduce that phase III is not classically orientationally ordered, and that it must contain at least three different sublattices. The latter conclusion is in agreement with that of recent theoretical calculations

and optical measurements on solid methane. A model is presented which accounts for the low temperature thermal properties of the solids.

Nuclear spin symmetry species conversion is known to occur in CH_4 and CH_3D but the present measurements show that it is not significant in CH_2D_2 or CHD_3. In CD_4 on the other hand, longer thermal relaxation is found and it may be ascribable to conversion.

The positions and shapes of the Schottky anomalies in the deuterated methanes are used to make estimates of the tunnel level splittings; these results are compared with those of recent neutron inelastic scattering experiments for CD_4, and with theoretical estimates for all of the deuterated methanes.

In a different type of experimental investigation, the relationship between the temperatures of the solid-solid phase transitions and thermally-stimulated luminescence of electron- and ultraviolet-irradiated methane (CH_4 and CD_4) was probed. Under certain conditions, a correlation was found to exist between the phase transition temperatures and sharp peaks in the glow curves, but thermal gradients in the samples preclude the use of this method for kinetic analysis of the phase transitions.

ACKNOWLEDGEMENTS

It gives me great pleasure to express my sincere gratitude to Professor J. A. Morrison, who introduced me to the subject of molecular solids. His great enthusiasm for science and scientific endeavours has been a constant source of inspiration.

Several others have shared an interest in the problems of solid methane, and have contributed many valuable comments throughout the course of this investigation. In particular, I would like to thank Drs. R. F. Code, J. H. Colwell, A. Hüller, M. L. Klein, K. Maki, S. F. O'Shea and W. Press and Professor T. Yamamoto in this regard. I would also like to thank Professor F. Bruner for the kind loan of his chromatographic column and Professor A. G. Harrison for the mass spectrometric analyses of CH_2D_2 and CHD_3, and Professor E. A. Ballik for his continued interest in this project.

For their friendship and advice, I would like to thank my physical chemistry colleagues, especially Troy Lassau, Dr. Ken Lushington and Dr. Tom Ryan. I would particularly like to thank Tom for his advice on radiation chemistry and for the construction of the electron gun.

Thanks also to Mr. Bill Scott for a steady supply of liquid helium, and to Mrs. Marilyn Foster for her fast and accurate typing of this thesis.

I acknowledge, with thanks, the financial support of the National Science and Engineering Research Council through a postgraduate award.

As an organic chemist, my husband, Rob, has been a constant (and appreciated) partner for many discussions. His companionship has made the path seem shorter and the load lighter.

Finally, throughout my life, my family and many of my teachers, co-workers and friends have created an atmosphere that is conducive to scientific thought. I dedicate this thesis to them, and to the pursuit of scientific knowledge.

TABLE OF CONTENTS

		Page
Chapter I	Intermolecular Forces in Molecular Solids	1
Chapter II	Solid Methane: An Introduction	23
Part A	Experimental Observations on Solid Methane	23
1	The Phase Diagram	23
2	Physical Properties of Solid Methane	26
	(a) Phase I	26
	(b) Phase II	30
	(c) Phase III	33
Part B	Theoretical Studies of Solid Methane	38
1	The James and Keenan (JK) Theory	38
2	Quantum Mechanical Investigations	40
	(a) Further Work Based on the JK Model	40
	(b) Extended James and Keenan (EJK) Model	44
	(c) Extension of the EJK Model to Phase III	47
Chapter III	Thermodynamic Studies of the Solid Deuterated Methanes	54
Part A	Experimental	54
1	Sample Preparation	54
	(a) Isotopic Purification	54
	(b) Sample Analysis	62
	(c) Further Purification	62

Chapter III			
Part A			
	2	Calorimetry	65
		(a) The Calorimetric Vessel	65
		(b) Thermometry and Temperature Measurement	68
		(c) Mounting of the Calorimeter Vessel	70
		(d) Measurement Techniques and Error Analysis	72
Part B		Results	73
	1	CH_2D_2	73
	2	CHD_3	78
	3	CD_4	83
Chapter IV		Deductions About the Structure of Phase III and Tunneling States in the Solid Isotopic Methanes	94
Part A		Low Temperature Entropy and Ordering in the Solid Methanes	94
	1	The Lattice Contribution to the Entropy	94
	2	The Entropy as a Function of Temperature for the Partially Deuterated Methanes	98
	3	The Energy Levels of the Deuterated Methanes in Hindering Potential Fields	103
	4	Nuclear Spin Symmetry Species Conversion in the Partially Deuterated Methanes	109
	5	The Structure of Phase III	112
Part B		Low-Lying Energy Levels in the Solid Methanes	119

Chapter IV

Part C Future Investigations 126

Chapter V An Experimental Study of Methane Thermoluminescence Near the Solid-Solid Phase Transitions 130

Part A Introduction 130

Part B Experimental 135

1 Sample Purity and Preparation 135

2 The Apparatus 136

(a) The Cryostat 136

(i) General Features 136

(ii) The Sample Deposition Port 140

(iii) Thermometry and Temperature Control of the Sample Block 140

(b) The Irradiation Sources 142

(i) The Electron Gun 142

(ii) Irradiation with Ultraviolet Light 144

(c) Light Detection 145

Part C Results and Discussion 145

1 The Isothermal Luminescence 146

(a) The Short-Lived Process 148

(b) The Long-Lived Process 148

2 Thermoluminescence 151

(a) Electron Bombardment 151

(b) Results from UV-Irradiation 152

Chapter V

Part C

2 (b)

(i) The Isothermal Decay Time 152

(ii) Warming Rates 154

(iii) The Effect of Sample Size 154

(iv) Solute Concentrations 157

(v) The Effect of Sample Deposition Rate 158

(vi) Sample Annealing 158

(vii) The Effect of the Solute on the Glow Curves 158

(c) Discussion of the Thermoluminescence Results 165

Chapter VI Summary 171

References 173

LIST OF FIGURES

Figure		Page
1	The interaction between two molecules, A and B	2
2	The interaction of molecule A with molecules B and C	10
3	Ar-Ar potential energy as a function of interatomic separation	12
4	The interaction of a fixed diatomic molecule with a rotating diatomic molecule	16
5	Pocket states for a fourfold rotational potential	20
6	Molecular energy levels of a tetrahedron in a tetrahedral potential	22
7	The phase diagram of solid CH_4	27
8	The phase diagram of solid CD_4	28
9	The structure of phase II of solid methane	31
10	The heat capacities of the deuterated methanes for $T \geq 0.3K$	36
11	The calculated energy levels for phase II of CH_4	48
12	The theoretically proposed structure of phase III as it arises from phase II	51
13	A schematic representation of the gas chromatograph	56
14	Van Deemter plot for CH_4 chromatographic separation	58

Figure		Page
15	The chromatographic separation of CH_2D_2	61
16	The chromatographic separation of CHD_3	63
17	The chromatographic separation of CD_4	64
18	The calorimeter vessel	66
19	The heat capacity of pure CH_2D_2	77
20	The heat capacity of pure CHD_3	84
21	The heat capacity of CD_4	90
22	Thermal relaxation times in CD_4	93
23	C/RT^3 vs T^2 for CD_4	97
24	The low-temperature entropy of CH_2D_2	101
25	The low-temperature entropy of CHD_3	102
26	The energy levels of CH_3D in different molecular fields	104
27	The energy levels of CH_2D_2 in different molecular fields	105
28	The energy levels of CHD_3 in different molecular fields	106
29	The energy levels of CD_4 in different molecular fields	107
30	Model of the tunneling states in CHD_3	120
31	The comparison of the observed and calculated heat capacity of CHD_3	121
32	The Schottky tail in CD_4	125
33	The thermoluminescence cryostat	137
34	The tail of the thermoluminescence cryostat in cross-section	139

Figure		Page
35	A typical heating curve for a thermo-luminescence sample	143
36	The decay of isothermal luminescence	147
37	The isothermal decay of the short-lived luminescence	149
38	The isothermal decay of the long-lived luminescence	150
39	The effect of the isothermal luminescence decay time on the glow curve	153
40	The glow curve for two different heating rates	155
41	The effect of the sample size and solute concentration on the glow curve	156
42	The effect of the sample deposition rate on the glow curve	159
43	The glow curve before and after annealing at T = 40K	160
44	The glow curve of CH_4/benzene	162
45	The glow curve of "impure" CD_4/benzene	163
46	The glow curve of "purified" CD_4/benzene	164

LIST OF TABLES

Table		Page
I	Contributions to the interaction energy between like polar molecules	8
II	Categorization of some molecular solids based on their intra- and intermolecular parameters	17
III	Phase transition temperatures and melting points of the isotopic methanes	24
IV	Comparison of calculated and experimental properties of CH_4	42
V	Comparison of calculated and experimental properties of CD_4	46
VI	Temperature dependence of tunneling levels of D_{2d} molecules in CH_4	49
VII	Compositions of methane samples	60
VIII	Measured heat capacities of CH_2D_2	74
IX	Smoothed values of the heat capacity of pure CH_2D_2	79
X	Measured heat capacities of CHD_3	80
XI	Smoothed values of the heat capacity of pure CHD_3	85
XII	Measured heat capacities of CD_4	86
XIII	Smoothed values of the heat capacity of pure CD_4	91

Table		Page
XIV	Derived entropies for the partially deuterated methanes	99
XV	Comparison of calculated and experimental values of S^{8}_{o}	110
XVI	Comparison of calculated and experimental values of residual entropies	110
XVII	Proposed 3-site model for phase III	117

LIST OF SYMBOLS

(in order of appearance)

R	intermolecular separation
H	Hamiltonian operator
Ψ	wave function
Φ	total interaction energy
ϕ^{AB}_{elec}	electrastatic energy of interaction for molecules A and B
ϕ^{AB}_{ind}	induction energy of interaction for molecules A and B
ϕ^{AB}_{disp}	dispersion energy of interaction for molecules A and B
I_A	ionization energy of molecule A
α_A	polarizability of molecule A
E	internal energy
U_o	depth of potential well on changing R
V_o	depth of potential well on change of orientation
B	rotational constant
I	moment of inertia
$\hbar$	Plank's constant/2π
T	temperature (in Kelvin)
P	pressure

C_p	heat capacity at constant pressure
C_v	heat capacity at constant volume
C_{sat}	heat capacity under saturated vapour
J	rotational quantum number
HETP	height equivalent to theoretical plates
R	resistance (in Ohms)
h	thermal conductance
τ	thermal relaxation time
Θ	Debye temperature
R	gas constant
S	entropy
S_o	entropy as extrapolated T = 0K
S_o^8	S_o from data for $T \geq 8K$
$S_o^{0.15}$	S_o from data for $T \geq 0.15K$
A,B,E,T	group theoretical symbols for rotational degeneracy of tunneling levels
I	nuclear spin
δ	energy level splitting
I	luminescence intensity
t	time (sec.)

CHAPTER I

INTERMOLECULAR FORCES IN MOLECULAR SOLIDS

Intermolecular forces and the potential energies of intermolecular interactions play a primary role in the determination of the physical properties of solids. In the case of molecular solids, that is solids in which the intramolecular forces are stronger than the intermolecular forces, and in which distinct molecular units are retained in the solid state, the forces between the molecules can lead to many varied and interesting properties. An understanding of the origin of the physical characteristics can only come from a knowledge of the dominant intermolecular forces.

Although it is a somewhat arbitrary division, it is convenient to consider intermolecular forces in two extremes: long-range forces and short-range forces. The long-range forces between two molecules will be examined first.

If two molecules, A and B, are composed respectively of charges $e_i^{(A)}$ and $e_j^{(B)}$ at distances $r_i^{(A)}$ and $r_j^{(B)}$ from their molecular centres, and the distance between $e_i^{(A)}$ and $e_j^{(B)}$ is r_{ij} and that between the molecular centres is R, as shown in Figure 1, then the interaction Hamiltonian H_{AB}, is given by[1]:

$$H_{AB} = \sum_i^A \sum_j^B \frac{e_i^{(A)} e_j^{(B)}}{r_{ij}} . \qquad (1)$$

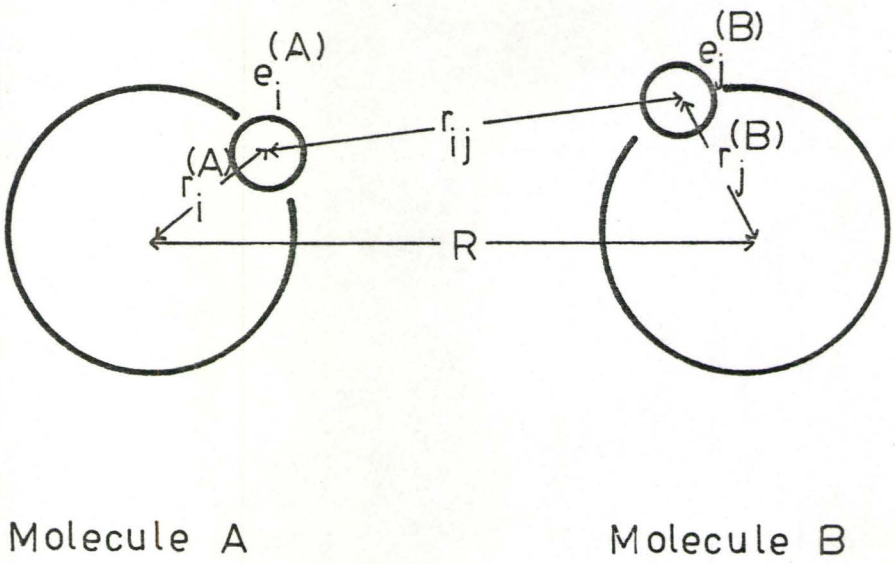

Figure 1: The Interaction Between Two Molecules, A and B.

r_{ij} can be expressed in terms of $r_i^{(A)}$, $r_j^{(B)}$ and R, and, for large intermolecular separation ($R >> r_i^{(A)}$ and $R >> r_j^{(B)}$, i.e no charge overlap between the molecules), the expression for H_{AB} can be expanded as a power series in R to yield[1]:

$$H_{AB} = \frac{q^{(A)}q^{(B)}}{R} + (q^{(A)}\mu^{(B)} - q^{(B)}\mu^{(A)})\ \nabla\ (R^{-1})$$

$$- \mu^{(A)}\mu^{(B)}\ \nabla^2\ (R^{-1}) - \frac{1}{3}\ (\mu^{(A)}\Theta^{(B)} - \mu^{(B)}\Theta^{(A)})\ \nabla^3\ (R^{-1})$$

$$+ \frac{1}{9}\ \Theta^{(A)}\ \Theta^{(B)}\ \nabla^4\ (R^{-1}) + \ldots \qquad (2)$$

where $q^{(A)}$ = total charge on molecule A = $\sum_i^A e_i^{(A)}$, $\mu^{(A)}$ = dipole moment of A = $\sum_i^A e_i^{(A)}\ r_i^{(A)}$ and $\Theta^{(A)}$ = quadrupole moment of A = $\sum_i^A e_i^{(A)}\ r_i^2$. ($q^{(B)}$, $\mu^{(B)}$ and $\Theta^{(B)}$ are similarly defined for molecule B.) It should be noted that H_{AB} has the following form:

$$H_{AB} = \text{charge-charge} + \text{charge-dipole} +$$
$$\text{dipole-dipole} + \text{dipole-quadrupole} +$$
$$\text{quadrupole-quadrupole} + \text{quadrupole-octopole} + \ldots \qquad (3)$$

The first non-zero term in H_{AB} depends on the specific interacting molecules: for example, the leading term is charge-charge for NH_4^+ - NH_4^+ interactions, dipole-dipole for HCℓ-HCℓ, quadrupole-quadrupole for N_2-N_2, octopole-octopole for CH_4-CH_4, and so on.

When the free molecules, A and B, have stationary states represented by Ψ_{r_A} and Ψ_{r_B} respectively, and H_{AB} is considered as a perturbation on the separated molecular energies, W_{n_A} and W_{n_B}, the total long-range energy of the interacting system, $\Phi^{\ell r}_{AB}$, is[2]:

$$\Phi^{\ell r}_{AB} = W_{n_A} + W_{n_B} + \langle n_A n_B \mid H_{AB} \mid n_A n_B \rangle + \sum_{p_A, q_B}{}' \frac{\langle p_A q_A \mid H_{AB} \mid n_A n_B \rangle^2}{W_{n_A} - W_{p_A} + W_{n_B} - W_{p_B}} + \ldots \qquad (4)$$

where the $\sum'$ indicates that the sum is for all p_A and q_B such that $p_A \neq q_B$. The first two terms in the series are the free molecule energies. The next term (the first order perturbation energy) is the electrostatic interaction energy, ϕ^{AB}_{elec}. The following term (the second order perturbation energy) includes both the induction energy, ϕ^{AB}_{ind}, and the dispersion energy, ϕ^{AB}_{disp}.

The electrostatic interaction energy is that due to the permanent electric moments of molecules A and B; such charge-charge interactions vary as R^{-1}, charge-dipole as R^{-2}, dipole-dipole as R^{-3}, dipole-quadrupole as R^{-4}, quadrupole-quadrupole as R^{-5}, and so on[1]. The ϕ^{AB}_{elec} can be either repulsive or attractive; this depends on the particular molecules involved.

The induction energy, ϕ_{ind}^{AB}, is[1]:

$$\phi_{ind}^{AB} = - \sum_{p_A, n_A}' \frac{\langle n_A n_B \mid H_{AB} \mid p_A n_B \rangle^2}{W_{p_A} - W_{n_A}} - \sum_{q_B, n_B}' \frac{\langle n_A n_B \mid H_{AB} \mid n_A q_B \rangle^2}{W_{q_B} - W_{n_B}} \qquad (5)$$

and represents the energy due to induction of a multipole moment in one molecule by the permanent charge distribution of the other. At large intermolecular separations,

$$\phi_{ind}^{AB} = -\frac{1}{2} (\alpha_A F_A^2 + \alpha_B F_B^2) \qquad (6)$$

where α_A is the polarizability of molecule A, F_A is the electric field at molecule A as a result of the permanent charge distribution of molecule B, and $\alpha_A F_A$ is the induced dipole moment of molecule A; α_B, F_B and $\alpha_B F_B$ are similarly defined in terms of molecule B.[3] The polarizability of molecules in their ground electronic states is positive and, therefore, the induction energy is negative. This is also true at shorter intermolecular separations where induced quadrupoles and higher moments have significant contributions, since the reduction of the total energy is always the driving force for the distortion of the molecular charge distribution.

Through a perturbation approach, the dispersion energy can be written as[1]:

$$\phi^{AB}_{disp} = - \sum_{\substack{p_A, n_A \\ q_B, n_B}}{}' \frac{\langle n_A n_B \mid H_{AB} \mid p_A q_B \rangle^2}{W_{p_A} - W_{n_A} + W_{q_B} - W_{n_B}} \quad . \qquad (7)$$

The source of the dispersion (or London) energy is the induction of a multipole moment in one molecule as a result of the instantaneous charge distribution of the other molecule. Unlike the electrostatic and induction energies, which can be understood in terms of classical mechanics, the dispersion energy is a quantum mechanical property of the system.

The dispersion energy can be written in terms of R as[4]:

$$\phi^{AB}_{disp} = - \frac{C_6}{R^6} + \frac{C_7}{R^7} + \ldots \quad , \qquad (8)$$

and semi-empirical techniques have been used to evaluate C_6 for simple molecules[5]. At larger intermolecular separations, the angular dependent term in R^{-7} becomes negligible[3], and London[6] deduced a useful approximation for C_6 such that:

$$\phi^{AB}_{disp} = - \frac{3}{2} \frac{1}{(4\pi\varepsilon_o)^2} \frac{I_A I_B}{I_A + I_B} \frac{\alpha_A \alpha_B}{R^6} \quad , \qquad (9)$$

where I_A and I_B are the ionization energies of molecules A and B, α_A and α_B are again the polarizabilities of A and B, and ε_o is the permittivity of free space ($4\pi\varepsilon_o$ = 1.1126497 x 10^{-10} C $V^{-1}m^{-1} \equiv$ 1 e.s.u.[7])

It is useful to compare the magnitudes of ϕ_{elec}, ϕ_{ind} and ϕ_{disp} for various pairs of molecules. In inert gas interactions, the electrostatic and inductive energies are zero, and the dispersive forces are the complete source of long-range interatomic attraction. Each of the interactions between like symmetric molecules has its lead term in R^{-6}, and one therefore need only compare the coefficients of the terms to see the relative contributions[8]. Such a comparison is given in Table I for the interactions between like dipolar molecules[6]. It is apparent that for neutral molecules the electrostatic and dispersion contributions to the energy are much greater than that due to induction yet, even for molecules with large dipole moments and especially for non-polar molecules such as CH_4, the dispersion energy makes a significant contribution to the total interaction energy.

Thus far, only the long-range intermolecular forces have been considered. As the molecules approach each other more closely, there is significant overlap between the electron clouds of the different molecules, and intermolecular electron exchange must be considered. The general approach that was used to understand the long-range interaction energy was feasible because the interaction can be treated as a perturbation of the separated atoms. Such is not the case for the short-range forces where the interaction is intermediate between the united

Table I

Contributions to the Interaction Energy Between Like Polar Molecules at T=293K[7]

	$\phi_{elec} \times R^6$ (10^{-60}erg cm^6)	$\phi_{disp} \times R^6$ (10^{-60}erg cm^6)	$\phi_{ind} \times R^6$ (10^{-60}erg cm^6)
CO	0.0034	67.5	0.057
HI	0.35	382	1.68
HBr	6.2	176	4.05
HCℓ	18.6	105	5.4
NH_3	84	93	10
H_2O	190	47	10

and separated molecule limits. For this reason, the energies of short-range interactions are usually calculated specifically for the molecules involved. Several approaches have been taken[4,8]; here it will suffice to mention that the short-range repulsive forces are often represented by a term in R^{-12} or (better) by a term in exp (-aR), or by combinations of the two[8]. (Apart from its convenience in the expression of the short-range interaction, R has been shown[1] not to be a natural expansion parameter for the function.) It should be noted that the overlap energy may in principle be either positive or negative but, at small separations, repulsion invariably occurs.

The internal energy, E, of the solid can be calculated from the intermolecular interaction energy, Φ_{AB} as :

$$E = \sum_{A>B} \Phi_{AB} \quad , \qquad (10)$$

where the kinetic energy contributions have been ignored. More serious, however, is the inherent assumption that the intermolecular forces are additive. The electrostatic forces are exactly additive and the dispersion forces are nearly additive (the non-additive contribution to the dispersion force is small since it arises from third and higher order perturbation theory), but the inductive forces are clearly non-additive. Consider the simplified case of an atom, A, between two dipolar molecules, B and C, as shown in Figure 2. If only A and B were present, A would have an induced dipole

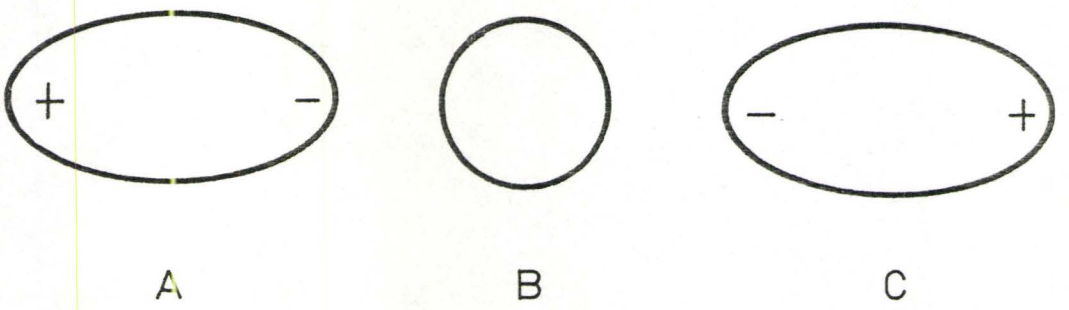

Figure 2: The Interaction of Molecule A with Molecules B and C. (See text for discussion of ϕ_{ind}.)

and the total energy would be lowered accordingly. In the presence of both B and C, A feels no net dipole, and there is no dipolar contribution to ϕ_{ind}. This is to be compared with a doubly reduced energy that additivity of ϕ_{ind} would predict. Since Axilrod and Teller's early calculation[9] of three-body forces, the nature and importance of many-body interactions have been the subject of much discussion[1].

In the past several years, very accurate interaction potentials have been composed for rare gas interactions. The example of an Ar-Ar potential[10] is shown in Figure 3. The form of the potential is:

$$U(x) = \varepsilon \{A\, x^{\gamma} \exp(-\alpha x) - (\frac{C_6}{x^6} + \frac{C_8}{x^8} + \frac{C_{10}}{x^{10}})\, F(x)\} \qquad (11)$$

$$\text{for } F(x) = \exp\left[-\left(\frac{D}{x} - 1\right)^2\right] \quad , x < D$$

$$\text{and } F(x) = 1 \quad , x \geq D \ .$$

Here, $x = r/r_m$ where r_m is the "equilibrium distance"[10]. The parameters ε, r_m, A, γ, α, C_6, C_8, C_{10} and D have variously been fitted to the absorption spectrum of Ar_2, the energy level spacings, the viscosity coefficient and an ab initio SCF short-range repulsive potential. The potential gives excellent agreement with the spectroscopic observations of Ar_2 and the second virial coefficient, viscosity, thermal conductivity, diffusion and thermal diffusion of solid Ar.[10]

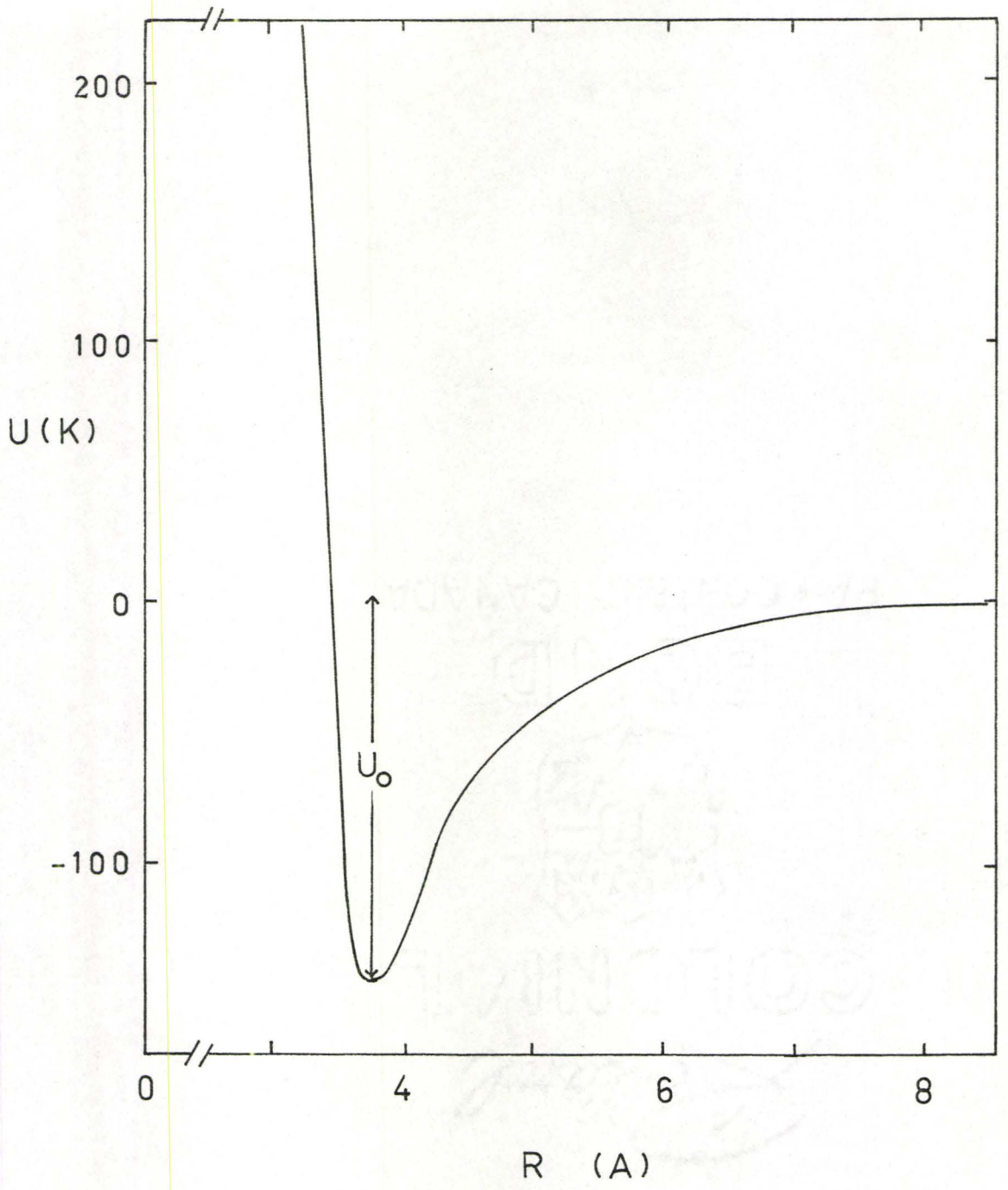

Figure 3: Ar-Ar Potential Energy, U, as a Function of Interatomic Distance, R. (Potential from Ref. 10.)

It is not as straightforward, however, to determine the interaction potential between two molecules, principally due to the complication of orientation-dependent contributions. For this reason, simplified models are usually chosen in order to calculate properties of molecular solids.

The dynamical structure of liquids and solids composed of molecules of spherical or nearly spherical symmetry has been considered in terms of a simple hard sphere model[11,12]. A model based on "rough hard spheres" (i.e. spheres which can undergo instantaneous interparticle collisions and thereby change the angular and translational momentum) has been used to calculate single-particle correlation functions in molecular liquids[13], and has provided a self-diffusion constant and shear viscosity coefficient for $CC\ell_4$ that is in good agreement with experiment[14].

Another approach that has been used to predict properties of molecular solids is the "atom-atom model". The model sums interactions between non-bonded atoms, and has major advantages over calculations based on the molecule as a whole: the atoms are isotropic and have nearly isotropic polarizabilities, even in their bonded states, and also the ratio of the particle size to the particle separation is more favourable for interatomic than for intermolecular interactions. The intermolecular (non-bonded) interactions are assumed to be additive such that Φ_{AB}, the potential energy of interaction for molecules A and B, is given by:

$$\Phi_{AB} = \sum_{i}^{A} \sum_{k}^{B} \phi_{ik} + \phi_{elec}^{AB} \qquad (12)$$

where ϕ_{ik}, the energy of interaction between atom i of molecule A and atom k of molecule B, is expressed as $(AR^{-6} - BR^{-12})$, or, more accurately, as $(AR^{-6} - B \exp(-R/\rho))$. The parameters A, B and ρ have been empirically determined for particular atom-atom interactions; much of the work for hydrocarbons has been carried out by Kitaigordskii[15] and Williams[16]. If A, B and ρ are considered to be universal for each atom-atom interaction, excellent agreement is found with the experimentally-determined properties of the solids. The list of the calculated properties is extensive and includes heats of sublimation, collisional linewidths, second virial coefficients, lattice dynamics, and molecular orientations and structure in the solid state[15].

A third approach which can correctly predict some properties of molecular solids is based on the assumption that molecular multipole moments give rise to the dominant forces in the solid. The method works best for long-range forces and has been successful, for example, in the case of a tetrahedral charge distribution (i.e. octopolar interaction) model of CD_4[17]. (The model will be discussed in detail in Chapter II.)

A qualitative understanding of properties of molecular solids can be gained through consideration of the relative magnitudes of the isotropic and the orientational-dependent

contributions to the interaction potential. Figure 4 illustrates the angular dependence of the anisotropic potential energy, V, in the simplified case of a rotating diatomic molecule interacting with another of fixed orientation. The relative magnitudes of the well-depths for the isotropic and anisotropic contributions to the potential energy (U_o and V_o as defined in Figures 3 and 4 respectively) play an important role in the determination of the physical properties of molecular solids. For $V_o << U_o$, the potential is dominated by the isotropic component, and the crystals may be "plastic" in nature. In other words, if sufficient thermal energy is available, the molecules will be orientationally disordered in the solid phase. (The term "orientationally disordered crystal" is now preferred over "plastic crystal" since the former is not restricted to solids that meet the Timmermans[18] definition of a plastic crystal, i.e. those solids with entropies of fusion $< 20 J K^{-1} mole^{-1}$. In addition, the term "rotational disorder" will be abandoned here in favour of "orientational disorder" since the latter term is not restricted to free or nearly free rotation in the solid.) For $V_o >> U_o$, the crystal may be "liquid", i.e. orientationally ordered and translationally disordered. In Table II, a few representative solids are categorized according to the relative strengths of their isotropic and anisotropic forces.

In this thesis, solids for which $V_o << U_o$ will be examined. At high temperatures, molecular solids with this

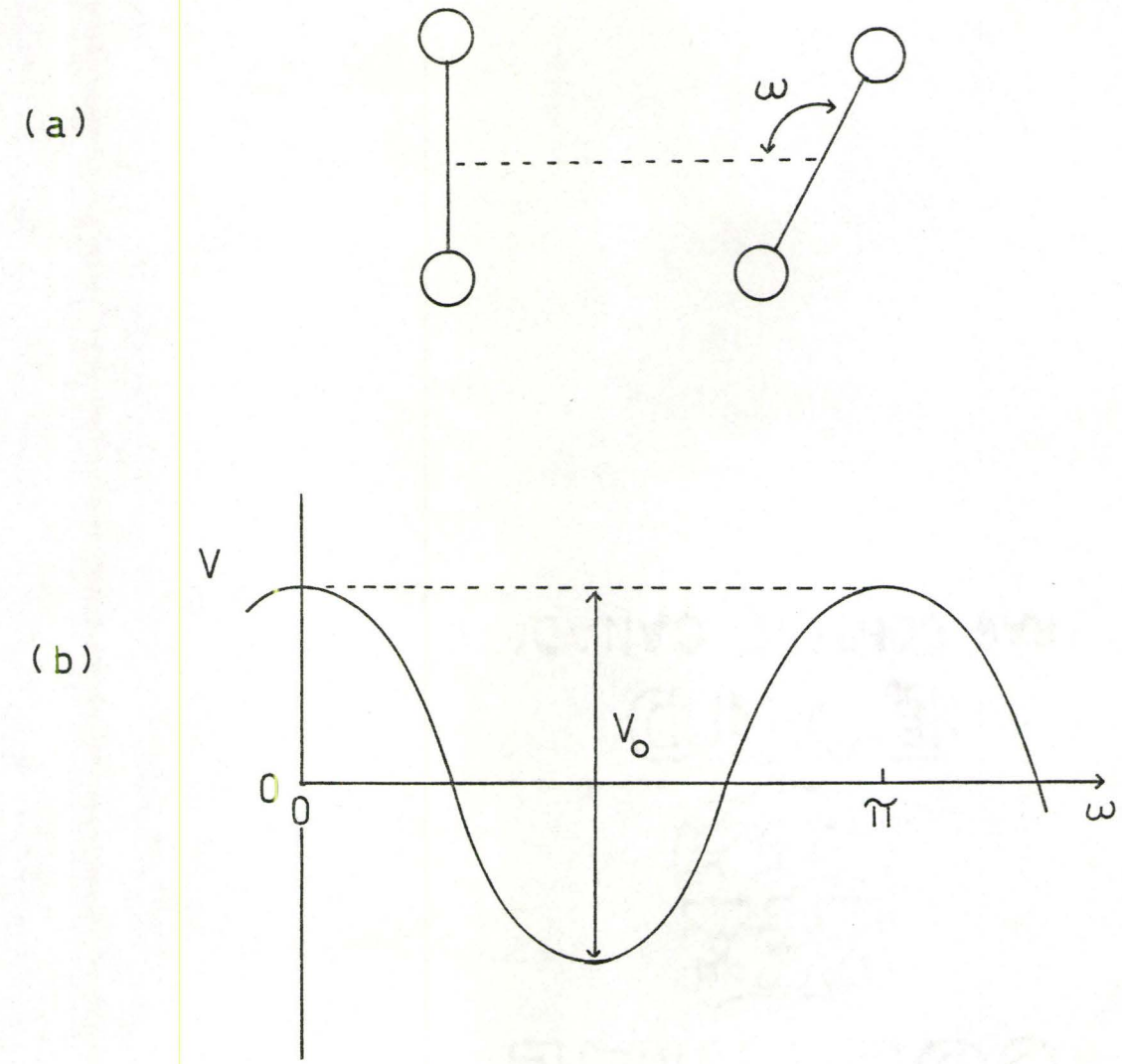

Figure 4: The Interaction of a Fixed Diatomic Molecule with a Rotating Diatomic Molecule.

(a) Orientation of the molecules.

(b) Potential energy, V, as a function of the orientation angle, ω.

Table II

Categorization of Some Molecular Solids Based on Their Intra- and Intermolecular Parameters

	$V_o << U_o$	$V_o \sim U_o$	$V_o >> U_o$
$B = \frac{\hbar^2}{2I}$ ↓	orientationally disordered crystals:		liquid crystals:
			$CH_3-(CH_2)_n-CO_2^- M^+$
		adamantane	
			DNA
		benzene	
	$CC\ell_4$	$CC\ell_3F$	
	F_2		
	O_2		
	NO	CO_2	
	CO		
	N_2		
	CD_4, ND_4^+		
	CH_4, NH_4^+		
		HI	
		HBr	
		HCℓ	
	D_2		
	H_2		

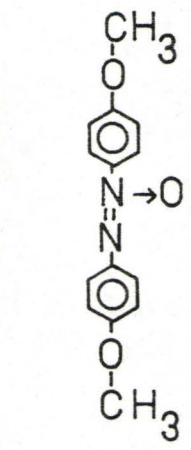

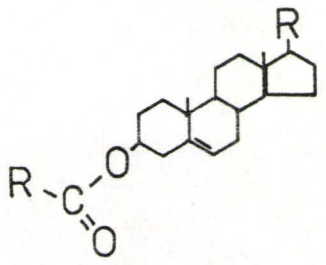

(R = alkyl chain)

characteristic exhibit behaviour that can be classified according to either the Frenkel[19,20,21] or the Pauling[22] pictures depending on the degree of orientational disorder. In the former case, molecules on lattice sites jump between several equilibrium orientations; these solids can be treated by an Ising model. In the latter case, the rotational motion of the molecules in the solid is similar to that in the liquid phase, and the molecules have an essentially classical, continuous rotational energy spectrum.

At lower temperatures where quantum effects dominate the solid and one must consider discrete energy levels in the solid, there are two extremes of orientational behaviour. If the orienting potential (V_o) is small in comparison with the rotational constant, B ($B = \hbar^2/2I$, where $\hbar$ = Plank's constant/2π and I = moment of inertia), then the molecules will be freely or nearly freely rotating. On the other hand, if V_o is much greater than B, the molecules will undergo small angular oscillations (called librations) about their equilibrium orientations. It is a straightforward matter[23,24] to calculate the energy levels and other properties of the molecules in either of the above extreme cases. In reality, however, many solids fall between these two extremes, as illustrated in Table II. In these intermediate cases, V_o is comparable to B in magnitude and the librational states are split by tunneling motion between different equilibrium orientations, as observed from calorimetric measurements[25], paramagnetic resonance[26],

phonon spectroscopy[27], neutron magnetic resonance[28] and inelastic neutron scattering[29,30].

A theoretical approach developed by Hüller[31] uses the variational method to provide molecular energy levels for the complete range of relative strengths of B and V_o. The method is based on the variational theorem[32]

$$\frac{\int \Psi^* H \Psi d\tau}{\int \Psi^* \Psi d\tau} \geq E_o \quad , \qquad (13)$$

where Ψ is a well-behaved function (called the trial wave function) that satisfies the boundary conditions of the problem, Ψ^* is the complex conjugate of Ψ, H is the Hamilton operator for the problem and E_o is the true value of the lowest energy eigenvalue of H. Higher energy levels (E_1, E_2, ...) can also be derived from the variational method.

Hüller uses appropriately-named "pocket" states as trial wave functions; the group of single-molecule wave functions describe the spatial energy minima, or pockets, of a system of interest. An illustration of the pocket states for a one-dimensional four-fold rotational potential is given in Figure 5. The wave functions are the correct free rotor wave functions in the limit of a vanishingly small orientational potential (V_o), and harmonic oscillator wave functions in the limit of strong orientational potentials. The width and depth of the pocket states are adjusted to match the particular potential. The calculations were carried out with

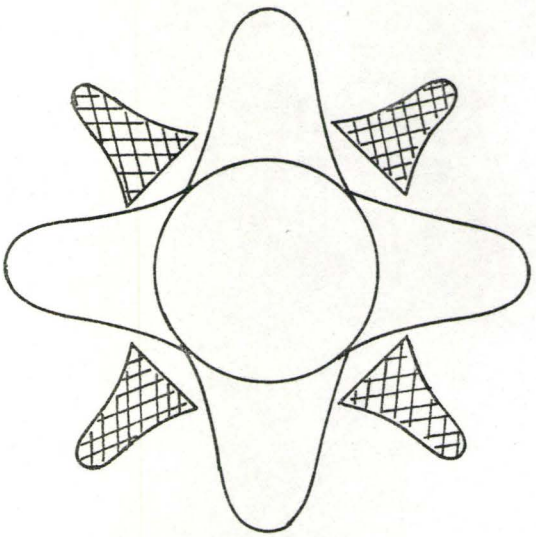

Figure 5: A Schematic Representation of the Pocket States for a 1-D Fourfold Rotational Potential. (The pocket state wavefunctions are represented by the cross-hatched areas, and the potential energy is represented by the solid line.)

a rotational Hamiltonian for molecules of 1, 2 or 3 degrees of rotational freedom, i.e. for molecules with 1 rotation axis, for dumbbell molecules and for spherical top molecules, and the calculation was simplified by the respective use of either circular functions, Kubic Harmonics, or cubic rotator functions, to take advantage of the symmetry of the problem. The total molecular wave function must be either totally symmetric or totally antisymmetric with respect to odd permutations of a given set of identical particles[33], and the proper symmetry for the total wave function was obtained from a linear combination of products of molecular electronic, vibrational, rotational, translational and nuclear spin wave functions. These quantum considerations lead, for example in solid hydrogen and solid methane, to different nuclear spin symmetry species of different energies.

The result of the Hüller theory is a unified picture of molecular energy levels as a function of orientational potential; this is shown in Figure 6 for the example of a tetrahedron in a tetrahedral potential. It is easy to see from the figure that the extent and nature of orientational disorder in molecular solids will depend both on the magnitude of the orientational potential relative to the rotational constant, and the thermal accessibility of these states.

The above general approach provides the basis for understanding orientational ordering in solids. However, as will be shown in Chapter II, a more specific approach is needed to reveal the detailed features of solid methane.

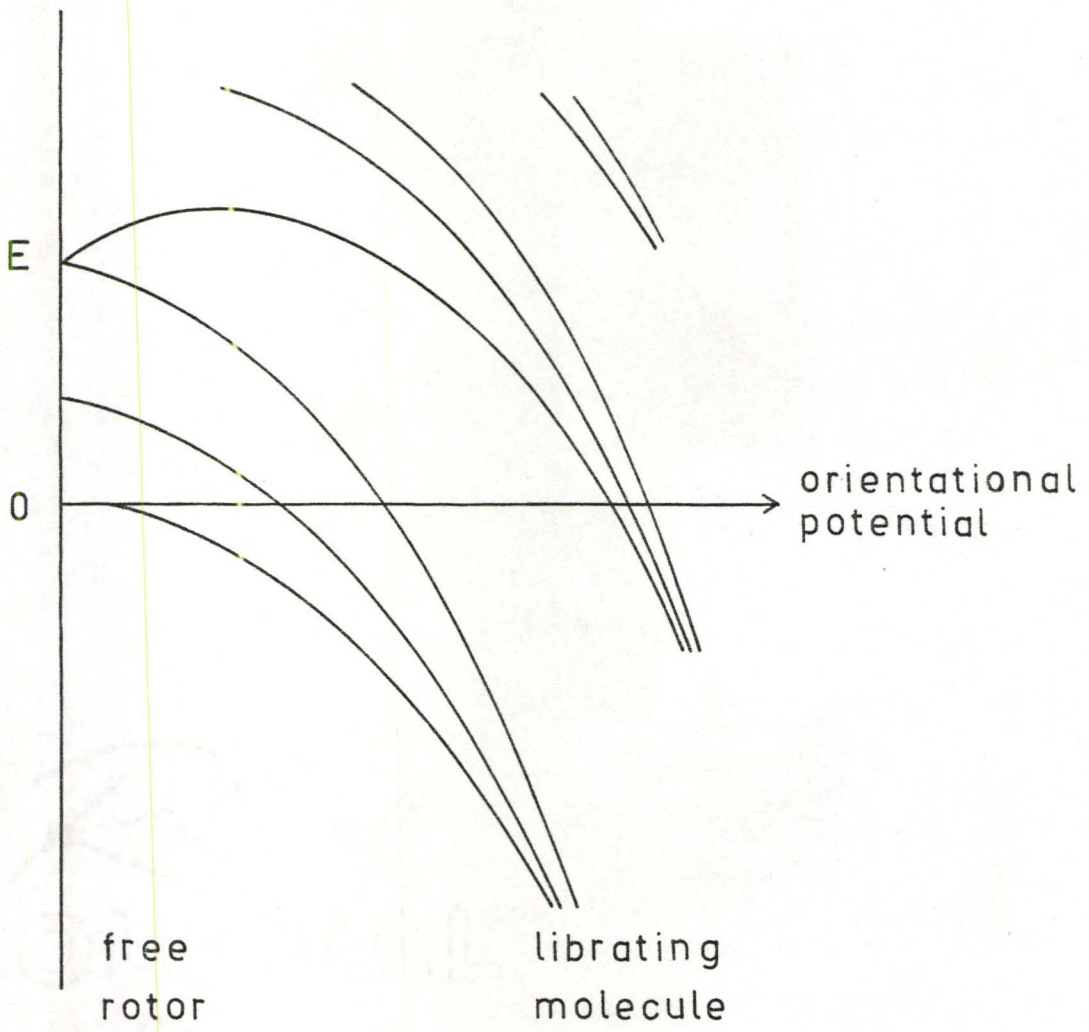

Figure 6: Molecular Energy Levels of the Tetrahedron in a Tetrahedral Potential, as a Function of Orientational Potential Strength.

CHAPTER II

SOLID METHANE: AN INTRODUCTION

Part A: Experimental Observations on Solid Methane

1. The Phase Diagram

Before proceeding further with the theory of solid methane, it is desirable to examine the results of some experimental observations. The most basic experimental result has been the determination of the methane phase diagram.

In 1929, Clusius[34] observed an anomaly in the heat capacity of solid CH_4 around 20.4K. Later, Clusius et al.[35,36] found that there are two anomalies in the heat capacity of solid CD_4 — one at 22.1K and one at 27.1K. The relationship between the phase transitions in CH_4 and CD_4 was clearly shown by heat capacity measurements made by Bartholomé et al.[37] on mixtures of CH_4 and CD_4. The experiments showed the existence of three solid phases for mixtures containing more than ∿20 mole % CD_4; the concentration dependence of the transition temperature showed that the upper transition in pure CD_4 corresponds to the transition observed in pure CH_4.

Sperandio's observations[38] of the heat capacity of the partially deuterated methanes, CH_3D, CH_2D_2 and CHD_3, indicate that their phase diagrams are similar to that of CD_4. In Table III, the most accurate determinations of the phase transition temperatures and the melting points of the methanes are given, where phases I, II and III are numbered

Table III

Phase Transition Temperatures and Melting Points of the Isotopic Methanes under Zero Applied Pressure

Methane	$T_{I \rightarrow II}$ (K)	$T_{II \rightarrow III}$ (K)	$T_{m.pt.}$ (K)
CH_4	20.5[a,b]	-	90.67[c]
CH_3D	23.1[c,d]	16.1[c,d]	90.42[c]
CH_2D_2	24.9[c,d]	19.1[c,d]	90.16[c]
CHD_3	26.0[c], 26.3[d]	20.9[c], 20.6[d]	89.95[c]
CD_4	26.9[a,e]	22.0[a,e]	89.76[c]

[a] from the heat capacity measurements of Colwell et al.[39]

[b] from the X-ray diffraction data of Aadsen[40]

[c] from the heat capacity measurements of Sperandio[38]

[d] from the heat capacity measurements of Colwell et al[42]

[e] from the X-ray diffraction data of Baer et al[41]

in order of decreasing temperature. The solid-solid transitions are known[39,40,41] to show considerable hysteresis and therefore the temperatures are quoted to only 3 significant figures. As can be seen from the table, the results of various investigations of the transition temperatures are in good agreement.

It should be noted that it is often difficult to determine the order of a phase transition. Even with the use of very sensitive thermometers, it is not an easy task to distinguish between the infinite heat capacity of a first order transition, and a very large (but finite) heat capacity of a second order phase transition. A better criterion may be the change in volume associated with the transition: the transition is classed as first order only if the volume change is discontinuous. It is again experimentally difficult to distinguish between a true discontinuity and a continuous change on a very compressed temperature scale. It is now, however, quite well established[40,41] that the phase transitions in solid methane are first order.

Considerable effort has been spent, and some controversy has resulted concerning the properties of methane at elevated pressures. Trapeznikowa and Miljutin[43] first measured the heat capacity of CH_4 under pressure and observed another solid-solid phase transition in this methane. Stevenson's volume discontinuity measurements[44] indicated the possibility of two higher pressure phases of CH_4, while

Stewart's more accurate use of the same technique[45] indicated the presence of only one higher pressure solid phase in each of CH_4 and CD_4 for $P < 6$ kbar. More recently, Nijman[46] has carried out NMR proton spin-lattice relaxation time measurements on CH_4 as a function of pressure and temperature. These measurements, in conjunction with the dielectric measurements of Constantino and Daniels[47], give the phase diagram for CH_4 shown in Figure 7. A possible fourth phase (phase IV) identified by the latter experiments is shown also. Figure 8 illustrates the phase diagram of CD_4, as observed by Stewart[45].

It is tacitly assumed that the structure is the same for each of the isotopic methanes in a given phase, and a great deal of effort has been spent on the determination of the properties of the three phases of solid methane. (Phase IV cannot be said to be firmly established as yet.) In the next section, the characteristics of each of the phases will be examined.

2. Physical Properties of Solid Methane

(a) Phase I

An early X-ray diffraction study of solid CH_4[48] indicated that the solid is face-centred cubic both above and below 20.4K; the difference in lattice constant for the phase transition was $\sim$1%. This small change in lattice constant indicated that the phase I $\rightarrow$ II transition was probably associated primarily with a change in the orientational order of the methane molecules.

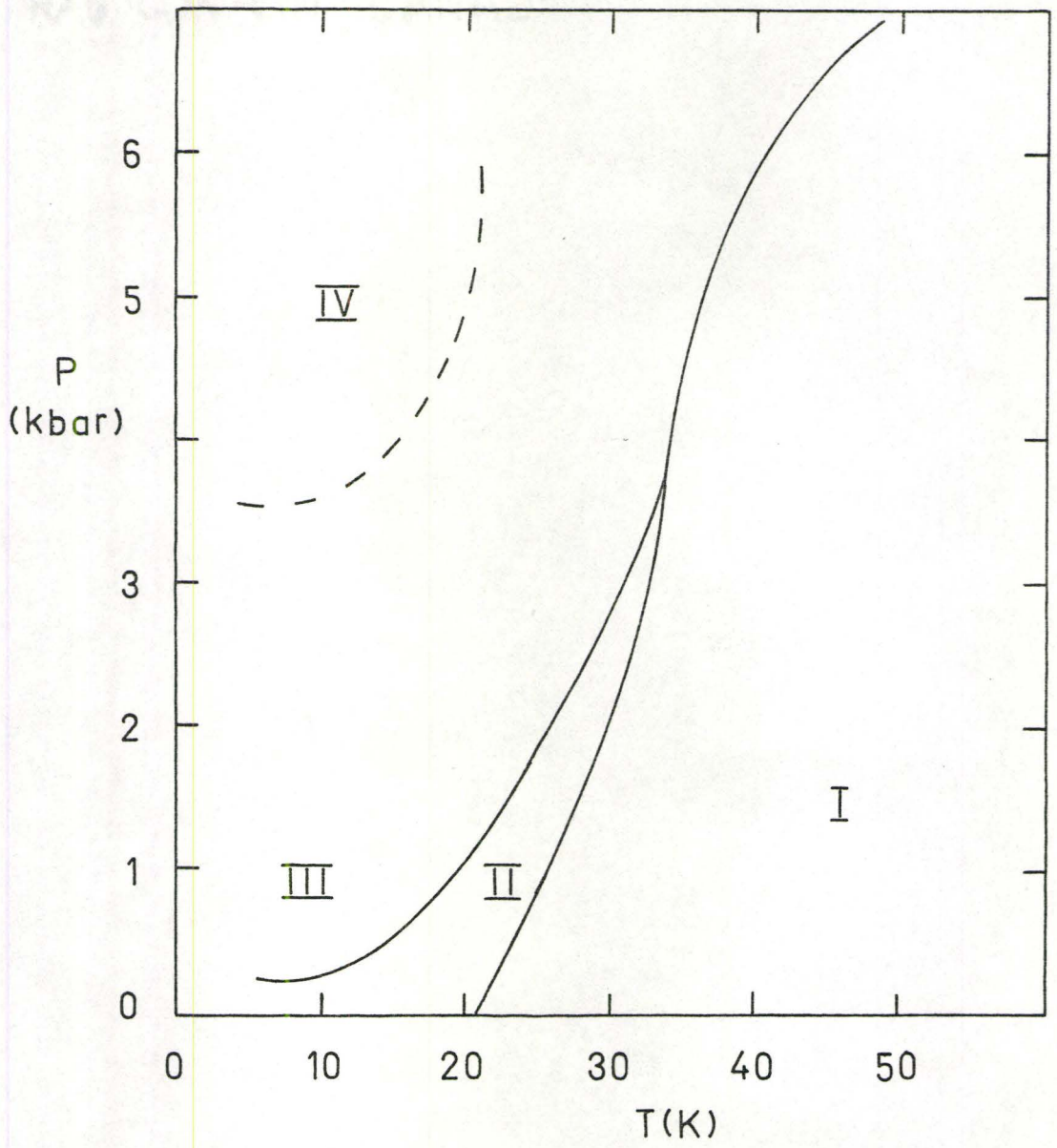

Figure 7: The Phase Diagram of Solid CH_4.

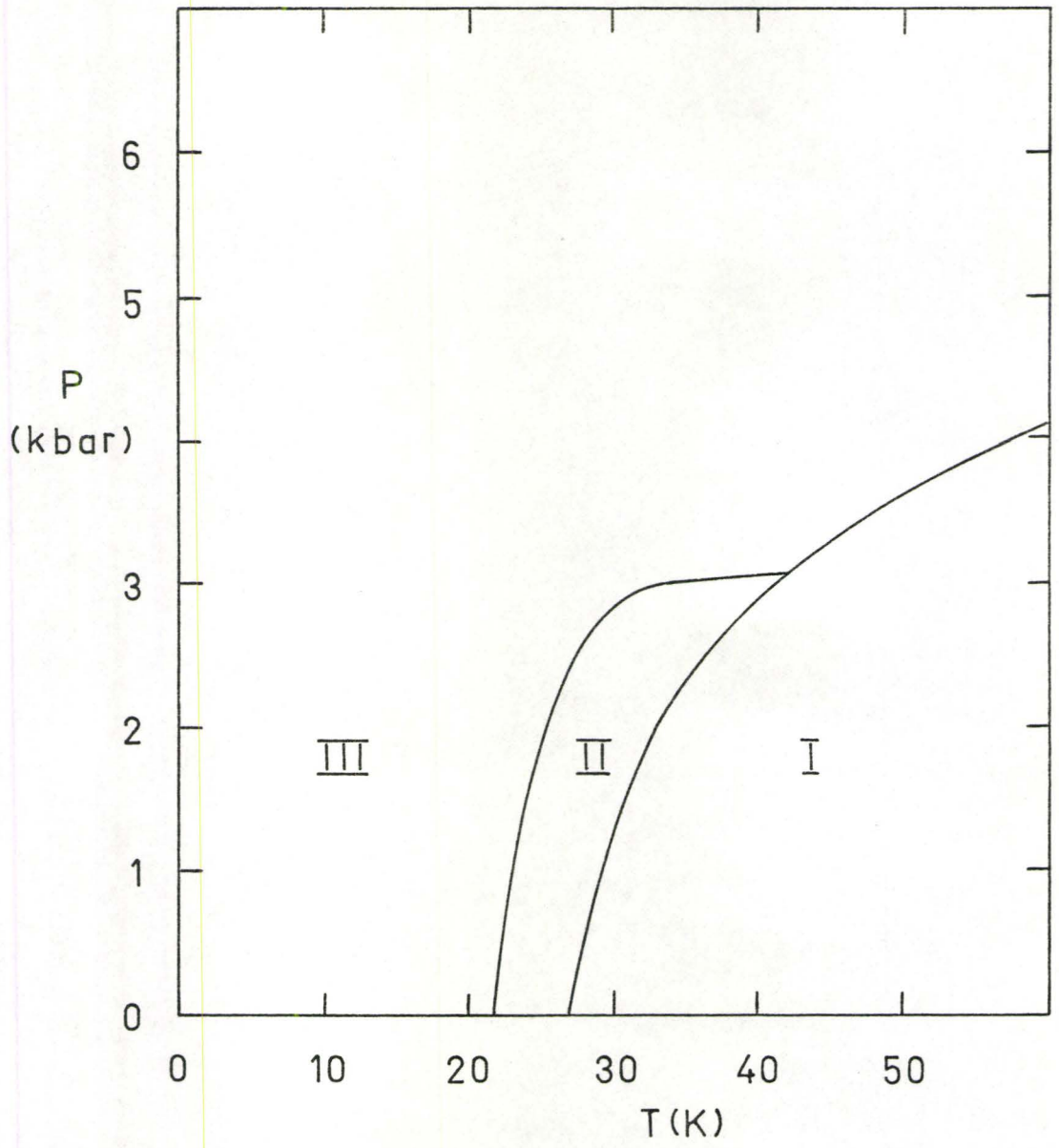

Figure 8: The Phase Diagram of Solid CD_4.

Early proton NMR experiments[49] showed that for T > 65K, both the line width and characteristic time for spin-lattice relaxation in CH_4 approach the liquid values. Also, Raman measurements of CH_4 in phase I near the melting point showed[50] rotational wings to the same extent as are seen in the liquid phase. Observations of the infrared absorption in the ν_3 mode of CH_4, CD_4 and CH_4 in CD_4[51,52] showed that the molecules undergo slightly hindered rotation in the liquid; one can conclude, therefore, that the molecules in the higher temperature region of phase I also undergo slightly hindered rotation. This has since been confirmed by neutron inelastic scattering[53] and also by observations of the molecular structure factor[54].

Experiments throughout the temperature range of phase I have shown that molecular reorientation is increasingly hindered as the temperature is lowered. Thiele et al.[55] measured the velocity and attenuation of ultrasonic waves in the solid, and observed that the characteristic time increased sharply with decreasing temperature. The ^1H and ^2H spin-lattice relaxation time, T_1, in solid CH_4, CD_4, CHD_3, CH_3D, CH_4-CD_4 mixtures and CH_4-Kr mixtures indicated[56] that the strong temperature dependence of T_1 is associated with changes in the ease of molecular reorientation. As the temperature is raised, the barrier to molecular reorientation is more easily overcome, such that the melting process principally involves an abrupt increase in centre of mass motion.

X-ray[40,41,57] and neutron[54,58] diffraction studies

have confirmed that in phase I the molecular orientations are completely disordered, and molecular reorientation is slightly hindered, for all the molecules. The space group is Fm3m (site symmetry O_h) with 4 molecules per unit cell.

(b) Phase II

As noted earlier, the lattice structure of phase II of solid methane is known to be face-centred cubic, and the small change in volume associated with the phase I → II transition indicates that there is primarily a difference in orientational ordering between the two phases[48].

An elegant neutron diffraction study of CD_4[54] has shown phase II to be an 8-sublattice structure with space group Fm3c. Twenty-four of the 32 molecules in the conventional (non-primitive) unit cell are orientationally ordered on sites with local symmetry $\bar{4}2m$ ($\equiv D_{2d}$), and the remaining 8 molecules per unit cell (on sites of local symmetry 432 ($\equiv O$)) are orientationally disordered. One-eighth of the unit cell of this complex structure is illustrated in Figure 9. Amazingly, this structure was first proposed theoretically for phase II by James and Keenan[17], thirteen years before it was verified experimentally.

CH_4 seems to exist in phase II down to the lowest experimentally accessible temperatures and, therefore, further information about this phase can be determined from the thermodynamic properties of CH_4 at low temperatures.

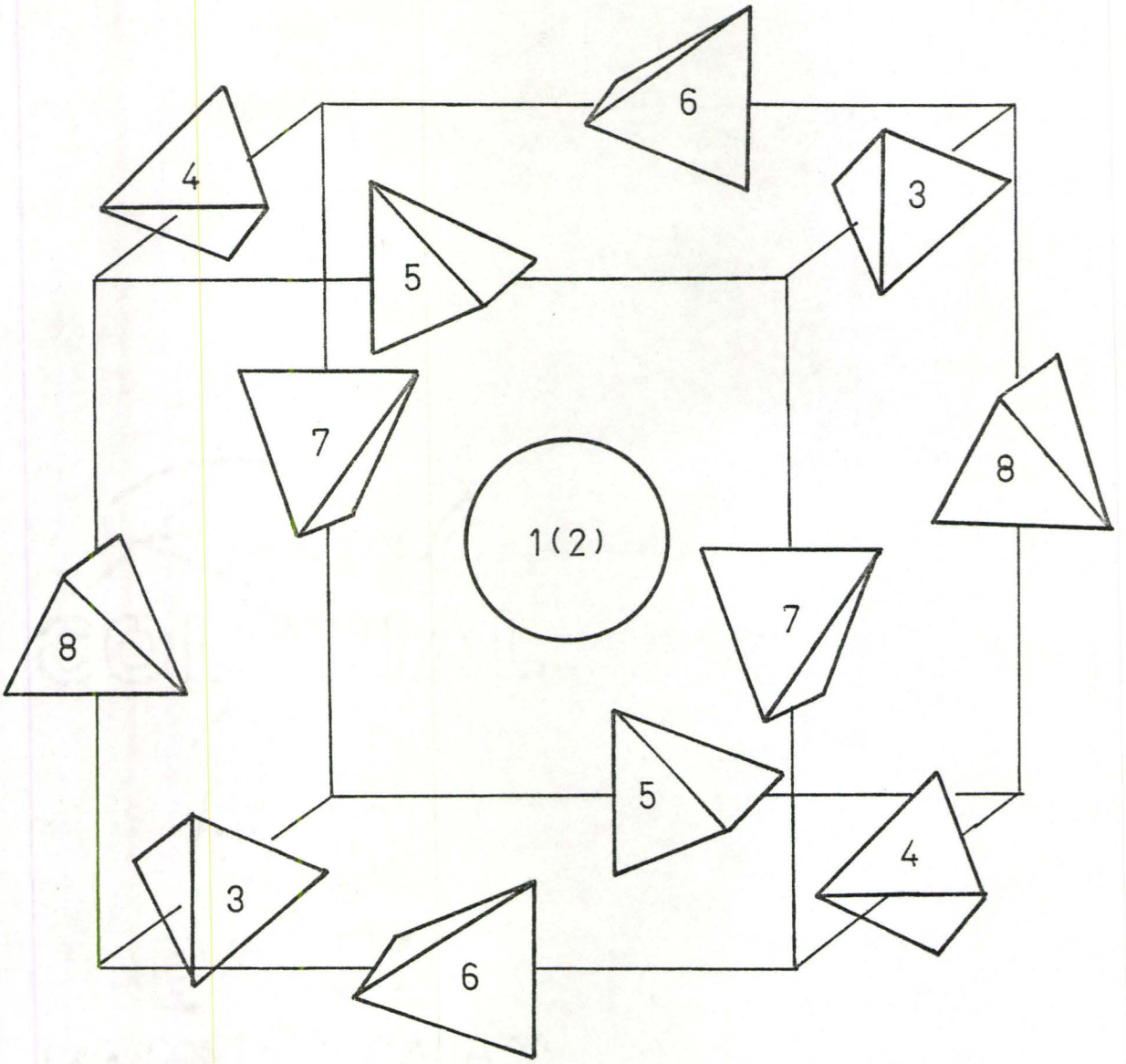

Figure 9: The Structure of Phase II of Solid Methane. (1/8 of the unit cell is shown, and the molecules are numbered according to their sublattice.)

Giauque et al.[59] and Frank and Clusius[60] found that, neglecting nuclear spin contributions, the entropy determined from spectroscopic data, S_{spec}, was equal to the calorimetric entropy, S_{cal}, as determined from a smooth extrapolation of Cp from its T = 15K value to T = 0K. This result indicated that it was unlikely that phase III would occur in CH_4 under its own vapor pressure, yet when the heat capacity of CH_4 was measured down to T = 4.2K, considerable thermal inertia was observed for $T \lesssim 8K$.[61] This was initially attributed to a phase transition in solid CH_4, but more recent work has shown that it was related to a change in nuclear spin symmetry species composition.[62-66]

The four protons and the tetrahedral symmetry of CH_4 give rise to three nuclear spin symmetry species. The symmetries of these species are designated as A, T and E and the total spins, I, are respectively 2, 1 and 0.[67] The product of the spatial degeneracy (1, 3 and 2 respectively) and the spin degeneracy (= 2I + 1) leads to a high temperature spin species composition of 5A, 9T and 2E. Since the lowest rotational state (J = 0) is only allowed for the A species, the equilibrium composition at T = 0K will be 100% A. The conversion between nuclear spin symmetry species is catalysed by O_2 in the case of CH_4, and has now been well-characterized in this methane through thermodynamic[61,66], NMR[68] and total neutron cross-section[69] experiments which probe $\langle I(I+1) \rangle$. It is well-established now that the thermal anomaly in the region $4K \lesssim T \lesssim 8K$ is due to spin species conversion of the

molecules on the disordered sublattices, and that the lower temperature anomaly (T $\sim$ 1K) is due to conversion of the molecules on the ordered sublattices.

This nuclear spin species conversion adds a further complexity to the problem of understanding solid CH_4. As will be discussed later in this thesis, nuclear spin species conversion is also important to the study of the deuterated methanes.

(c) Phase III

Phase III has been known for some time to have a non-cubic structure, as evidenced by an early observation of the appearance of weak optical birefringence in CH_3D and CD_4 below the II $\rightarrow$ III transition[36]. An X-ray study[57] of the lattice parameter of CD_4 indicated that the solid undergoes a small tetragonal distortion in proceeding from phase II to phase III; this tetragonal distortion is consistent with a sensitive measurement of the optical birefringence in phase III[70]. The c to a ratio was initially[57] reported as $\sim$1.02 and has been confirmed recently[41] by a very precise measurement of the change in lattice parameters of CD_4 with temperature, to be 1.012 at T = 11.6K.

A neutron diffraction study[54] of CD_4 unfortunately failed to determine the phase III structure unambiguously, for reasons indicated below. The data suggest that the low temperature phase can be understood by an ordering of the

disordered molecules of phase II together with slight distortions of the other sublattices. It was later suggested by Press and Hüller[71] that the phase III space group could possibly be tetragonal $P4_22_12$ with Z = 16 (i.e. 16 molecules per unit cell), or tetragonal $P4_2/nmc$ with Z = 32. X-ray and neutron diffraction studies of CD_4 carried out by Arzi and Sándor[72] indicated that $P4_2bc$ (Z = 16) and $P4_2/nmc$ (Z = 32) are both possible space groups for phase III. Unfortunately, a complete and precise direct investigation of the structure of phase III is rendered extremely difficult by the fact that below the II → III transition, the tetragonal c-axis is pointing randomly in the directions of the (formerly) cubic axes[71].

It is possible, in principle, to characterize phase III through thermodynamic measurements. The residual entropy, which is the difference between the spectroscopic entropy at a given T and P (calculated from the usual statistical mechanical contributions) and the calorimetric entropy at the same T and P (determined from the observed heat capacity), is a measure of the disorder in a material. Extrapolation of the observed heat capacity smoothly to T = 0K on the basis of measurements for $T \geq 8K$ gives an apparent residual entropy, excluding the nuclear spin contribution, of R ℓn 4 for CH_3D[60,73-4] R ℓn 6 for CH_2D_2[74], R ℓn 4 for CHD_3[74] and zero for CD_4[60,73,74] (within the experimental errors). In the terminology of classical mechanics, the results indicate that there is a

randomization of the position of the C-H and C-D bonds at a given site for the partially deuterated methanes in phase III. Since the apparent residual entropy is a time-averaged property of the system, it is not possible to state whether this randomization is static or dynamic. However, investigation of the heat capacity of the deuterated methanes at lower temperatures has transformed the discussion of these solid methanes to the realm of quantum solids.

Measurements of C_p for the partially deuterated methanes at $2.5K \leq T \leq 8K$ revealed[39,74] the presence in each of a Schottky[75] anomaly, i.e. an anomalous heat capacity due to the thermal depopulation of low -lying energy levels. Colwell[76] extended these measurements to T = 0.3K and the combined results[39,74,76] are shown in Figure 10. Note that CD_4 does not appear to have low-lying energy levels in this same energy range. These measurements, in conjunction with Nagamiya's study[77] of the group theory of low-lying energy levels in the solid isotopic methanes, give an indication of the nature of the tunneling levels of the deuterated methanes in phase III. However, the conclusions about the energy level schemes that can be drawn are extremely sensitive to the extrapolation of the entropy of the solid to T = 0K, as will be discussed later. In fact, it is a central aim of this thesis to make deductions about the nature of phase III, based on heat capacity measurements of isotopically purified deuteromethanes at very low temperatures.

Figure 10: The Heat Capacites of the Deuterated Methanes.

The measurements for $T \geq 2.5K$ (Refs. 39 and 74) and for $T \geq 0.3K$ (Ref. 76) are in good agreement in their overlap region.

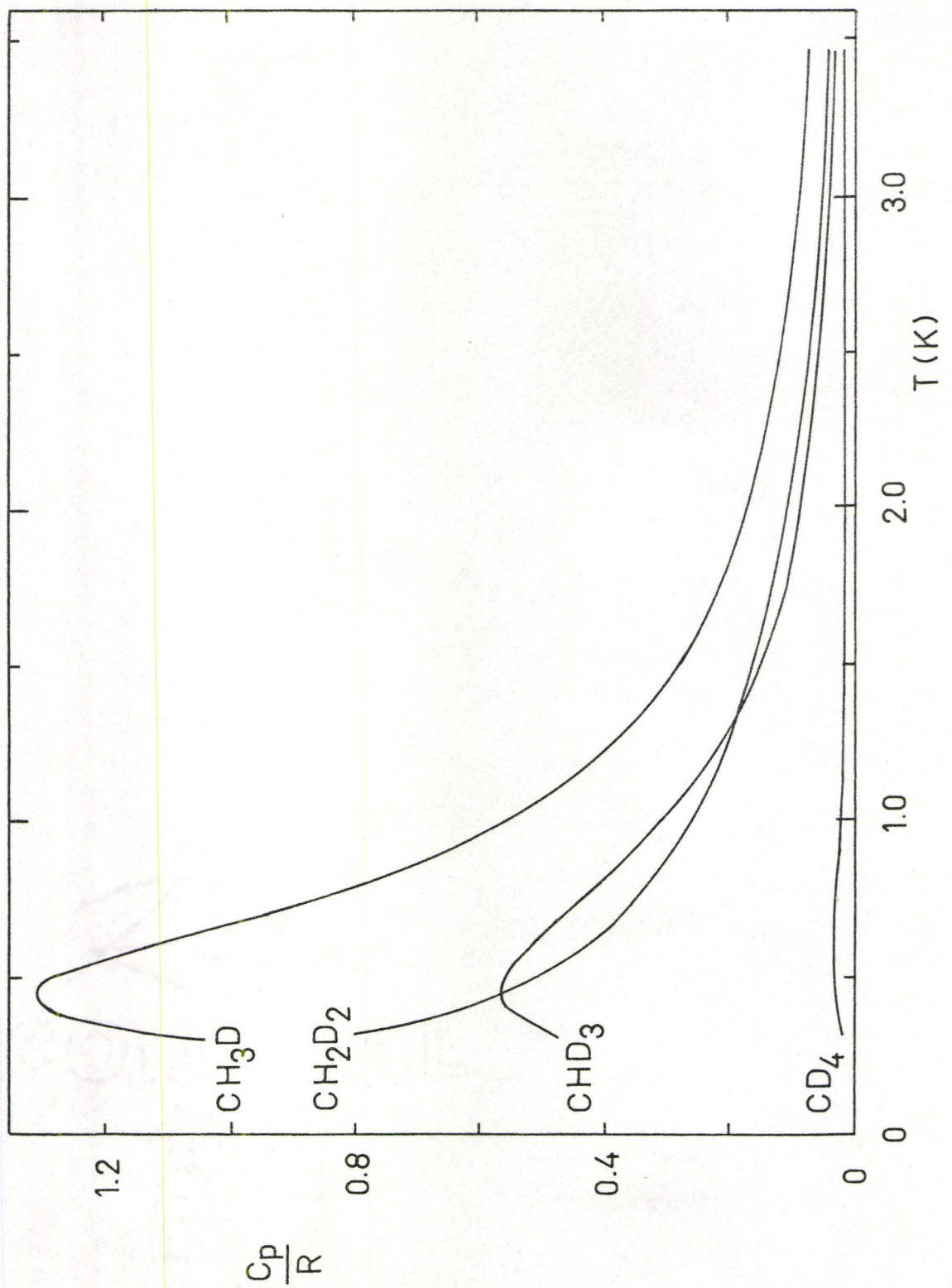
$\frac{C_p}{R}$
1.2
0.8
0.4
0
0
1.0
2.0
3.0
T (K)
CH_3D
CH_2D_2
CHD_3
CD_4

There is conclusive evidence now, both from NMR[78] and total neutron cross-section measurements[7,9] that nuclear spin-species conversion takes place in phase III of CH_3D. The heat capacity of that methane has been well characterized down to T = 0.15K[79,80,81], but it has not been straightforward to understand the resulting extrapolation of the entropy of T = 0K. As will be discussed later in this thesis, the change in entropy through the Schottky anomaly in CH_3D is more than that expected due to either the complete ordering of the C-D bonds ($\Delta S = R \ln 4$) or complete nuclear spin species conversion ($\Delta S = R \ln 2$), yet it is less than that due to these combined processes ($\Delta S = R \ln 8$).

The CH_2D_2 sample used by Colwell[76] showed long relaxation time after the heat pulses in the heat capacity measurements. Colwell considered that this could be due to nuclear spin species conversion in either CH_2D_2 or in the CH_3D impurity, since similar relaxation processes were noted in CH_4[61,66] and CH_3D[74,76,79] in the region of conversion. No conclusions were drawn concerning conversion in CHD_3 and CD_4. More information about conversion in the deuteromethanes will be presented in this thesis.

It should be apparent from the foregoing summary that there has been a considerable experimental effort put forward to understand the properties of the solid isotopic methanes. The theoretical studies of solid methane will now be examined to see how they account for these properties.

Part B: Theoretical Studies of Solid Methane

1. The James and Keenan (JK) Theory[17]

The general theory of Hüller[31] gives an overall understanding of the basis of orientational ordering in molecular solids, but its specific predictive powers are somewhat limited and more detailed interaction potentials must be considered.

The theoretical understanding of solid methane advanced very significantly with the publication of the theory of James and Keenan[17] in 1959. Their aims were to explain the existence of the 3 solid phases of CD_4 and to predict the molecular ordering of each phase, based on a simple model of the solid.

Their model of solid methane neglected the molecular and lattice vibrations, and treated the crystal as a face-centred cubic array of spherical rotors carrying tetrahedral charge distributions. They assumed that the dominant term in the intermolecular interaction is electrostatic, and retained only the octopole-octopole interaction of nearest neighbours in the lattice. Since this calculation neglected such refinements as lattice and molecular vibrations (which would tend to modify the molecular coupling), the quantization of molecular rotation and the statistical effects of nuclear spins, it only applies to the heaviest methane, CD_4.

Using the effective octopole moment as the only adjustable parameter, a mean field calculation was carried

out to minimize the Gibbs free energy. The self-consistency condition leads to a family of so-called "consistency equations", one equation per molecule in the crystal. It is the solutions to these equations, simplified by the use of tetrahedral harmonics and the associated tetrahedral rotor functions, which give three solid phases for methane, in agreement with the experimental observations.

The JK calculation correctly predicted the structure of phase I and, more surprisingly, the complex sublattice structure of phase II of solid methane. (As noted earlier, it was many years before this structure was experimentally verified[54].) Their work correctly predicted the phase II → III transition to be first order and, when the effective octopole moment was adjusted to put the phase I → II transition at T = 27.1K, the phase II → III transition was predicted to be at T = 24.4K. (This is very close to the observed temperature of 22.0K.) In addition, their model predicts heats of transition which are in close agreement with the experimental values[36] for both the I → II and II → III transitions.

The simplicity of the model precludes prediction of some refinements in the properties of solid methane. For example, the phase I → II transition is predicted to be second order, in contrast with its observed[40,48] first order behaviour. In addition, the predicted phase III structure with all the molecules oscillating about equivalent equilibrium

orientations was ruled out by a neutron diffraction study[54] of CD_4. In spite of these limitations, the amazing success of this very simple model of solid methane cannot be overemphasized.

2. Quantum Mechanical Investigations

(a) Further Work Based on the James and Keenan Model

More recent theoretical studies of solid methane have been carried out almost exclusively by Yamamoto and his co-workers at Kyoto University. With the formulation of a model applicable to all of the isotopic methanes, rather than just to CD_4, as the aim, their work started as a quantum mechanical extension of the James and Keenan model. This subsection will outline the model and its applications; the primary conclusion from the study is that a more detailed interaction potential needs to be considered to yield a quantitative understanding of solid methane. To this end, an extended James and Keenan (EJK) model was developed, as described in the next subsection. Still further refinements are necessary to understand the properties of phase III, and these are outlined in the final subsection of this chapter.

Based on the JK model, the electrostatic octopole-octopole interaction between nearest neighbours of a face-centred cubic array of molecules with fixed centres was again considered[82]. The molecular motion was studied in the space spanned by the rotational wavefunctions of the free molecules for $J \leq 9$, where J is the rotational quantum

number for a free molecule. The molecular field approximation was employed (i.e. each molecule was assumed to feel the molecular field of the average of the equilibrium states of its neighbours), and the minimization of the Gibbs free energy again led to a series of consistency equations which could be solved to yield properties of the solid.

The calculations reproduced[82] the results of James and Keenan, and also gave rise to a wealth of additional information about solid methane. For example, CH_4 was predicted not to transform into phase III except under applied pressure[83]. This, in combination with the prediction that nuclear spin species conversion would not lead to a sharp transiton in CH_4[82], showed the necessity for experiments probing conversion in this methane. The model also gave[84] values of the energy of conversion, the enthalpy change in the transition and the effect of pressure on the lower transition temperature for CH_4 that are in good agreement with experiment, as shown in Table IV.

The calculated upper transition temperatures in solid CH_3D, CHD_3 and solid solutions of CH_4 and CD_4 agree[85] with the experimental result of Bartholomé et al[37], i.e. that the upper transition temperature depends chiefly on the mean molecular weight of the methane molecules, whether the sample is a pure isotopic methane or a mixture. Since the model does not take centre of mass motion into account, the result indicates that translational motion is not the important

Table IV

Comparison of Calculated and Experimental Properties of CH_4

	Experimental Value	Calculated[f] Value
ΔH of Conversion ($T \sim 8K$)	4.4 cal/mole[b]	3.82 cal/mole
ΔH of I→II transition	18.1 cal/mole[c] 15.7 cal/mole[d]	15.2 cal/mole[g]
Effect of pressure on lower transition temperature[a] $= \frac{\zeta dT}{d\zeta}$	62K[e]	64K

[a] ζ = coupling parameter = $\frac{I_3^2}{R^7}$, where I_3 is the effective octopole moment and R is the distance between molecular centers.

[b] from Refs. 61 and 74.

[c] from Ref. 34 for $17K \leq T \leq 21K$.

[d] from Ref. 36 for $20K \leq T \leq 21K$.

[e] from the compressibility, as determined in Ref. 45.

[f] from Ref. 84.

[g] for $16K \leq T \leq 20K$.

factor in determining the upper transition temperature[39,85].

Under the assumption that phase III of CH_3D is ferrorotational (i.e. that every molecule feels the same molecular field as every other), and that CH_3D does not undergo nuclear spin symmetry species conversion, the Schottky anomaly in CH_3D was semi-quantitatively reproduced using the James and Keenan model[86]. The temperature was higher and the anomaly was broader than that observed experimentally[74,76,79-81] but their calculations showed that the addition of conversion to the calculation would sharpen the anomaly and shift it to a lower temperature[86]. This study suggested that the Schottky anomaly in CH_3D is the kinematical consequence of a methane molecule in a hindering potential, in combination with nuclear spin species conversion,[86] as earlier suggested by Colwell[76].

A later examination of the quantum statistical JK model provided[87] a quantitative explanation for the observed[88] negative thermal expansion in solid CH_4. As the temperature is lowered, conversion to the A nuclear spin symmetry species occurs. This species is the only one which includes the $J = 0$ rotational state and therefore the rotational ordering which was taking place for the E and T molecules (into their lowest rotational states) is destroyed. Since the rotational ordering is weakened, its effect of squeezing the lattice is also weakened, and negative thermal expansion results.

Although the James and Keenan model satisfactorily

explains many properties of the solid isotopic methanes, as illustrated above, it does not account for the differences in the two types of molecules in phase II[89]. (The disordered and ordered molecules are commonly referred to as "O_h" and "D_{2d}" respectively, with the reason given that these are the respective site symmetries. In fact, the site symmetry is O_h for the phase I molecules, but the disordered molecules of phase II are on sites of O symmetry; the crystalline field has O_h symmetry with respect to the crystal fixed axes[89]. In this thesis, the disordered and ordered molecules will be called O and D_{2d} respectively, according to their true site symmetries.) The present model requires some modification in order to see these features.

(b) Extended James and Keenan (EJK) Model

The James and Keenan model of solid methane, discussed above, does not take into account the effect of a hindering potential on the disordered molecules in the solid. The extension of the James and Keenan model to include a crystalline field initially considered[90] the octahedral crystalline field which a CH_4 molecule feels in a Kr or Xe matrix[91]. In a molecular field calculation for $J \leq 4$, double transitions were again found for suitable values of the effective octopole moment, but the effect of the crystalline field was found to be sufficiently important to warrant further studies with a more realistic crystalline field[90].

Yasuda[92] used empirical pairwise interatomic potentials[93-96] to study the interaction of methane molecules in the solid state, and derived expressions for the crystal fields which methane feels in Xe and Kr matrices, and also in bulk methane. The inclusion of these crystal field expressions in the EJK model of solid methane has been rather successful. It gives the observed phase I and phase II structures of solid methane[97], and predicts the phase I → II transition to be first order yet unlike Pauling's rotational melting[22] and Frenkel's order-disorder transition[19,20,21] Again, no phase II → III transition is predicted in CH_4 under its own vapour pressure, and the model can give a qualitative discussion of this transition in CH_4 at elevated pressures[98]

In the EJK model which includes rotational states up to J = 10, the calculated[99] selection rules and intensities for the ν_3 and ν_4 modes of the infrared absorption of methane in rare gas matrices give satisfactory agreement with the experimental results[100] There is good agreement between the calculated[101] and observed[102] ν_3 and ν_4 Raman bands of methane in rare gas matrices, and the EJK model yields thermodynamic quantities that are in fair agreement with the experimental values. As examples, the calculated and experimental transition temperatures and entropies of transition for CD_4 are given in Table V. Furthermore, the heat capacity of CH_4 has been calculated[89], and agrees with the observations of Colwell et al.[39,61] and Vogt and Pitzer[66], particularly in

Table V

Comparison of Calculated and Experimental Transition Temperatures and Entropies of Transition for CD_4

Transition		T(K)	ΔS/R
I → II	Calculated[a]	30	0.43
	Experimental	27.1[b]	0.62[c]
II → III	Calculated[a]	24	0.60
	Experimental	22.2[b]	0.40[c]

[a] from Ref. 97

[b] from Ref. 41

[c] from Ref. 39

the region where spin species conversion occurs. In fact, this calculation clearly shows the separate contributions due to conversion on the O and D_{2d} lattice sites.

It is this latter result which is the principal success of the model: the O and D_{2d} molecules of phase II show different physical properties. The calculated[98] energy levels for the two types of molecules, as shown in Figure 11, are in good agreement with the results of neutron inelastic scattering experiments[103,104,105], and yield[98] values of $\langle I(I+1) \rangle$ for CH_4 which agree with the NMR results.[64,5,106] In addition, the calculated zero point entropy of CH_4 agrees with that of Colwell et al.[39] if the heat capacity anomaly at $T \sim 8K$ is taken to be due to conversion of the O molecules.

The EJK model of solid methane also predicts a temperature dependence of the tunneling levels of the D_{2d} molecules in their equilibrium spin species concentrations at low temperatures. As illustrated in Table VI, the calculation agrees with the combined results from NMR[28,107], neutron inelastic scattering[29,108] and heat capacity[66] measurements.[109] Although the model is very successful at predicting and explaining many properties of the solid isotopic methanes, it was unable to predict the correct structure of phase III.[110] Modifications to the model were therefore required.

(c) Extension of the EJK Model to Predict Phase III Properties:

The EJK model has been extended[111] through the

Figure 11: The Calculated[98] Energy Levels for Phase II of CH_4. (E, T and A are the nuclear spin symmetry species.)

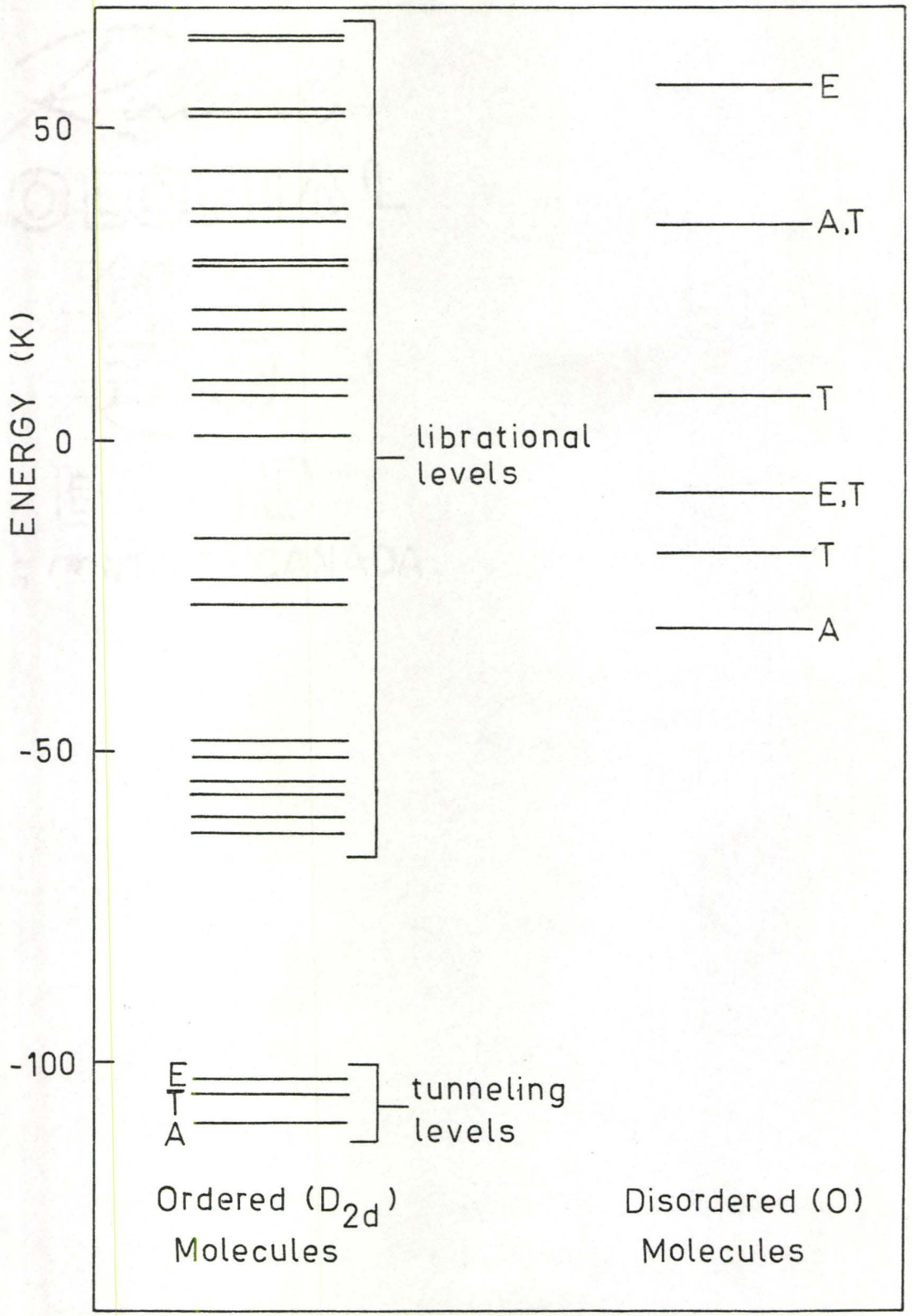
ENERGY (K)
50
0
-50
-100
librational levels
tunneling levels
E
T
A
E
A,T
T
E,T
T
A
Ordered (D_{2d}) Molecules
Disordered (O) Molecules

Table VI

Temperature Dependence of Tunneling Levels of D_{2d} Molecules in CH_4 (Energies measured from lowest A level in K)

	T(K)	ΔE_E	ΔE_T
Calculated[a]	0.00	3.30	2.16
	0.97	3.10	2.04
	2.00	2.89	1.91
	3.33	2.81	1.86
	4.07	2.79	1.85
	5.26	2.78	1.83
Observed	0.4-1.5[b]	2.89	1.951
	4.2[c]	-	1.7
	4.2[d]	-	1.75±0.1
	4.9[e]	2.51 ± 0.03	1.66 ± 0.03

[a] from Ref. 89

[b] from Ref. 66

[c] from Ref. 28 and 107

[d] from Ref. 108

[e] from Ref. 29

addition of octopole-hexadecapole and hexadecapole-hexadecapole terms to the potential energy, using a simplified 1-body crystalline field interaction. The classical molecular field approximation was again employed, and the stabilities of solutions to the consistency equations which branch from phase I or from phase II were examined. In addition, Landau's theorem of second order phase transitions was extended to determine the space groups of the resulting phases.

Two multipolar interaction strengths were the only adjustable parameters used, and the model correctly predicts the phase I and phase II structures. Some 32 possible structures arise for phase III, and, as might be expected for such a delicate balance of interactions, the existence region of each solution is rather sensitive to the adjustable parameters. The extinction rules that were obtained from neutron diffraction studies[54,72] limit the phase III structure to 4 of the 32, and a calculation of the phase diagram at T = 0K leads the authors to the conclusion that phase III likely belongs to the space group $P4_2/mbc$ with 16 molecules per unit cell. This prediction indicates that there are 3 different types of molecules in phase III (in the ratio 1:2:1); the O molecules of phase II go to site symmetry D_2 and the D_{2d} molecules of phase II go to site symmetries C_s and S_4. (See Figure 12). It is important to notice that the octapole-hexadecapole and hexadecapole-hexadecapole interactions are necessary to stabilize this particular structure.

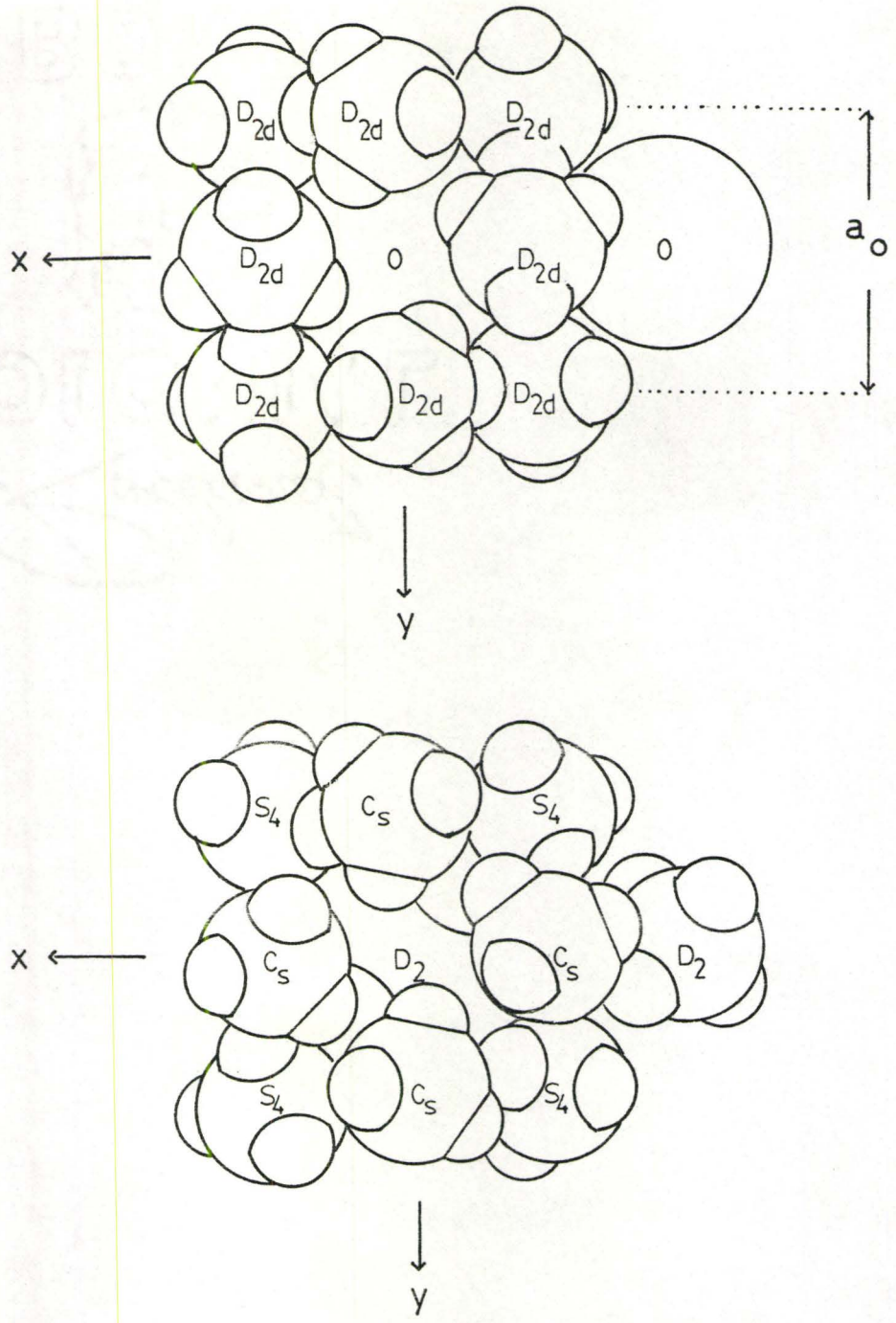

Figure 12: The Theoretically Proposed[111] Structure of Phase III As It Arises from Phase II.

The calculation also provides information about the forces that stabilize structures other than phase III of solid methane. When the hexadecapole moment is weakened and the crystalline field is strengthened, the phase II structure[112] of solid CF_4 is observed. Similarly, if the crystalline field is weakened, the $I\bar{4}2m$ structure is stabilized; this is related to a proposed structure[113] for SiF_4 through a contraction of the z-axis. Also, the calculation predicts that phase IV of solid methane, if it indeed exists, belongs to the space group $R\bar{3}$ (Z = 8) or R3c (Z = 32), since these structures are stabilized when the crystal field is strengthened, as it is under pressure.

The model for phase III approximately reproduces the Schottky anomalies that occur in CH_3D[79] and CH_2D_2.[114] Moreover, the proportions of the different types of molecules in phase III are sensible in terms of their possible origin from the O and D_{2d} molecules of phase II. However, the calculated structure of phase III shows some serious differences from the experimental observations. Notably, the phase II → III transition was calculated to be second order, yet it is known to be a first order transition. In addition, there is a considerable discrepancy between the calculated and observed changes in entropy (0.6 R and 0.4 R, respectively) for the phase II → III transition.

One of the main unsolved problems of solid methane at present is an experimental verification of the structure

of phase III. Press[54] had difficulties carrying this out directly with neutron diffraction of CD_4. Recent Raman[115] and infrared[116] absorption studies indicate that the structure is complicated and that there are likely three types of molecular sites in phase III. The absence of coincidences in the Raman and infrared bands indicate that the correct space group will have an inversion element; this rules out the $P4_2\ 2_12$ and $P4_2bc$ space groups.

CHAPTER III

THERMODYNAMIC STUDIES OF THE SOLID DEUTERATED METHANES

Part A: Experimental

As stated in the previous chapter, the structure of phase III of solid methane is not known at this time; a direct experimental determination of the structure did not prove to be definitive.[54] Based on low temperature heat capacity measurements of the deuterated methanes, the order in phase III (as determined from the extrapolation of the entropy of the solid to T = 0K) and features of the low-lying energy states (as determined from the position and shape of the Schottky anomalies) will be presented here. Heat capacity measurements will also yield useful information about nuclear spin species conversion. The thermodynamic investigation will therefore not only provide test properties for any proposed models of phase III, but will also reveal interesting features of this phase.

1. Sample Preparation

(a) Isotopic Purification

The earlier[61,74,76] measurements of the low temperature heat capacity of the solid deuterated methanes yielded somewhat ambiguous results: they were carried out on samples that contained significant isotopic impurities. To a first approximation, the contributions of each of the species in

the sample may be assumed to be additive, but this assumption may not hold for high impurity levels. In addition, it was not certain whether observed[76] thermal relaxation effects in CH_2D_2, for example, were caused by CH_3D impurities, or by a process intrinsic to CH_2D_2. For these reasons, a gas chromatograph that could separate methane isotopes was constructed to prepare the calorimetric specimens. Although this separation technique has been used previously for analytical[117,118] and even preparative[119] separations of such species, it is far from routine and will be described in some detail here.

As in all preparative gas chromatographs, the present apparatus was composed of four main parts: the injection system, the column, the detector and the collector. It is shown schematically in Figure 13.

Samples of commercial (Merck, Sharp and Dohme, Montreal) methanes were admitted to the column for isotopic purification through a rotary multiport valve. When the sample was injected, the carrier gas was diverted to the sample reservoir, and the methane was swept into the column. This reservoir could then be evacuated again before it was reloaded.

The column[120] was 120 m of 6 mm (o.d.) copper tubing, packing with 40-60 mesh Graphon (a graphitized carbon black of surface area $\sim$ 120 m^2g^{-1}.) To eliminate severe tailing of the peaks due to some hydrophilic sites on the Graphon, the adsorbent was coated with 1% squalane (w/w). The column was kindly loaned by Professor F. Bruner of Consiglio Nazionale delle Ricerche, Rome.

Figure 13: A Schematic Representation of the Gas Chromatograph.

A - carrier gas

B - injection valve

C - sample

D - chromatographic column

E - acetone/dry ice slurry

F - thermistors

G - detector bridge

H - chart recorder

J - solenoid assembly

K - liquid N_2

L - collection traps

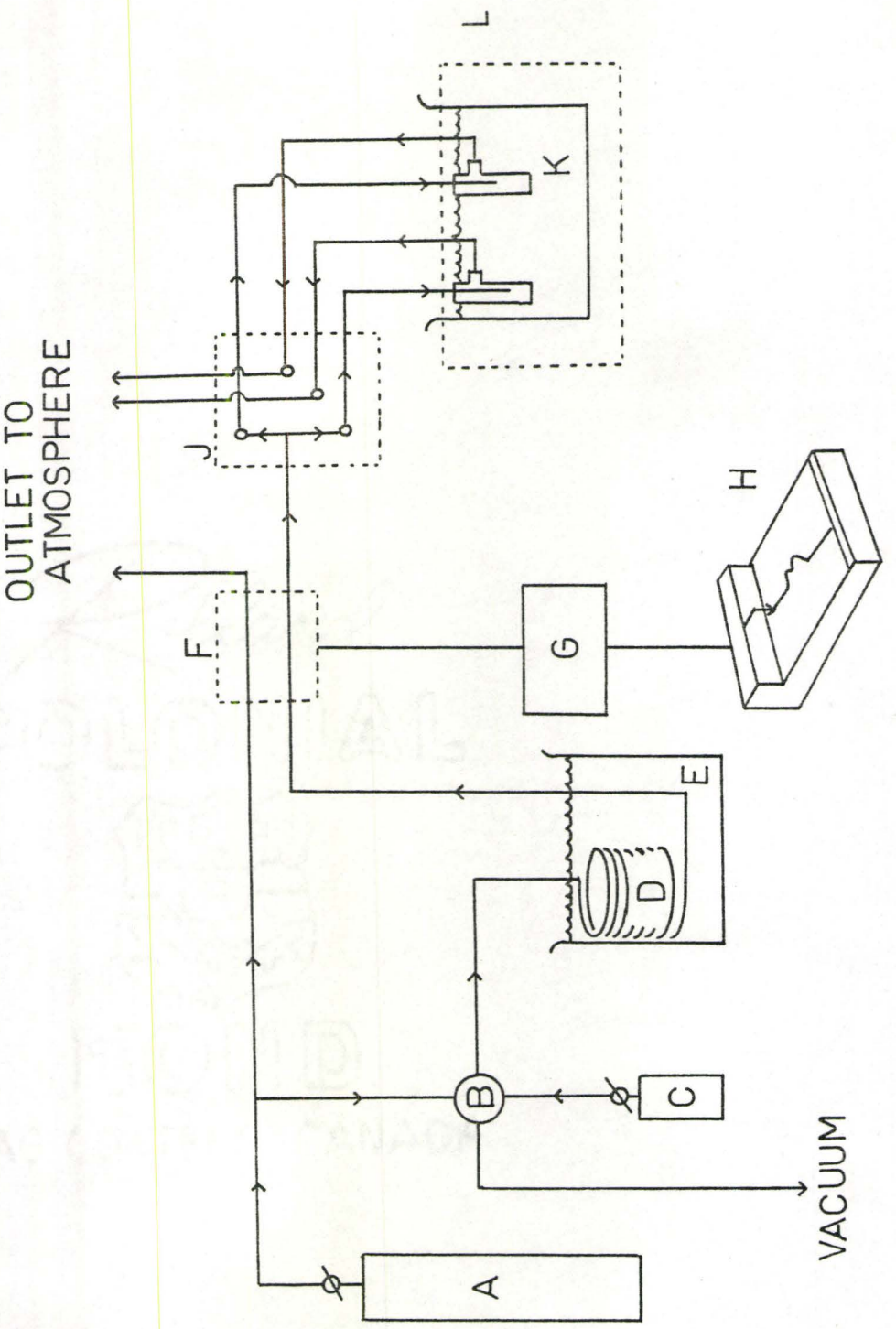
OUTLET TO ATMOSPHERE
L
K
J
H
F
G
E
D
B
C
A
VACUUM

As the samples were eluted from the column, they were detected with a pair of matched thermistor detectors, referenced to pure carrier gas. The amplified off-balance potential in the bridge circuit was indicated on a 10 mV range recorder.

Solenoid switches were used to divert the column outlet flow to a trap maintained at T = 77K and packed with Porapak Q® (Waters Assoc., Framingham, Mass.), where the desired portion of the eluted sample was retained. With the trap at T = 77K, the adsorbed carrier gas was pumped away, and the purified methane sample was recovered by subsequently warming the trap.

The column was operated at T = -78°C (acetone/dry ice) and helium was used as the carrier gas. Hydrogen has been reported to give slightly better isotopic separation[120], but residual traces of helium could be removed more easily than traces of hydrogen. An optimum separation was obtained at a carrier gas inlet pressure of 400 psig, as shown in Figure 14. There the van Deemter plot[121] is given, where

$$\text{HETP} = \text{height equivalent to theoretical plates}$$

$$= \frac{L}{N}$$

$$= \frac{L}{16}\left(\frac{w}{x}\right)^2 \qquad (14)$$

and where N is the number of theoretical plates, L is the column length, x is the sample retention time and w is the

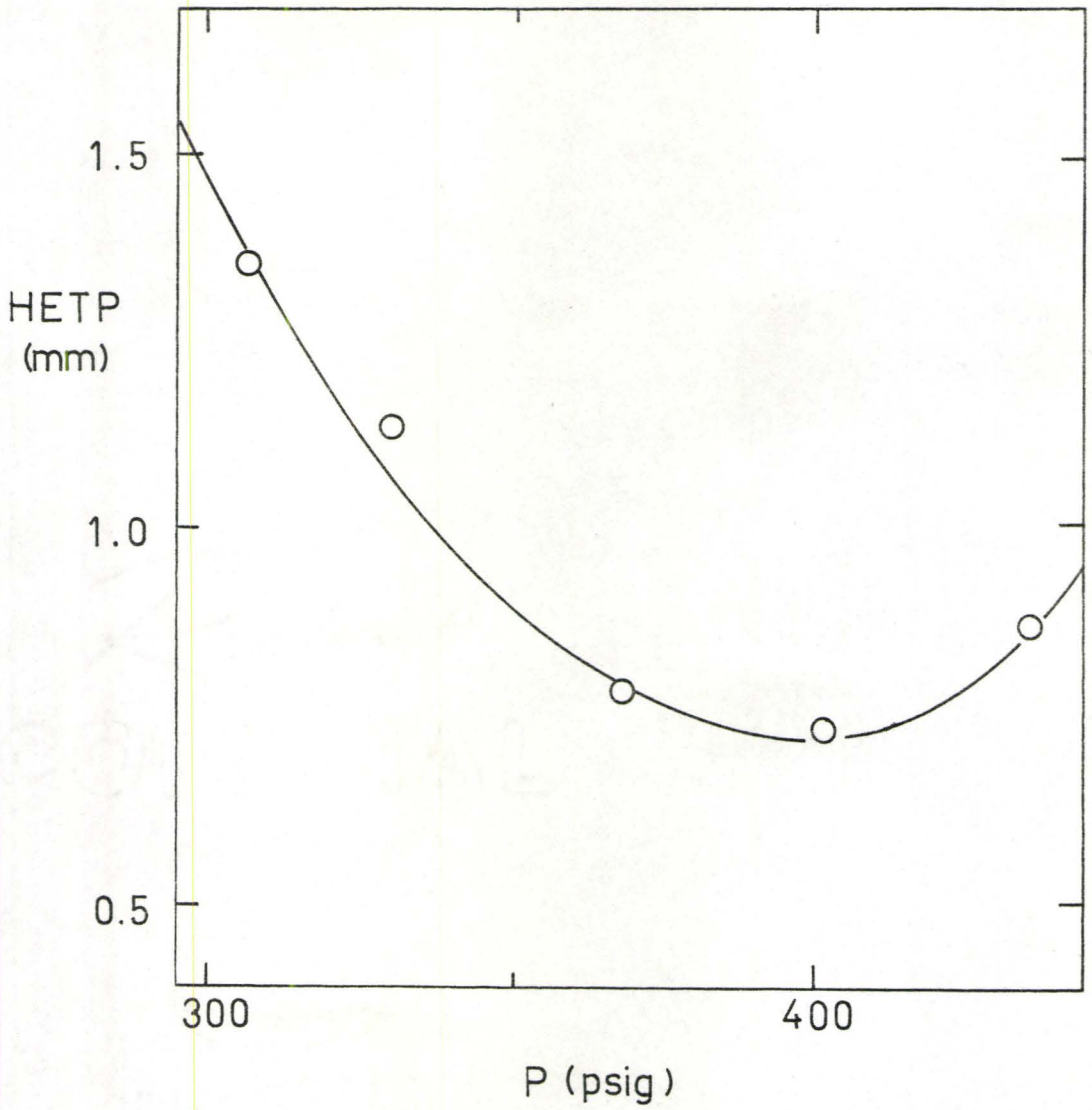

Figure 14: Van Deemter Plot for CH_4 Chromatographic Separation.

peak width at half peak height. Optimum separation is achieved at a minimum value of HETP. The maximum possible sample size for the column was reported to be 1 cm^3 (STP)[122], and this size was employed.

The long retention times ($\sim$ 5½ hours) for the deuteromethanes, combined with the large calorimetric specimen required ($\sim$ 100 cm^3 (STP) for CH_2D_2 and CHD_3; $\sim$ 200 cm^3 (STP) for CD_4) and the small yield of each injected sample ($\sim$ 0.4 cm^3 (STP)) made it necessary to stack the column with injected samples every 12 minutes. There was no interference between samples, and purified deuteromethane was thus collected at a rate of about 1 cm^3 (STP) per hour.

The commercially available deuterated methanes contain a few per cent of isotopic impurities.(See Table VII.) Since the chromatographic separation of the methanes is not complete, distinguishable peaks for each methane were not observed in the commercial samples, and appropriate mixtures were prepared to indicate the portion of the eluted peak that should be retained. In Figure 15(a) the separation of a 40:60 mixture of CH_3D in CH_2D_2 is illustrated. Note that the retention time is 325 minutes for CH_2D_2 and the lighter isotope is eluted about 3 minutes later. With this result as a guide, commercial CH_2D_2 was injected, and various "slices" of the eluted peak were analysed (see below). The final collected portion of the CH_2D_2 envelope is shown in Figure 15(b) as a cross-hatched area. Similar preliminary and final results for the CHD_3 and

Table VII

Composition of Methane Samples (mole %)[a]

Component	Commercial[b] CH_2D_2	Purified CH_2D_2	Commercial[b] CHD_3	Purified CHD_3	Commercial[b] CD_4	Purified CD_4
CH_4	< 0.2	< 0.2	< 0.3	< 0.2	< 0.2	< 0.2
CH_3D	2.2 ± 0.2	0.6 ± 0.2	< 0.2	< 0.2	< 0.2	< 0.2
CH_2D_2	97.8 ± 0.2	99.0 ± 0.2	5.4 ± 0.2	0.6 ± 0.2	< 0.2	< 0.2
CHD_3	< 0.2	< 0.2	94.6 ± 0.2	99.4 ± 0.2	3.4 ± 0.2	0.6 ± 0.2
CD_4	< 0.2	< 0.2	< 0.2	< 0.2	96.6 ± 0.2	99.4 ± 0.2
O_2	-	$< 3 \times 10^{-4}$	-	$< 3 \times 10^{-4}$	-	$< 3 \times 10^{-4}$
N_2	-	< 0.4	-	< 0.4	-	< 0.4

[a] Inequalities and errors quoted result respectively from detection limits and the mean deviation of several determinations.

[b] Merck, Sharp and Dohme, Montreal

Figure 15: The Chromatographic Separation of CH_2D_2.

(a) 40:60 mixture of CH_3D in CH_2D_2.

(b) Commercial CH_2D_2.

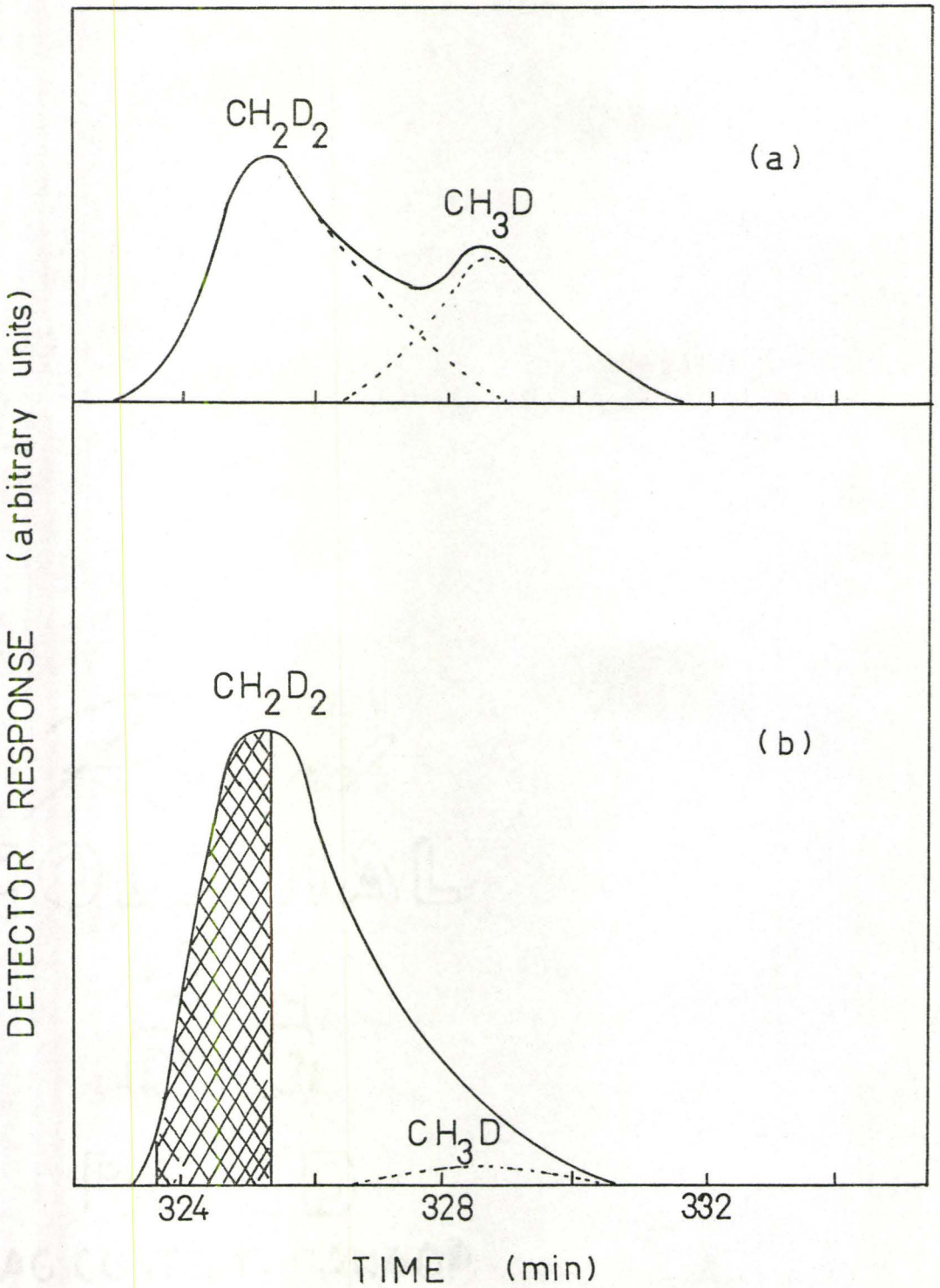
CH_2D_2
CH_3D
(a)
CH_2D_2
CH_3D
(b)
DETECTOR RESPONSE (arbitrary units)
324
328
332
TIME (min)

CD_4 purifications are given in Figures 16 and 17 respectively.

(b) Sample Analysis

The mass analyses of the CH_2D_2 and CHD_3 samples were performed at the University of Toronto on a modified EMI-52 magnetic-deflection single-focussing mass spectrometer. In the case of CH_2D_2, the electron beam energy was reduced until a constant 17:18 mass ratio was obtained; at this energy ($\sim$ 8 eV) the mass 18 peak was entirely due to $CH_2D_2^+$ and the mass 17 peak to CH_3D^+. Higher electron beam energies caused, for example, ambiguity in the assignment of the mass 17 source in CH_2D_2 (i.e. CHD_2^+ from CH_2D_2, or CH_3D^+ from CH_3D); more conventional mass spectrometry was thus precluded. In the case of CD_4 where the mass 20 and mass 19 peaks could be unequivocably assigned to CD_4^+ and CHD_3^+ respectively, mass analyses were carried out on a Hitachi-Perkin Elmer RMU-6A mass spectrometer. The isotopic compositions of the final calorimetric specimens are given in Table VII.

(c) Further Purification

Small traces of helium that had been introduced as carrier gas were removed when the sample was pumped at T = 4.2K to a pressure < 0.1 torr.

Finally, the sample was introduced into a diffuse-layer Misch metal getter to remove traces of O_2 and N_2. A thin film of this cerium-lanthanum alloy was flash-deposited

Figure 16: The Chromatographic Separation of CHD_3.

(a) 40:60 mixture of CH_2D_2 in CHD_3.

(b) commercial CHD_3.

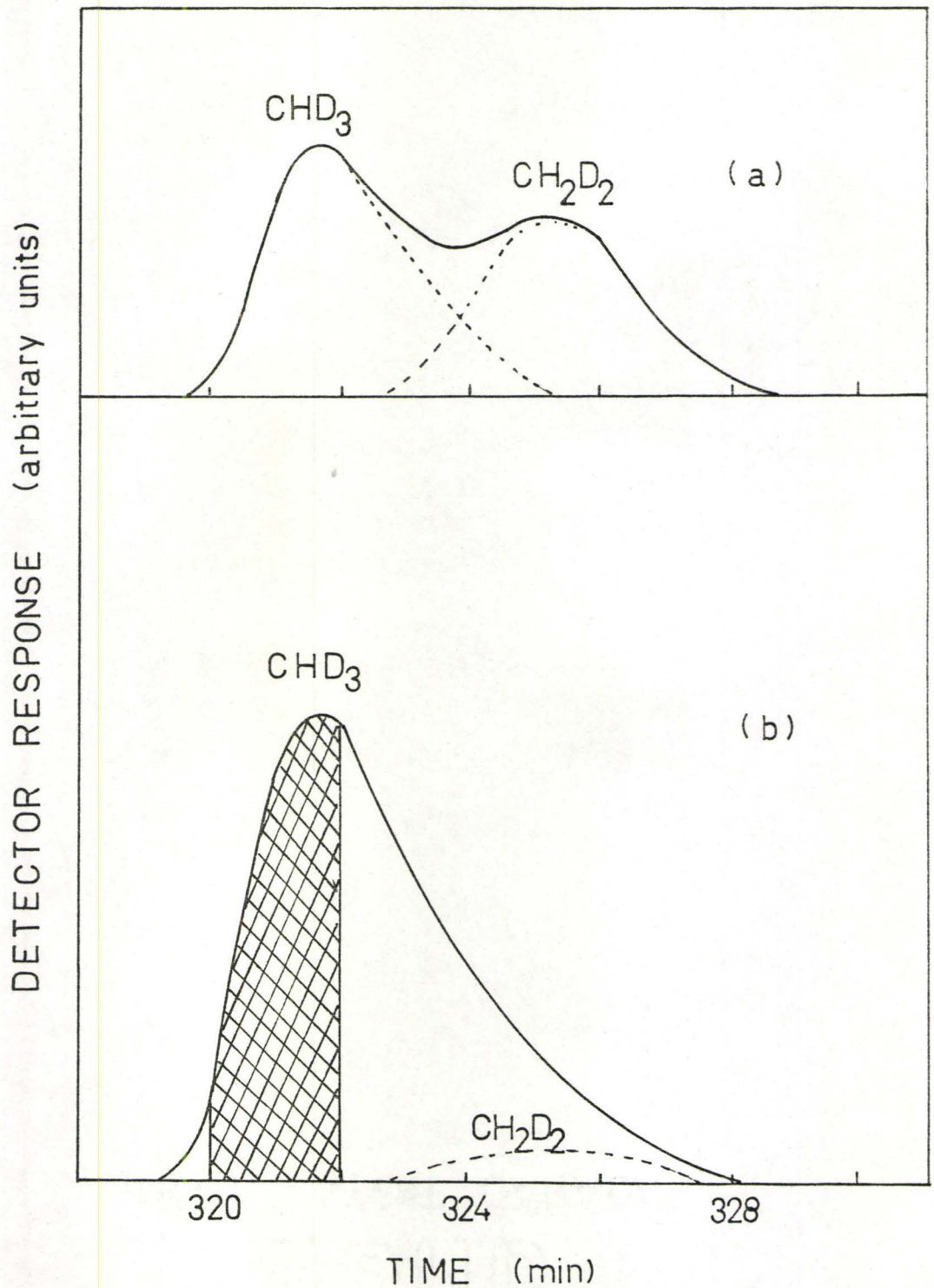
CHD3
CH2D2
(a)
CHD3
(b)
CH2D2
DETECTOR RESPONSE (arbitrary units)
320
324
328
TIME (min)

Figure 17: The Chromatographic Separation of CD_4.

(a) 40:60 mixture of CHD_3 in CD_4.

(b) commercial CD_4.

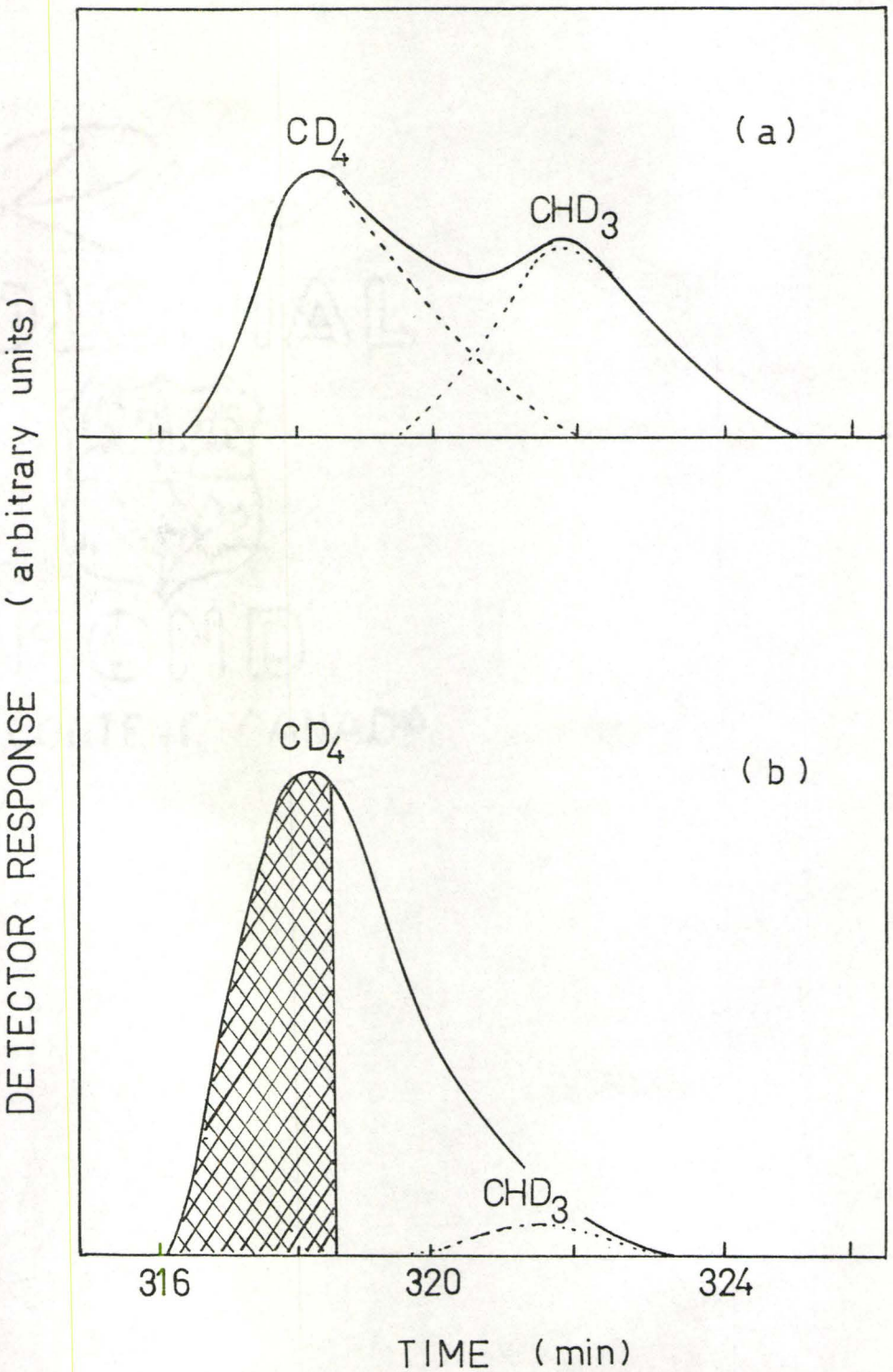
CD4
(a)
CHD3
CD4
(b)
CHD3
DETECTOR RESPONSE (arbitrary units)
316
320
324
TIME (min)

in an argon atmosphere (P $\sim$ 1-2 torr) and the argon was pumped out ($P<1x10^{-6}$ torr) before the methane was admitted. This method has been shown[123] to reduce the oxygen content in methane samples to less than 3 ppm. The sample was left on the getter overnight, and the nitrogen content, as deduced from the sample vapour pressure at T = 77K in comparison with that of pure methane[124], was typically reduced from a few per cent to $\lesssim$ 0.4%.

All samples were handled in a high vacuum line for transfer into the calorimeter vessel.

2. Calorimetry

(a) The Calorimetric Vessel

The aims of the present work were to measure the heat capacities of isotopically purified CH_2D_2, CHD_3 and CD_4 with as great precision and accuracy, and to as low a temperature as possible. To this end, a special calorimeter vessel was used.

The vessel (shown in Figure 18) was principally made of copper and had a total mass of $\sim$ 70 g and an internal volume of $\sim$ 120 cm^3. It was designed to be filled outside of the cryostat. This eliminated problems associated with sample sublimation and solidification in filling lines in the more common type of filling arrangement. The vessel filling port was closed with a stainless steel needle valve (shown in Figure 18) which could be manipulated through a

Figure 18: The Calorimeter Vessel.

A - gold-plated copper wire

B - stainless steel screw

C - filling port

D - suspension rings

E - constantan heater wire

F - germanium thermometer

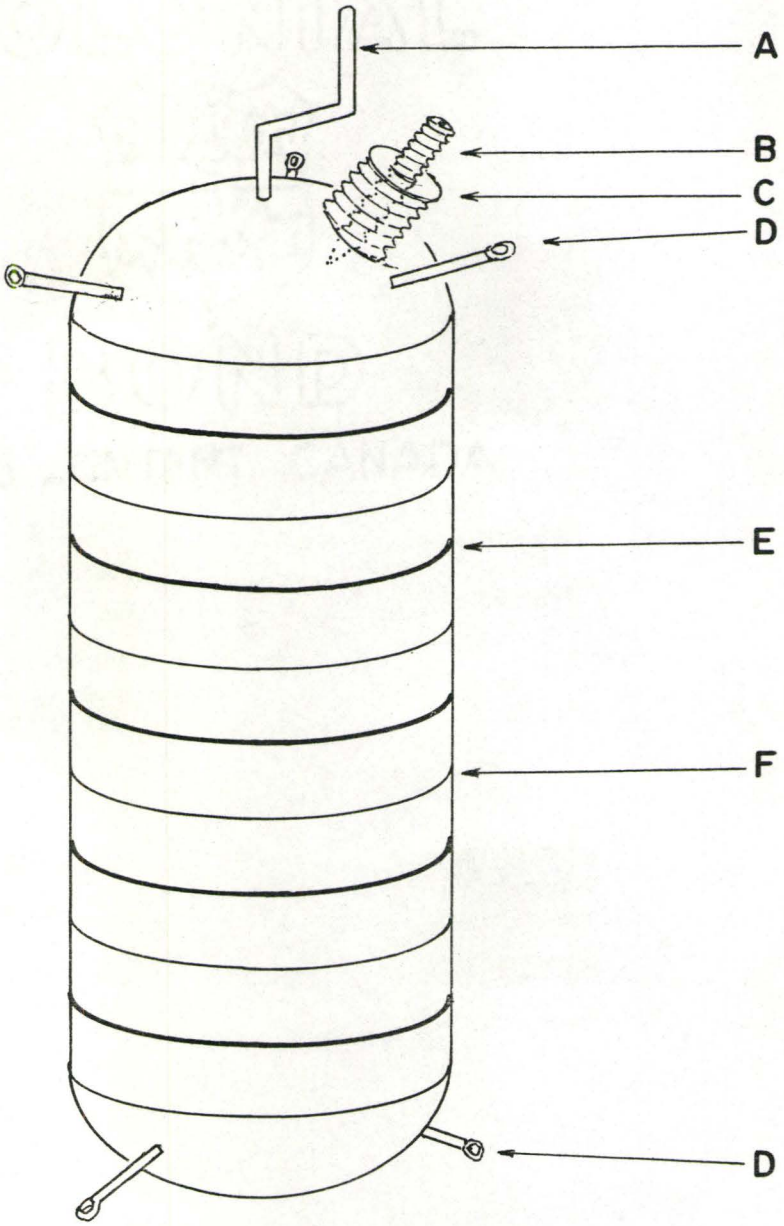
A
B
C
D
E
F
D

detachable seal that screwed on to the filling port and was directly attached to the filling line.

The heat capacity of the empty calorimeter vessel was initially measured[79,81,114] with the needle valve open to ensure that the vessel was thoroughly evacuated. The measurements gave rise to a troublesome effect (a sample heat capacity that was apparently slightly larger than that observed previously[76]) because of poor thermal contact between the needle valve and its housing. The effect was similar to a linear contribution to the heat capacity that was observed[125] in ^{3}He and ^{4}He films, and was initially[126] interpreted as due to a dimensional effect associated with the sample thickness. It was ultimately proved that it arose from an omission in the heat capacity of the vessel (viz. the heat capacity of the needle valve.) This was surprising since it was expected that there would be adequate thermal contact between the needle valve and the vessel through the screw threads. Moreover, the contact would improve as the temperature was lowered because the needle valve was made of steel and its mounting block of brass. In addition, the mass of the needle valve is only $\sim$ 1% of the total mass, but, because the coefficient of the electronic term in the heat capacity of this steel is so large, the needle valve contributes roughly 20 to 25% to the total heat capacity of the vessel. When the heat capacity of the evacuated calorimeter vessel was measured with the valve closed, the discrepancy between the

determinations[76,79,81,114] of the methane heat capacity was eliminated.[127]

The heat capacity of the empty calorimeter vessel is approximately linear in T, and a value of $\sim 1.5 \times 10^{-3}$ J K^{-1} at T = 1.0K can be used to judge its contribution to the total. The heat capacity of the empty calorimeter was measured for $0.13K \leq T \leq 3.8K$, and was known to a precision of ± 2% or better.

(b) Thermometry and Temperature Measurement

A nitrogen-filled germanium resistance thermometer (Cryo Cal Inc.) was used in the calorimetric measurements to be described in this thesis. The thermometer had been previously[79,80] calibrated against ^3He and ^4He vapour pressure thermometers at 121 points for $1.07K \leq T \leq 4.3K$, and a relationship between the resistance, R, and the temperature, T, of the form

$$\ln R + \frac{A}{\ln R} + \frac{B}{(\ln R)^2} + C + \frac{D}{T} = 0 \qquad (15)$$

was found, where A = 34.3303, B = -38.9865, C = -10.0897 and D = -0.215482K. The calibration points fitted expression (15) to an average deviation of 1.5×10^{-3}K, and a maximum deviation of 4.6×10^{-3}K.

The thermometer was also intercompared[79,80] with a second germanium thermometer (Model 5A, Scientific Instruments, Inc.) that had been calibrated for $0.05K \leq T \leq 3.2K$ to a

claimed accuracy of ± 5 x 10^{-3}K, and with a nuclear orientation thermometer (The Oxford Instrument Co. Ltd.) in the form of a single crystal of cobalt that contained ^{60}Co. The agreement was better than ± 5 x 10^{-3}K between the germanium thermometers in the region 1K ≤ T ≤ 3.2K, but systematic deviations existed below T = 1K. However, extrapolation of equation (15) to T = 0.08K gave temperatures in agreement with the nuclear orientation thermometer to within 8 x 10^{-4}K, and the discrepancy with the second germanium thermometer was attributed to a temperature gradient during its initial calibration[128]. Indirect confirmation of the accuracy and reliability of the present thermometer was obtained through the measurements of the heat capacity of vacuum melted high purity copper[79] and very dilute alloys of cerium in aluminum[129]

The absolute value of the temperature was therefore accurate to ± 5 x 10^{-3}K or better throughout the entire temperature region of the present experiments (0.1K ≤ T ≤ 3.8K.) In heat capacity measurements, however, temperature differences are more important than absolute values of the temperature; here ΔT was known to within 1 x 10^{-3}K.

The resistance of the thermometer was determined by a simple DC method. The voltage across the thermometer was measured in both directions (to take account of thermal emfs), and compared with the voltage across a reference resistance (known to ± 0.01% or better.) The thermometer current could

be varied between 0.1μA and 20μA and was chosen to give minimum heating of the thermometer with maximum measurement sensitivity. The potentials were amplified, measured with a digital voltmeter to 5 significant figures, and recorded by a mechanical printer.

(c) Mounting of the Calorimeter Vessel

The calorimeter vessel was loaded in a Mark V helium dilution refrigerator (The Oxford Instrument Co. Ltd.)[130] which had a nominal cooling power of 200 erg sec^{-1} at T = 0.1K.

The dilemma of low temperature heat capacity measurements is that the calorimeter must be in sufficient thermal contact with the cold parts of the refrigerator to be cooled, yet heat exchange with the calorimeter must be minimized during the measurements. The problem was resolved here through the use of a mechanical heat switch. The gold-plated copper wire connected to the top of the vessel, as shown in Figure 18, was gripped, as required, by the gold-plated copper jaws of a heat switch. A wire, attached to the switch and to a screw at the top of the cryostat, allowed the external operation of the switch. The jaws of the heat switch were connected to the mixing chamber of the refrigerator with heavy but flexible copper braid.

In order to minimize the heat leak to the vessel during measurements, spring-loaded nylon filaments (2 lb test), which gave strength with minimum thermal conductivity, were

used to position the vessel in a sturdy frame that was suspended from the mixing chamber. The electrical leads that were brought into the cryostat were enamel and silk-covered constantan ($\sim$ 20 Ω ft^{-1}). They were thermally anchored to the main helium container (T = 4.2K) and to the pumped helium pot (T = 1.2K) before they were wrapped around a copper ring that was attached to the mixing chamber. Between the mixing chamber and the vessel, the leads were Pb-covered manganin which had the desirable property of becoming superconducting for T < 7K.[31] The apparatus was mounted on blocks on a basement floor and, during heat capacity measurements, movement in the laboratory was restricted in order to reduce extraneous heating through mechanical vibration.

At temperatures below 0.25K, cooling was exceptionally slow (< 5 x 10^{-3}K hr^{-1}) through the heat switch alone and so, for measurements in this temperature region, a thermal link (6.5 cm of #36 AWG copper wire) was attached between the calorimeter vessel and the copper braid of the mixing chamber. This increased the rate of cooling of the calorimeter vessel but not to the extent that it decreased significantly the accuracy with which the heat capacity measurements could be made. In the region 0.5K $\leq$ T $\leq$ 0.9K, the observed thermal conductance could be fitted to the simple expression

$$h = 0.2\ T^4\ (W\ cm^{-2}\ K^{-1}) \quad . \qquad (16)$$

It is similar to that which has been reported[132] for Kapitza boundary-limited conductance for a junction of super-conducting tin to copper:

$$h = 0.11\ T^3\ (W\ cm^{-2}\ K^{-1}), \qquad (17)$$

or of superconducting lead to copper,

$$h = 0.09\ T^4\ (W\ cm^{-2}\ K^{-1}) . \qquad (18)$$

(d) Measurement Techniques and Error Analysis

The heat capacity was measured by the heat pulse method. The temperature was followed before and after the pulse, and ΔT was derived from an extrapolation of the temperatures to the mid-point of the heating period. Typically, the heat pulse lasted 20-30 sec and the temperature drifts were 10^{-5} to 5×10^{-5} K sec^{-1}. The temperature drifts depended on whether the heat switch was open (as it generally was for $T \gtrsim 0.4K$) or closed (as it was for $T \lesssim 0.4K$), and also on the presence or absence of the thermal link.

The extrapolated temperatures could generally be determined to within a few mK at worst, and the energy input could be measured to better than ± 0.1%. As mentioned earlier, the calorimeter vessel heat capacity was known to ± 2%. In the results section, uncertainties will be given for each point, based principally on estimated uncertainties in ΔT and in the vessel heat capacity. The errors quoted are ± 2 standard deviations (i.e. outside limits).

Part B: Results

The heat capacities of isotopically purified CH_2D_2, CHD_3 and CD_4 were measured in the region $0.15K \leq T \leq 3.0K$. The results for the three methanes will be presented in turn.

1. CH_2D_2

The measured heat capacities of 2.594×10^{-3} moles of isotopically purified CH_2D_2 (purity as in Table VII) are given in order of determination in Table VIII. It should be noted that the agreement between the measurements made with and without the thermal link is excellent. The uncertainties quoted are 2 standard deviations, as discussed in Section III.A.2.d. In the measurements, the calorimeter heat capacity accounted for 3% of the total at the lowest temperature, 80% of the total at the highest temperature, and 35% of the total at T = 1.0K.

The heat capacity of "pure" CH_2D_2 was calculated from the raw data under the assumption that the CH_3D contribution (taken from the data of Ref. 79 for "pure" CH_3D) was strictly additive. The data for "pure" CH_2D_2 are shown in Figure 19 and are compared with Colwell's results.[76] The agreement is well within the experimental errors, except at the lowest temperatures ($T < 0.5K$). Such a systematic difference was noted previously[79]; the present results should have preference both because of the extremely careful thermometer calibration and because the measurements were made on an isotopically purified sample. Smoothed values

Table VIII

Measured Heat Capacities of CH_2D_2

T(K)	C_p^a/R	Uncertainty[b] in Cp/R
0.720	0.3782	0.002
0.284	0.9004	0.016
0.331	0.8182	0.016
0.387	0.7042	0.011
0.498	0.5426	0.004
0.660	0.4130	0.005
0.861	0.3122	0.006
1.051	0.2502	0.007
1.223	0.2127	0.005
1.404	0.1827	0.008
1.588	0.1541	0.005
1.766	0.1314	0.004
1.952	0.1136	0.006
2.181	0.0964	0.006
2.441	0.0816	0.007
2.677	0.0678	0.008
0.228	0.8991	0.011
0.261	0.9145	0.026
0.291	0.8802	0.016
0.324	0.8295	0.018

continued ...

Table VIII continued

T(K)	c_p^a/R	Uncertainty[b] in Cp/R
0.356	0.7590	0.020
0.388	0.7062	0.025
0.419	0.6489	0.050
1.398	0.1826	0.002
1.425	0.1772	0.004
1.447	0.1757	0.007
0.961	0.2822	0.002
1.154	0.2289	0.002
1.346	0.1924	0.002
1.534	0.1579	0.005
1.726	0.1354	0.007
1.915	0.1163	0.006
2.097	0.1013	0.008
0.941	0.2843	0.003
1.117	0.2387	0.002
1.306	0.1989	0.004
1.507	0.1640	0.005
1.712	0.1350	0.009
1.914	0.1172	0.005
2.112	0.0988	0.007

continued ...

Table VIII continued

T(K)	C_p^c/R	Uncertainty[b] in Cp/R
0.161	0.673	0.022
0.134	0.533	0.058
0.158	0.659	0.025
0.184	0.779	0.026
0.208	0.909	0.074
0.228	0.928	0.096
0.240	0.952	0.054
0.255	0.956	0.038
0.360	0.808	0.036
0.294	0.943	0.040
0.259	0.963	0.050
0.196	0.831	0.033
0.197	0.821	0.030
0.143	0.572	0.030
0.166	0.701	0.030
0.192	0.818	0.041
0.215	0.925	0.055
0.230	0.898	0.033
0.237	0.926	0.058

[a] Measurements made without copper wire link.
[b] See section III.A.2.d for discussion of errors.
[c] Measurements made with copper wire link attached.

Figure 19: The Heat Capacity of Pure CH_2D_2.

o Present Measurements.

—— From Ref. 76.

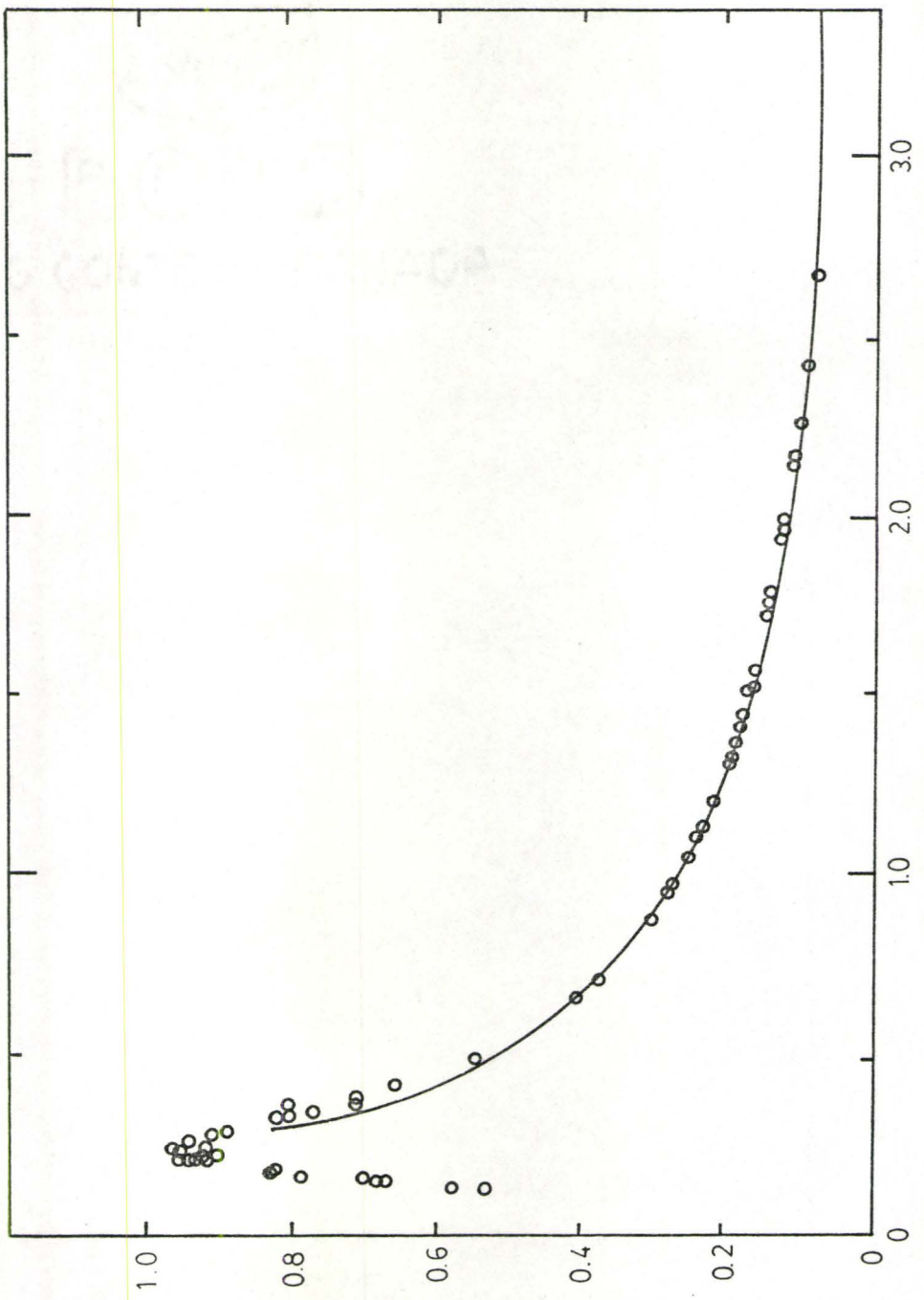
1.0
0.8
0.6
0.4
0.2
0
C_p/R
0
1.0
2.0
3.0
T (K)

of the present results for "pure" CH_2D_2 are given in Table IX.

The measurements showed the same thermal relaxation as was observed for the empty calorimeter vessel ($\tau < 5$ sec.) This is to be contrasted with Colwell's observation[76] of a thermal relaxation in CH_2D_2 similar to that observed in CH_3D ($\tau \gtrsim 60$ sec.) It was suggested[76] that this long relaxation could be due to either nuclear spin species conversion in CH_2D_2, or to the presence of CH_3D impurity; it appears now that the latter was the cause. The present sample was kept at $T \lesssim 4K$ for periods longer than 2 weeks without any detectable change in the heat capacity. It is thus unlikely that very slow conversion occurred. Although very fast conversion ($\tau << 1$ sec.) cannot be ruled out by the absence of observable thermal relaxation processes, entropy arguments to be presented in the next chapter make this seem unlikely in CH_2D_2.

2. CHD_3

The measured heat capacities of 3.367×10^{-3} moles of isotopically purified CHD_3 (purity as in Table VII) are given in order of measurement in Table X. Again, the agreement between the measurements made with and without the thermal link is excellent. The heat capacity of the vessel comprised $\sim$ 7% of the total at the lowest temperature, $\sim$ 80% of the total at the highest temperature, and $\sim$ 17% at T = 1.0K.

Table IX

Smoothed Values of the Heat Capacity of Pure CH_2D_2

T(K)	Cp/R
0.14	0.552
0.16	0.660
0.18	0.764
0.20	0.870
0.22	0.932
0.24	0.942
0.26	0.931
0.28	0.906
0.30	0.875
0.35	0.777
0.40	0.667
0.45	0.581
0.50	0.522
0.60	0.441
0.70	0.384
0.80	0.338
0.90	0.300
1.00	0.267
1.50	0.162
2.00	0.108
2.50	0.075
3.00	0.060

Table X

Measured Heat Capacities of CHD_3

T(K)	C_p^a/R	Uncertainty[b] in Cp/R
0.402	0.5560	0.0052
0.453	0.5815	0.0098
0.496	0.5903	0.0093
0.536	0.5745	0.0118
0.581	0.5479	0.0117
0.598	0.5428	0.0175
0.637	0.5060	0.0108
0.685	0.4755	0.0153
0.734	0.4502	0.0079
0.792	0.4109	0.0076
0.851	0.3672	0.0060
0.905	0.3232	0.0081
0.973	0.3039	0.0062
1.027	0.2805	0.0077
1.075	0.2528	0.0109
0.996	0.2903	0.0092
1.105	0.2474	0.0063

continued ...

Table X continued

T(K)	C_p[a]/R	Uncertainty[b] in Cp/R
1.227	0.2047	0.0058
1.360	0.1727	0.0060
1.531	0.1397	0.0058
1.737	0.1103	0.0061
1.950	0.0883	0.0076
2.201	0.0708	0.0083
2.476	0.0605	0.0093
2.764	0.0480	0.0101
0.495	0.5913	0.0086
0.529	0.5710	0.0103
0.562	0.5597	0.0100
0.597	0.5357	0.0101
0.636	0.5167	0.0066
0.677	0.4909	0.0168
0.732	0.4467	0.0076
0.794	0.3930	0.0078
0.841	0.3686	0.0061

continued ...

Table X continued

T(K)	C_p^c/R	Uncertainty[b] in Cp/R
0.308	0.459	0.0045
0.355	0.520	0.0054
0.404	0.568	0.0041
0.456	0.577	0.0050
0.503	0.576	0.0106
0.191	0.313	0.0081
0.219	0.338	0.0079
0.248	0.383	0.0096
0.276	0.419	0.0040
0.315	0.463	0.0073
0.357	0.523	0.0116
0.388	0.550	0.0138
0.168	0.291	0.0051
0.197	0.321	0.0073
0.228	0.356	0.0074
0.260	0.393	0.0087
0.291	0.438	0.0068
0.323	0.486	0.0066
0.358	0.524	0.0086

a Measurements made without copper link.
b See Section III.A.2.d. for discussion of errors.
c Measurements made with copper wire link attached.

The heat capacity of "pure" CHD_3 was calculated from the raw data under the assumption that the contribution of the CH_2D_2 impurity (taken from the data of the previous section for "pure" CH_2D_2) was additive. The data for "pure" CHD_3 from both the present work and Colwell's measurements[76] are illustrated in Figure 20. The agreement is well within the experimental errors, except for the region $T < 0.5K$, and again the present results are to be preferred. It should be noted that the measurements indicate the presence of some structure on the low temperature side of the Schottky anomaly; this proves to be important in the analysis of C_p/R to obtain estimates of the tunneling levels, as will be discussed in the next chapter. Smoothed values of the heat capacity of pure CHD_3 are given in Table XI.

The CHD_3 sample showed thermal relaxation similar to that of CH_2D_2. That is to say, thermal relaxation was normal and yielded no evidence for conversion.

3. CD_4

The heat capacity of 7.627×10^{-3} moles of isotopically purified CD_4 (purity as in Table VII) is given in Table XII in order of measurement. Again, there is good agreement between the determinations made with and without the copper wire thermal link.

The uncertainties quoted in Table XII are again ± 2 standard deviations (as discussed in Section III.A.2.d), but

Figure 20: The Heat Capacity of Pure CHD_3

o Present Measurements.

—— From Ref. 76.

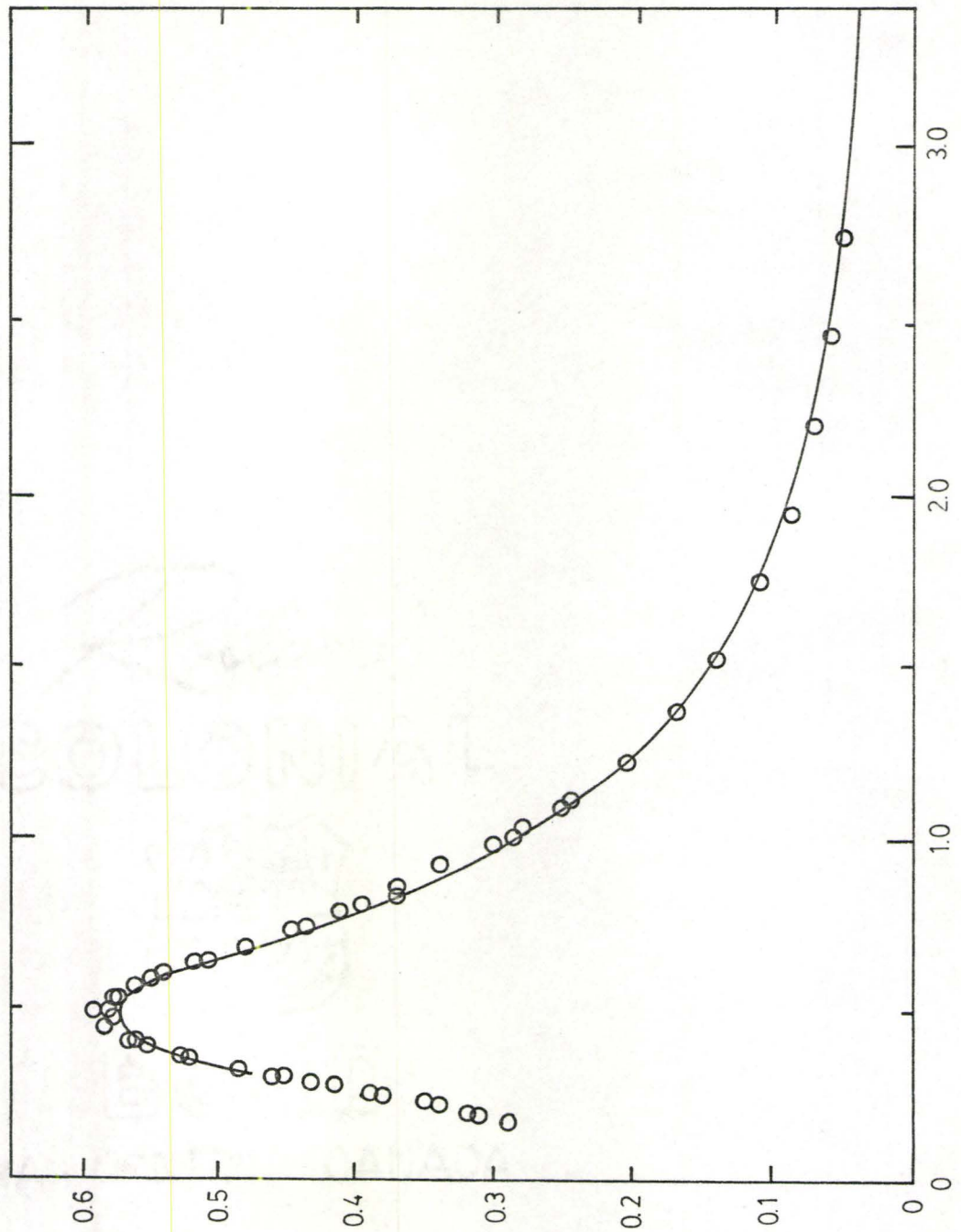
0.6
0.5
0.4
0.3
0.2
0.1
0
C_p/R
0
1.0
2.0
3.0
T (K)

Table XI

Smoothed Values of the Heat Capacity of Pure CHD_3

T(K)	Cp/R
0.14	0.242
0.16	0.276
0.18	0.301
0.20	0.323
0.22	0.343
0.24	0.367
0.26	0.392
0.28	0.420
0.30	0.448
0.35	0.512
0.40	0.561
0.45	0.579
0.50	0.582
0.60	0.535
0.70	0.469
0.80	0.400
0.90	0.339
1.00	0.288
1.50	0.141
2.00	0.081
2.50	0.055
3.00	0.041

Table XII

Measured Heat Capacities of CD_4

T(K)	C_p^a/R	Uncertainty[b] in Cp/R
0.420	2.85×10^{-3}	3×10^{-4}
0.889	1.38×10^{-3}	9×10^{-4}
1.018	1.10×10^{-3}	7×10^{-4}
1.153	2.14×10^{-3}	8×10^{-4}
1.288	2.48×10^{-3}	9×10^{-4}
1.486	1.18×10^{-3}	1×10^{-3}
1.726	3.12×10^{-3}	1×10^{-3}
1.961	2.81×10^{-3}	2×10^{-3}
0.237	3.83×10^{-3}	7×10^{-4}
0.279	3.53×10^{-3}	9×10^{-4}
0.317	2.77×10^{-3}	7×10^{-4}
0.384	2.70×10^{-3}	5×10^{-4}
0.477	2.45×10^{-3}	3×10^{-4}
0.578	2.07×10^{-3}	3×10^{-4}
0.677	1.65×10^{-3}	5×10^{-4}

continued ...

Table XII continued

T(K)	C_p/R[a]	Uncertainty[b] in Cp/R
0.772	1.62×10^{-3}	6×10^{-4}
0.873	1.65×10^{-3}	8×10^{-4}
0.976	1.08×10^{-3}	1×10^{-3}
1.129	1.70×10^{-3}	5×10^{-4}
1.304	2.35×10^{-3}	1×10^{-3}
1.473	1.91×10^{-3}	1×10^{-3}
1.672	2.36×10^{-3}	1×10^{-3}
1.884	2.37×10^{-3}	1×10^{-3}
2.100	3.02×10^{-3}	7×10^{-4}
2.325	2.80×10^{-3}	2×10^{-3}
2.594	3.74×10^{-3}	2×10^{-3}
2.868	5.37×10^{-3}	3×10^{-3}
3.258	8.32×10^{-3}	3×10^{-3}
3.217	8.01×10^{-3}	3×10^{-3}
3.585	1.17×10^{-2}	4×10^{-3}
3.879	1.58×10^{-2}	4×10^{-3}
3.763	1.41×10^{-2}	6×10^{-3}

continued ...

Table XII continued

T(K)	C_p^c/R	Uncertainty[b] in Cp/R
0.162	4.12×10^{-3}	4×10^{-4}
0.165	7.97×10^{-3}	3×10^{-4}
0.169	6.99×10^{-3}	1×10^{-3}
0.175	5.82×10^{-3}	6×10^{-4}
0.180	4.52×10^{-3}	6×10^{-4}
0.186	5.44×10^{-3}	8×10^{-4}
0.188	6.06×10^{-3}	6×10^{-4}
0.203	6.33×10^{-3}	6×10^{-4}
0.214	5.42×10^{-3}	8×10^{-4}
0.229	5.16×10^{-3}	5×10^{-4}
0.257	3.67×10^{-3}	6×10^{-4}
0.159	7.59×10^{-3}	4×10^{-4}
0.164	7.35×10^{-3}	6×10^{-4}
0.171	8.00×10^{-3}	5×10^{-4}
0.176	6.85×10^{-3}	8×10^{-4}
0.192	6.44×10^{-3}	6×10^{-4}

[a] Measurements made without copper wire link.

[b] Errors quoted based on ±2 standard deviations (See Section III.A.2.d)

[c] Measurements made with copper wire link attached.

are considerably larger than those for the CH_2D_2 and CHD_3 measurements. There are two main reasons for this: the calorimeter vessel now accounts for 50-95% of the total heat capacity and, at the lowest temperatures ($T < 0.3K$), unusually small ($\sim 0.010K$) ΔT values were used in order to delineate the rapid rise in heat capacity.

The results are illustrated in Figure 21 and compared with two sets of earlier measurements.[39,76] The three separate determinations clearly converge as the temperature increases towards 4K but, below that, the earlier measurements indicate a much higher heat capacity. The discrepancy is principally due to the impurity contributions to the heat capacity in the earlier work; Colwell's measurements[76] clearly reflect the shape of the anomaly in the heat capacity of CHD_3. As judged by its heat capacity at $T = 0.5K$, where the CHD_3 impurity would have its maximum contribution, the present specimen probably contained $< 0.4\%$ CHD_3. Smoothed values of the heat capacity of "pure" CD_4, based on 0.4% CHD_3 impurity in the measured sample, are given in Table XIII.

A very interesting feature of the present measurement was the observed rise in the heat capacity for $T \lesssim 0.3K$. The nature and origin of the anomaly will be discussed in detail in the next chapter.

In contrast with the CH_2D_2 and CHD_3 measurements, distinct thermal relaxation processes were observed in the heat capacity of CD_4. The relaxation was exponential and

Figure 21: The Heat Capacity of CD_4.

o Present Measurements.

● From Ref. 76.

× From Ref. 39.

···· Heat Capacity Contribution Due to 0.4% CHD_3 in Sample.

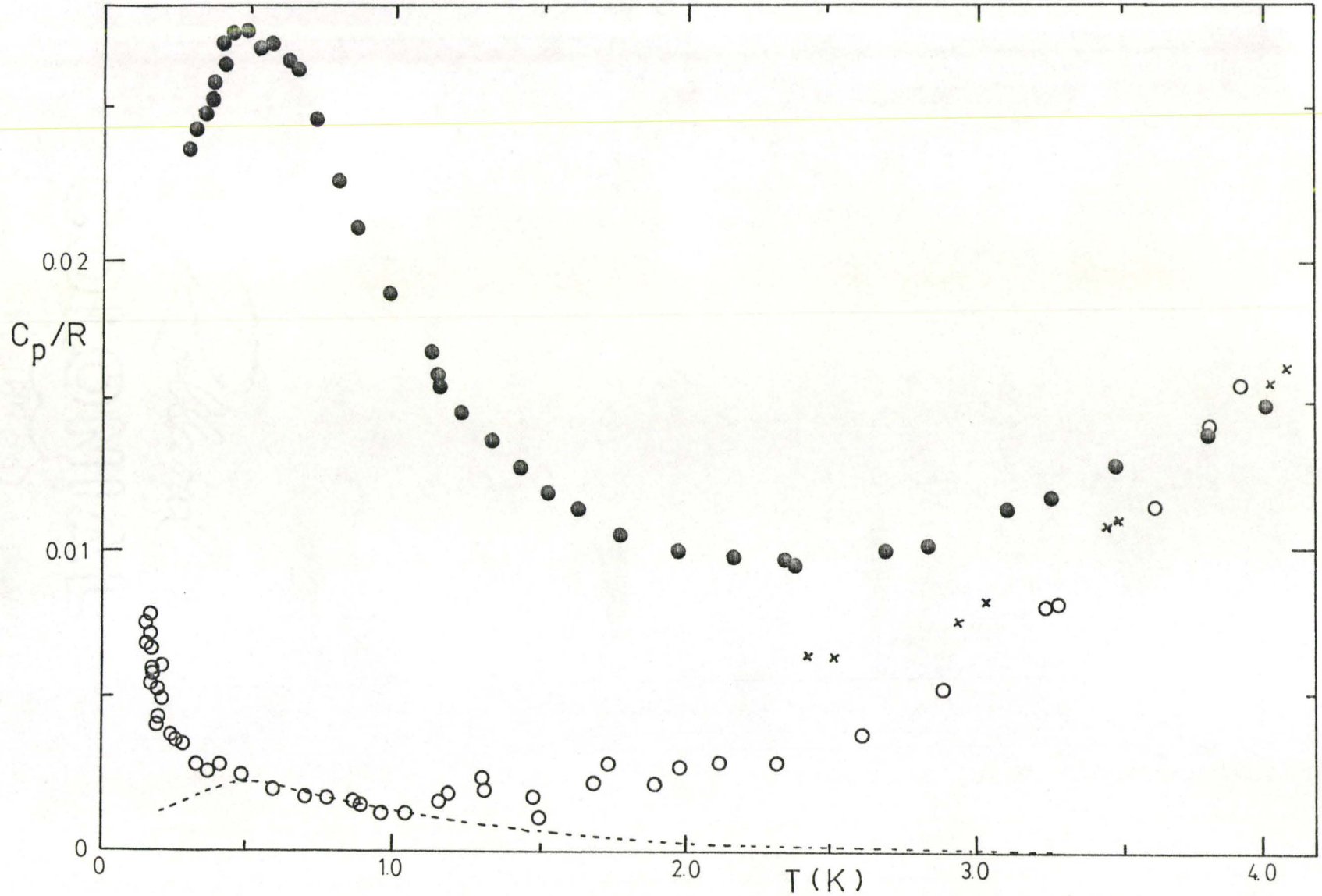
0.02
0.01
0
C_p/R
0
1.0
2.0
3.0
4.0
T (K)

Table XIII

Smoothed Values of the Heat Capacity of Pure CD_4

T(K)	Cp/R
0.17	0.0066
0.20	0.0030
0.30	0.0016
0.40	0.0004
0.50	0.0002
1.0	0.0002
1.5	0.0010
2.0	0.0019
2.5	0.0028
3.0	0.0058
3.5	0.0109
4.0	0.0163

can be expressed in terms of a relaxation time, τ. As shown in Figure 22, τ rises rapidly for $T \lesssim 0.2K$, and is about 12 sec at the lowest temperature measured. The most probable conclusion is that nuclear spin species conversion occurs in CD_4.

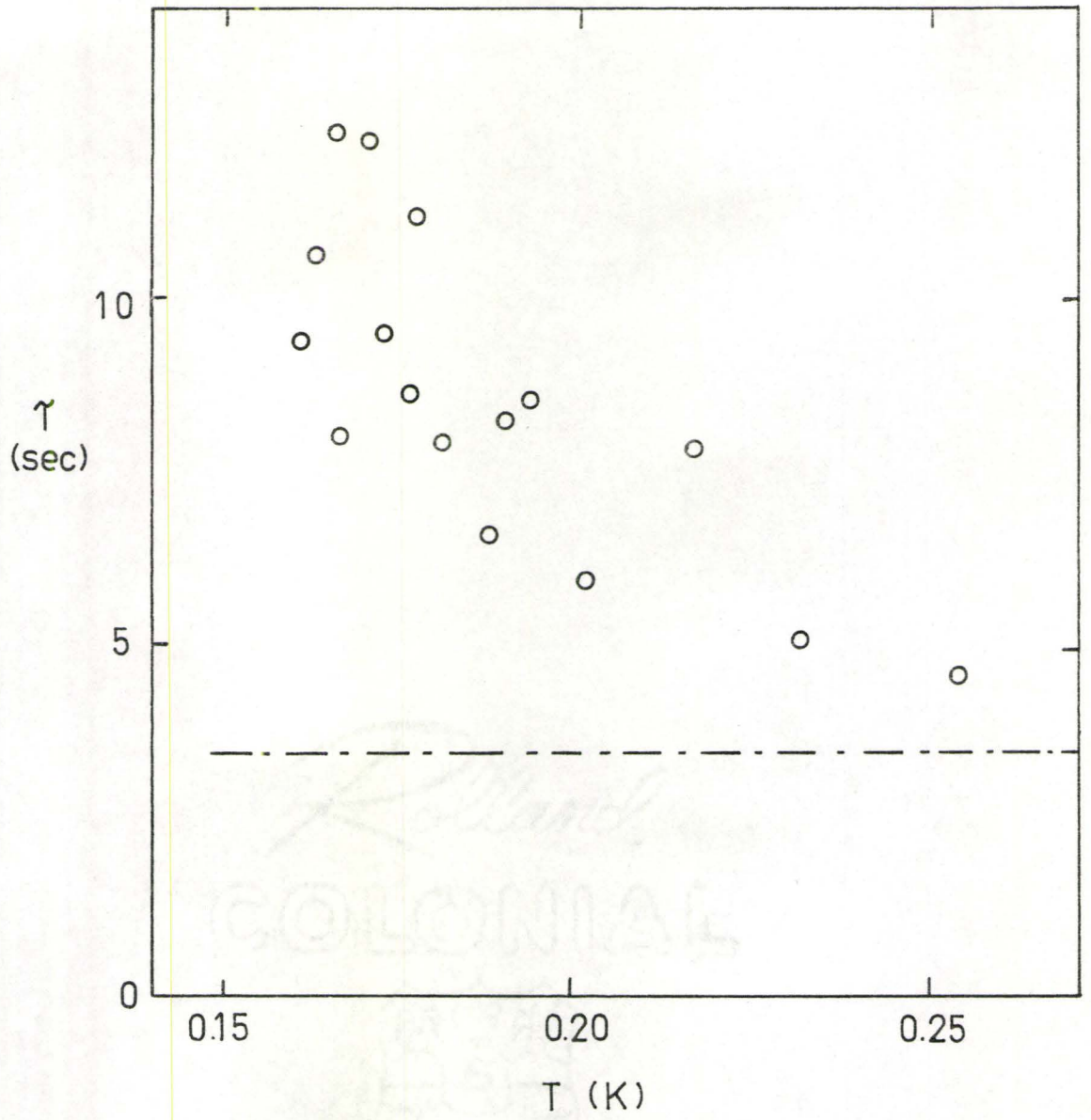

Figure 22: Thermal Relaxation Times in the CD_4 Sample.

o CD_4 relaxation time.

—·— Relaxation time of the empty calorimeter vessel.

CHAPTER IV

DEDUCTIONS ABOUT THE STRUCTURE OF PHASE III AND TUNNELING STATES IN THE SOLID ISOTOPIC METHANES

Part A: Low Temperature Entropy and Ordering in the Solid Methanes

1. The Lattice Contribution to the Entropy

As mentioned earlier, the low temperature entropy of the deuterated methanes can yield information about the ordering that takes place in phase III. It is of particular interest to see the contribution to the entropy from the Schottky anomalies, but first one must know the nature of the lattice heat capacity in order to subtract its contribution from the measured heat capacity.

At low temperatures, the lattice heat capacity of an insulator can be described by a power series of the form

$$C_v = a\,T^3 + b\,T^5 + c\,T^7 + \ldots, \qquad (19)$$

in which the coefficients a, b and c are directly related to the coefficients in the corresponding power series for the frequency spectrum at low frequencies.[133] (It should be noted that the quantity that is measured calorimetrically

for a condensible solid is C_{sat}, the heat capacity of the solid in equilibrium with its saturated vapour. C_{sat} is related to Cp by[134]

$$C_{sat} - Cp = \left(\frac{\partial P}{\partial T} \right)_{sat} \left[\left(\frac{\partial H}{\partial P} \right)_T - V \right], \qquad (20)$$

and to Cv by[134]

$$Cp - Cv = \frac{\beta^2 VT}{\chi_T} , \qquad (21)$$

where V is the molar volume, β is the coefficient of cubic expansion and χ_T is the isothermal compressibility. For most solids, especially below room temperature, the differences between C_{sat}, Cp and Cv are negligible![134] Here, the three quantities will be assumed to be identical.)

At very low temperatures, the heat capacity becomes that of an elastic continuum, and is a universal function of T/θ^C such that the Debye - T^3 law holds[135], i.e.

$$C_v = \frac{12\ Nk\ \pi^4}{5} \left(\frac{T}{\theta^C} \right)^3 , \qquad (22)$$

where θ^C is the Debye characteristic temperature, as derived from the heat capacity. (The entropy and elastic constants respectively are universal functions of T/θ^S and T/θ^{el}.) Thus, for $T < \theta^C/25$, the heat capacity expansion can often be truncated to

$$C_v = a\ T^3 + b\ T^5 , \qquad (23)$$

and, for $T < \theta^C/100$, to

$$C_V = a\,T^3$$

$$= \frac{12\,Nk\,\pi^4}{5}\left(\frac{T}{\theta^C_o}\right)^3 \quad , \qquad (24)$$

where the subscript on θ^C_o is used to denote the value of θ^C in the limit of $T \to 0K$.

A plot of C_V/RT^3 against T^2 for experimental data should be a gentle curve, and a value of θ^C_o can be obtained from the intercept on the axis at $T^2 = 0$. This, in turn, can be used to approximate the lattice contributions to the low temperature heat capacity and entropy at finite temperatures. An early estimate[136] of θ^C_o for methane, derived from CD_4 data, gave a value of $\sim$ 130K; this was, however, rather uncertain due to the large contribution of the CHD_3 impurity to the heat capacity in the low temperature region. From a plot of C_V/RT^3 against T^2 (see Figure 23), the present results for CD_4 give

$$\theta^C_o\,(CD_4) = 109 \pm 2K \quad . \qquad (25)$$

The effective characteristic temperature for the other deuterated methanes can be estimated easily from the ratio of the masses:[134]

$$\frac{\theta_1}{\theta_2} = \left(\frac{M_2}{M_1}\right)^{\frac{1}{2}} \qquad (26)$$

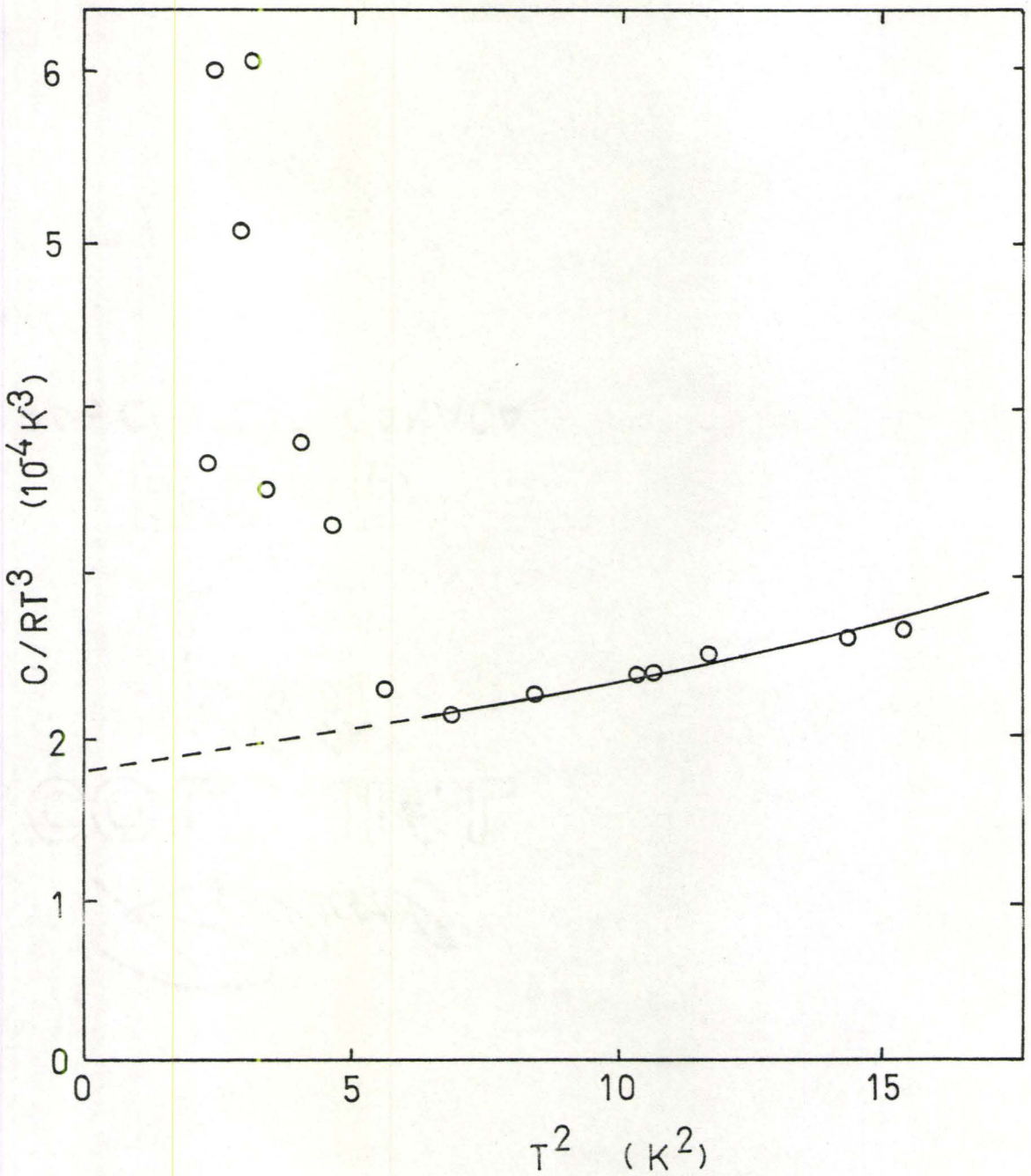

Figure 23: Cp/RT^3 vs T^2 for CD_4.

Actually, since the lattice contributions to the heat capacities of the partially deuterated methanes are so small (< 1% of the total for T < 2.0K), it is hardly worthwhile to make the small mass correction.

It should be noted that in Figure 23 the heat capacity shows significant deviations from the form of eqn (23) for $T^2 < 6K^2$. These turn out to be caused by the high temperature tail of a Schottky anomaly which makes an appreciable contribution to the heat capacity, as will be discussed later in this chapter.

2. The Entropy as a Function of Temperature for the Partially Deuterated Methanes

The absolute value of the entropy of a substance in state A can be calculated if S_B (i.e. the entropy in state B) is known, and sufficient thermal data are available to compute ΔS for the transformation from state A to state B.

For the gas, including nuclear spin, the entropy at a pressure P and temperature T may be computed from

$$S(P,T) = S_t + S_r + S_v + R \ln \Pi\rho \quad , \qquad (27)$$

where S_t, S_r and S_v are the usual statistical thermodynamic contributions for translation, rotation and vibration, and ρ is the nuclear spin weight (= 2 for hydrogen and = 3 for deuterium).[137] The required data are available[74] and yield the values of S(P,T) for the deuterated methanes that are given in Table XIV.

Table XIV

Derived Entropies for the Partially Deuterated Methanes

	S/R (T,P)	S^{8}_{o}/R	$S^{0.15}_{o}/R$
CH_3D	24.73	4.60	2.63
	(90.41K,84.50 torr)	±0.05	±0.10
CH_2D_2	25.91	5.36	3.75
	(90.17K,82.00 torr)	±0.05	±0.10
CHD_3	26.24	5.37	4.23
	(89.96K,82.20 torr)	±0.05	±0.10
CD_4	24.95	4.37	—
	(97.82K,208.8 torr)	±0.05	

The entropy of the solid methanes at some lower temperature can now be estimated by subtracting from (27) entropy changes due to cooling, condensation, solidification, etc., for which appropriate data are available here and elsewhere[38,74,76]; the low-temperature entropies of CH_2D_2 and of CHD_3 are shown respectively in Figures 24 and 25.

In order to make deductions about ground state degeneracies, it is useful to estimate the residual entropy at T = 0K by extrapolation from two regions. The first extrapolated entropy, S_o^8, is derived from the calorimetric data[38,74] for $T \geq 8K$; the contribution from the Schottky anomaly is neglected and the heat capacity for T < 8K is assumed to obey the T^3 dependence found for CD_4 in Section IV.1. An alternate extrapolated entropy, $S_o^{0.15}$, is derived from the calorimetric data down to the lowest temperature ($T \sim 0.15K$) reached in the present experiments; the data are extrapolated smoothly to T = 0K below that temperature. The values of S_o^8 and $S_o^{0.15}$ are given in Table XIV for CH_3D, CH_2D_2 and CHD_3. The earlier results[79,80,81] obtained for CH_3D are included here because they are central to the discussion of models for phase III, as will be shown later. $S_o^{0.15}$ cannot be estimated with any certainty for CD_4 from the present measurements. (Of course, if $S_o^{0.15}$ was estimated for CD_4 with the exclusion of the contribution due to the low temperature Schottky anomaly, then it would be identical to S_o^8.)

As will be seen shortly, the extrapolated values of

Figure 24: The Entropy of CH_2D_2, Including the Contribution of Nuclear Spins, as a Function of Temperature.

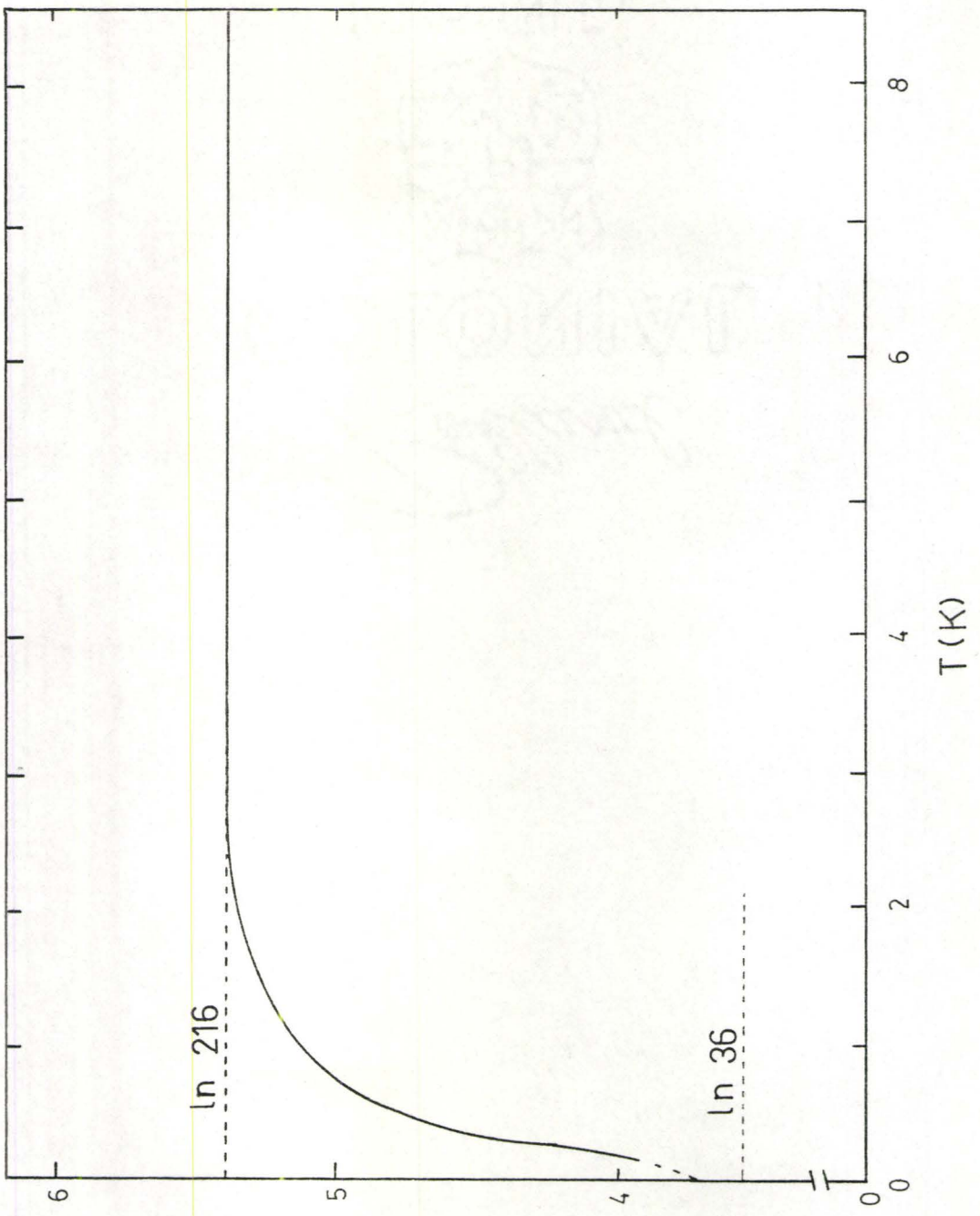
ln 216
ln 36
S/R
T(K)
0
2
4
6
8
4
5
6

Figure 25: The Entropy of CHD_3, Including the Contribution of Nuclear Spins, as a Function of Temperature.

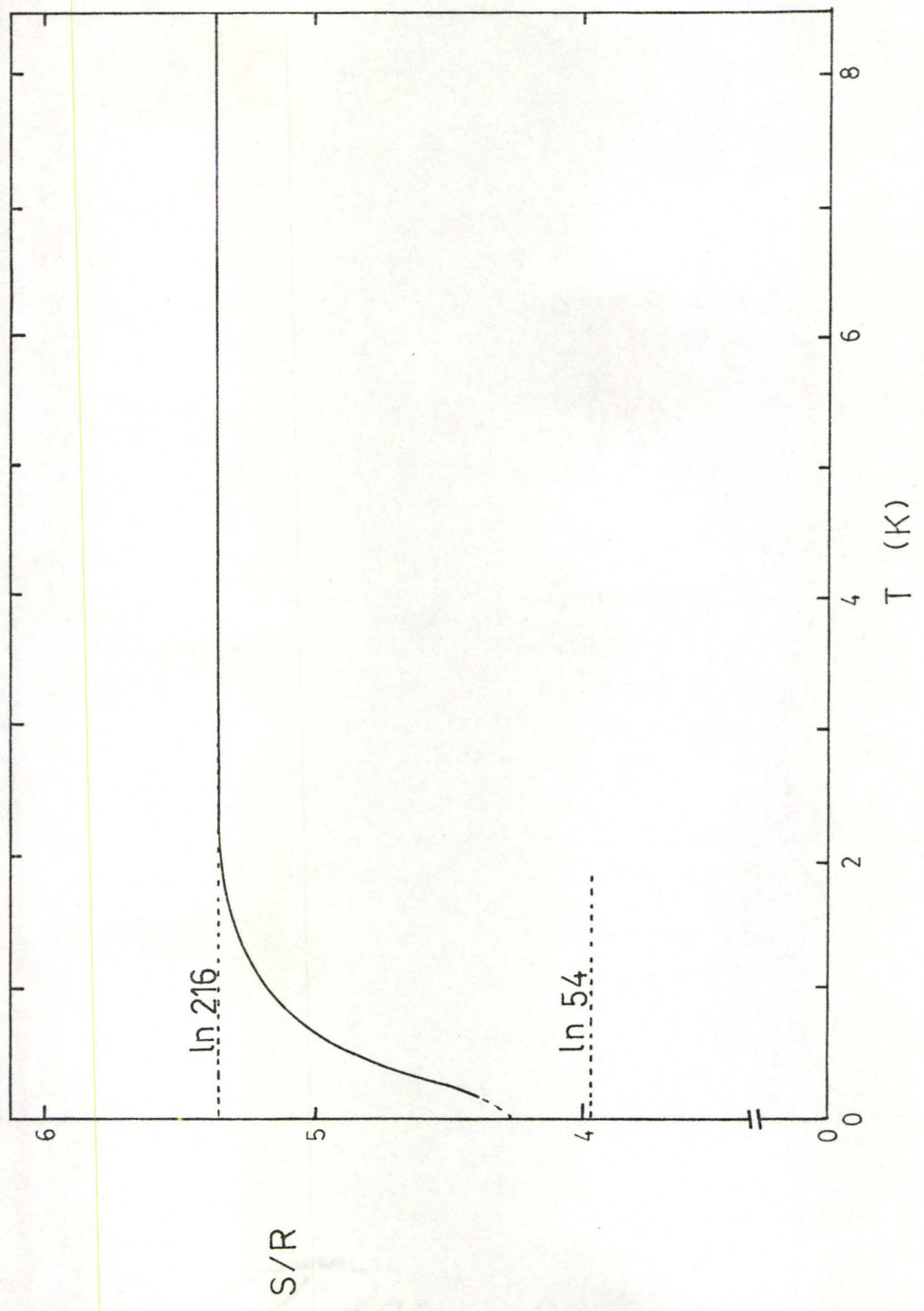
S/R
6
5
4
0
2
4
6
8
T (K)
ln 216
ln 54

S_o^8 give information about the total numbers of populated states in the low-lying tunneling levels of the deuterated methanes; under the assumption that the heat capacity goes smoothly to zero from T = 0.15K to T = 0K, $S_o^{0.15}$ gives clear-cut information about the degeneracies of the energy levels of the methane molecules in their ground states. A proper model of phase III must, of course, account for the observed values of S_o^8 and $S_o^{0.15}$, as well as the heat capacity as a function of temperature.

3. The Energy Levels of the Deuterated Methanes in Hindering Potential Fields

In Chapter I, the variation of the CH_4 energy levels under the influence of a tetrahedral hindering potential is shown in Figure 6. The energy level arrays of the deuterated methanes are similarly affected under the influence of a hindering potential; the energy levels for CH_3D[67,74,76,77], CH_2D_2[67,74,76,77,138], CHD_3[67,74,76,77] and CD_4[67,77] subjected to fields of different symmetry are given in Figures 26-29, as derived from group theory.

The values of S_o^8 given in the previous section can be easily understood in terms of the energy level schemes presented in Figure 26-29. If the tunneling states (i.e. those states arising from the influence of a hindering potential) are fully populated at T = 8K, then

Figure 26: The Energy Levels of CH_3D in Different Molecular Fields.

Here, J is the rotational quantum number, A and E are the designations of the two nuclear spin symmetry species, and the numbers shown on the states are total degeneracies; (a) corresponds to the free rotor, and (b), (c) and (d) respectively correspond to tetrahedral, trigonal and assymmetric molecular fields. The energy level spacings are not to scale.

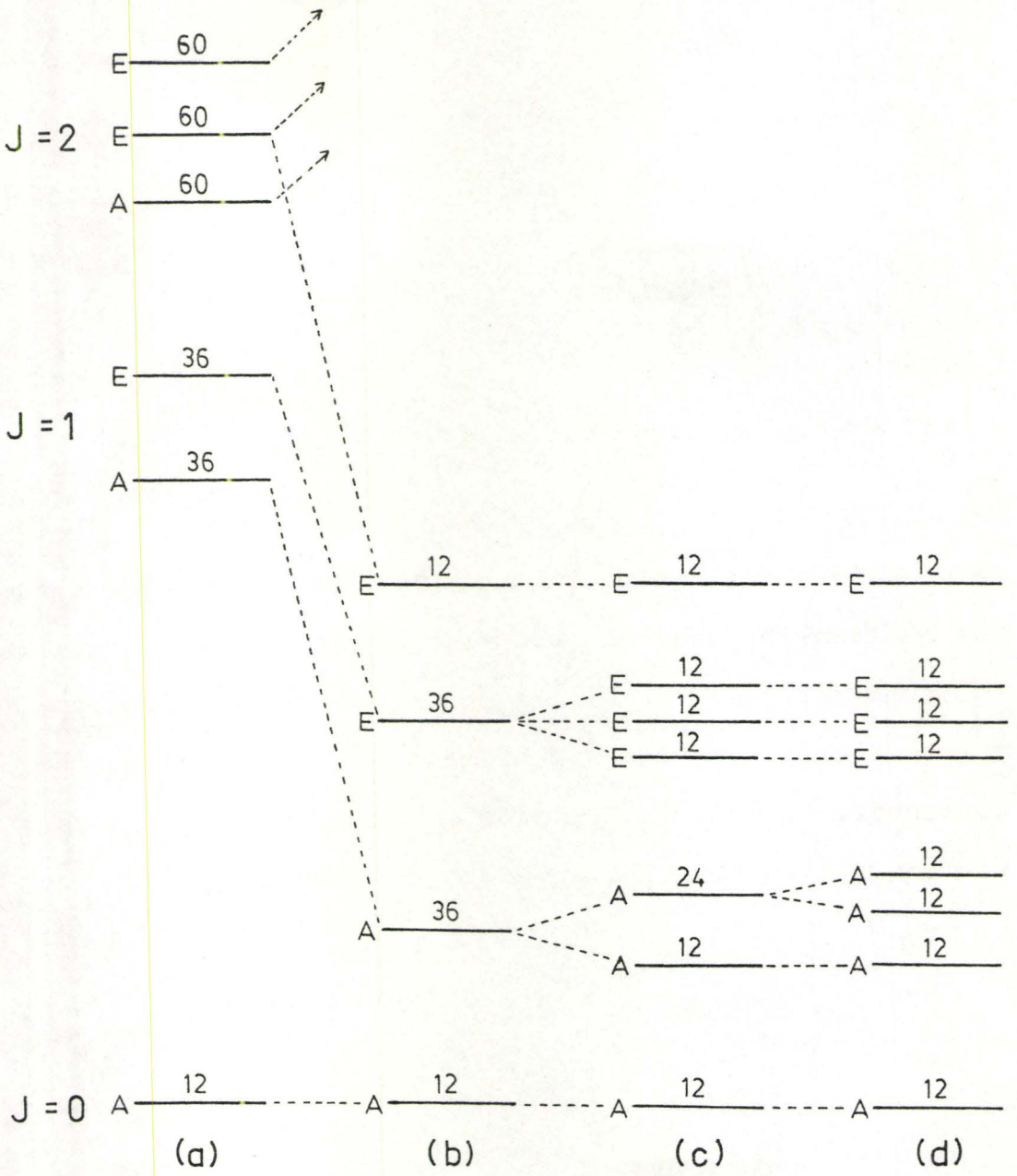
J = 2
J = 1
J = 0
E
A
60
36
12
24
(a)
(b)
(c)
(d)

Figure 27: The Energy Levels of CH_2D_2 in Different Molecular Fields.

Here, J is the rotational quantum number, A and B are the designations of the two nuclear spin symmetry species, and the numbers shown on the states are total degeneracies; (a) corresponds to the free rotor, and (b) and (c) respectively correspond to molecular fields of tetrahedral and less than tetrahedral symmetry. The energy level spacings are not to scale.

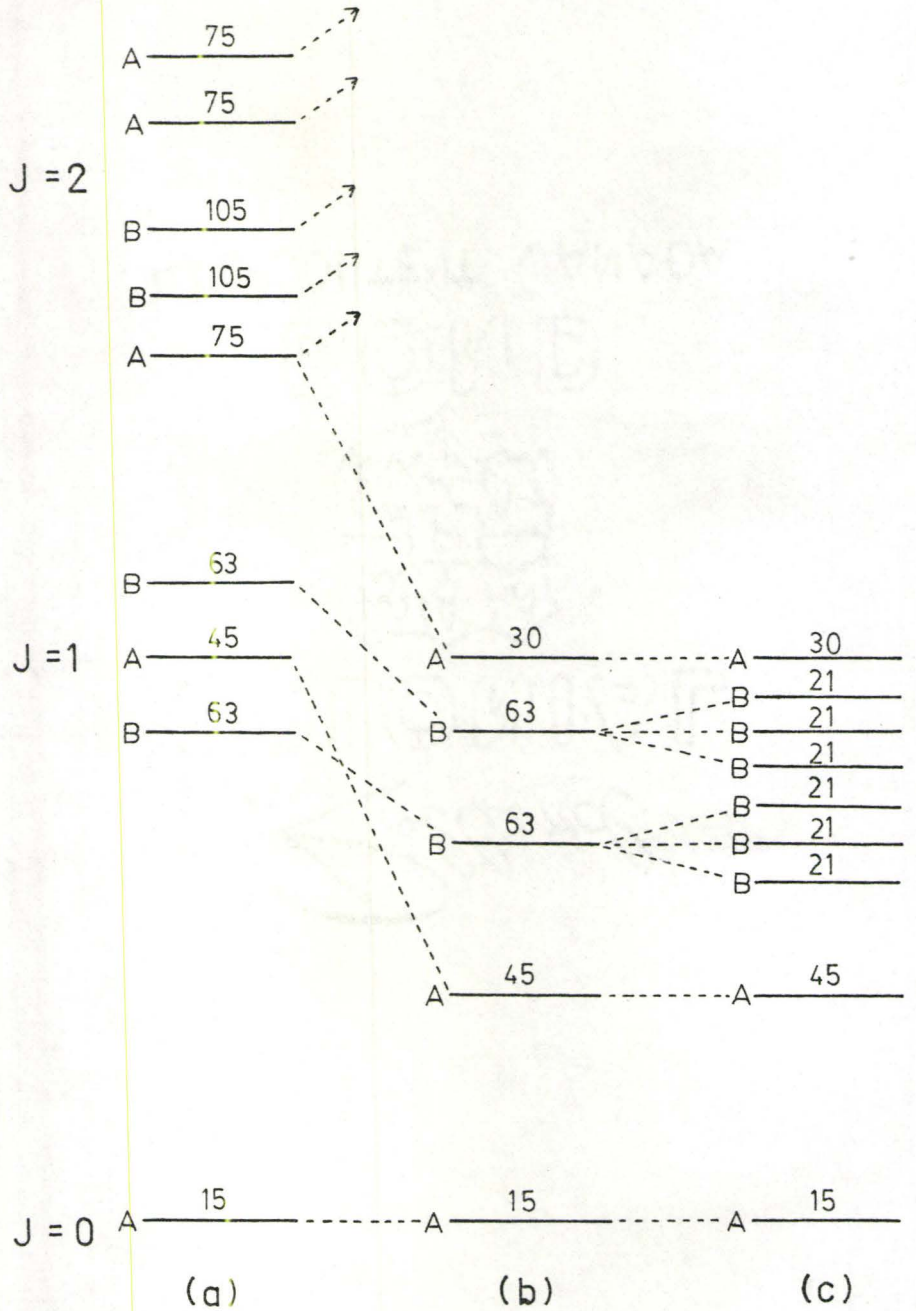
J = 2
J = 1
J = 0
A 75
A 75
B 105
B 105
A 75
B 63
A 45
B 63
A 30
B 63
B 63
A 45
A 30
B 21
B 21
B 21
B 21
B 21
B 21
A 45
A 15
A 15
A 15
(a)
(b)
(c)

Figure 28: The Energy Levels of CHD_3 in Different Molecular Fields.

Here, J is the rotational quantum number, A and E are the designations of the two nuclear spin symmetry species, and the numbers shown on the states are the total degeneracies; (a) corresponds to the free rotor, and (b) and (c) respectively correspond to molecular fields of tetrahedral and less than tetrahedral symmetry. The energy level spacings are not to scale.

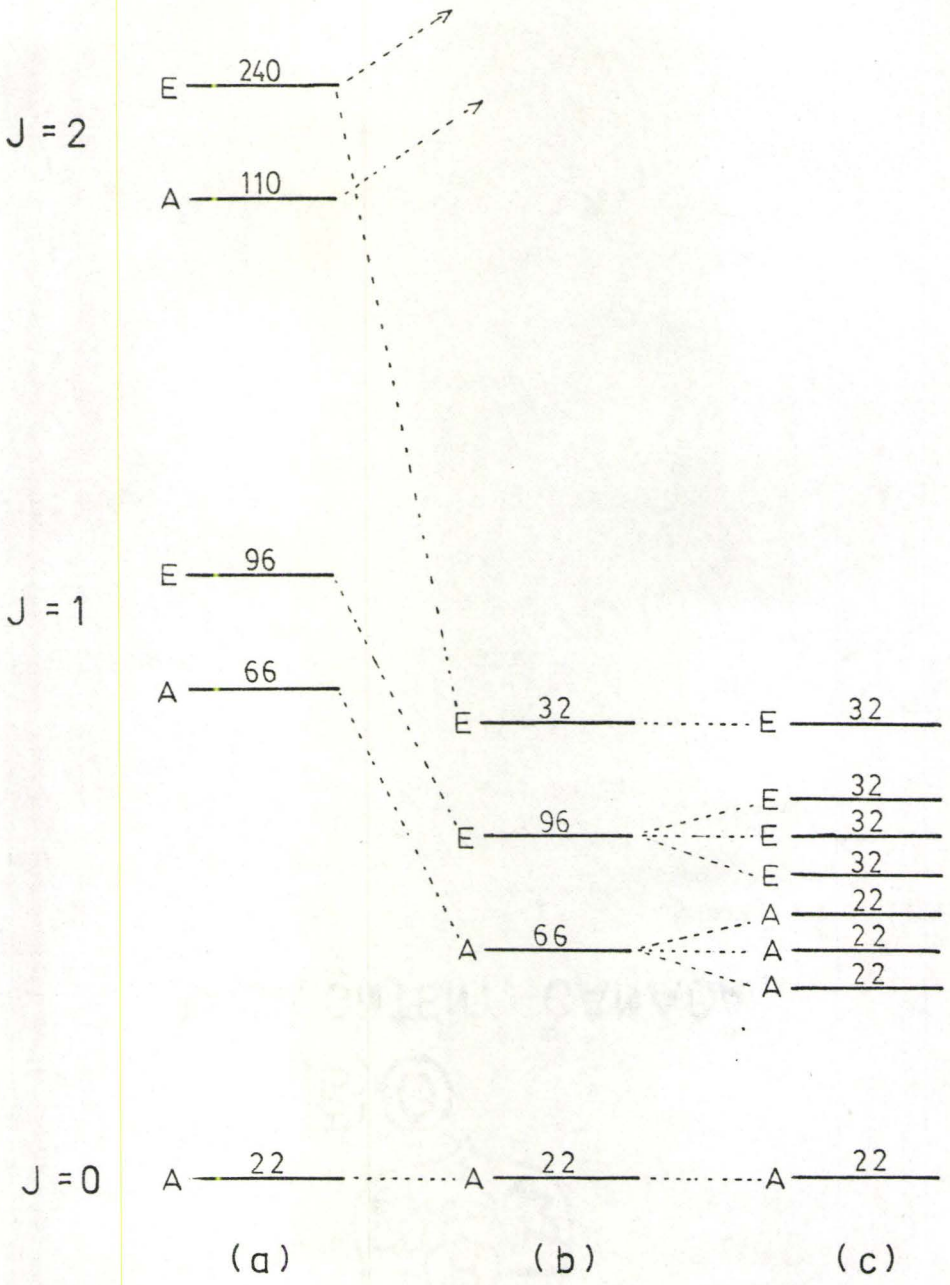
J = 2
E 240
A 110
J = 1
E 96
A 66
E 32
E 96
A 66
E 32
E 32
E 32
E 32
A 22
A 22
A 22
J = 0
A 22
A 22
A 22
(a)
(b)
(c)

Figure 29: The Energy Levels of CD_4 in Different Molecular Fields.

Here, J is the rotational quantum number, A, E and T are the designations of the three nuclear spin symmetry species and the numbers shown on the states are the total degeneracies. (a) corresponds to the free rotor, and (b) and (c) respectively correspond to molecular fields of tetrahedral and less than tetrahedral symmetry. The energy level spacings are not to scale.

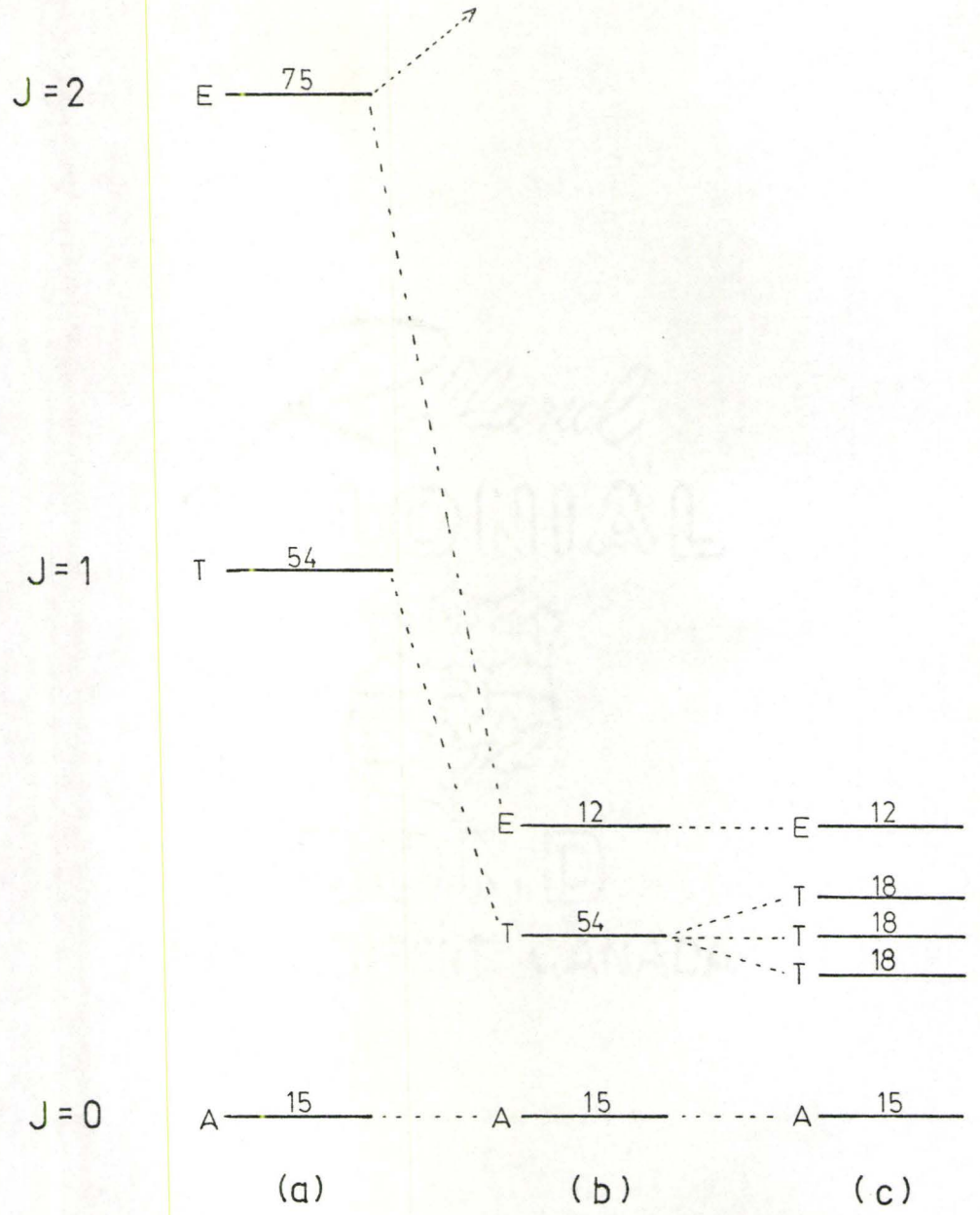
J = 2
E
75
J = 1
T
54
E
12
E
12
T
54
T
18
T
18
T
18
J = 0
A
15
A
15
A
15
(a)
(b)
(c)

$$\frac{S^8_o}{R} = \sum_i x_i \ln n_i - \sum_i x_i \ln x_i \quad , \tag{28}$$

where the sum is over the nuclear spin symmetry species, i, and n_i and x_i are respectively the total number of populated states corresponding to spin species i, and the high temperature mole fraction of the spin species. (The second term in equation (28) is the entropy of mixing of the spin symmetry species.) For example, referring to Figure 26,

$$\begin{aligned} \frac{S^8_o}{R}(CH_3D) &= \frac{48}{96} \ln 48 + \frac{48}{96} \ln 48 \\ &\quad - \frac{48}{96} \ln \frac{48}{96} - \frac{48}{96} \ln \frac{48}{96} \\ &= \ln 96 \\ &= 4.564. \end{aligned} \tag{29}$$

This result is clearly in complete agreement with the classical (high temperature) result:

$$\begin{aligned} \frac{S^8_o}{R}(CH_3D) &= \ln 4 + \ln \Pi\rho \\ &= \ln 4 + \ln (2^3 \times 3) \\ &= \ln 96 \end{aligned} \tag{30}$$

and with the experiment:[79]

$$\frac{S^8_o}{R}(CH_3D, \text{expt'l}) = 4.60 \pm 0.05. \tag{31}$$

In Table XV, values of S_o^8 for the deuterated methanes derived from experiment are compared with those calculated from the energy level diagrams given in Figures 26-29.

The experimental values of $S_o^{0\cdot15}$ are not so easily interpreted. That either classical ordering of the C-H and C-D bonds is incomplete, or nuclear spin species conversion is incomplete, or both, can be seen for all the partially deuterated methanes. In Table XVI, the values of the residual entropy, S_o, to be associated with complete ordering, and with both complete ordering and conversion, are given for each of the partially deuterated methanes. (The residual entropy limits are shown graphically for CH_2D_2 and CHD_3 in Figures 24 and 25.) The observed values of $S_o^{0\cdot15}$ clearly show that one or both of these processes must be incomplete.

4. Nuclear Spin Symmetry Species Conversion in the Partially Deuterated Methanes

Conversion processes in CH_3D are now well-established through the long relaxation times observed[74,76,79-81] in heat capacity measurements, and through NMR[78] and neutron total cross-section[79] measurements. From measurements down to T = 0.75K, the last type of experiment indicated that conversion goes to completion or nearly to completion (i.e. the mean squared value of the nuclear spin, $\langle I(I+1)\rangle$, approaches the value of 3.75 associated[139] with the pure A spin species.) It has been suggested[79] that the conversion is facile in CH_3D

Table XV

Comparison of Calculated and Experimental Values of S_o^8

	S_o^8/R (calculated)	S_o^8/R (expt'l)
CH_3D	4.564 (= ℓn 96)	4.60±0.05
CH_2D_2	5.375 (= ℓn 216)	5.36±0.05
CHD_3	5.375 (= ℓn 216)	5.37±0.05
CD_4	4.394 (= ℓn 81)	4.37±0.05

Table XVI

Comparison of Calculated and Experimental Values of Residual Entropies

	S_o/R (ordering)	S_o/R (ordering+ conversion)	$S^{0\cdot15}/R$ (expt'l)
CH_3D	ℓn 96-ℓn 4 = 3.178	ℓn 12 = 2.485	2.63 ± 0.10
CH_2D_2	ℓn 216-ℓn 6 = 3.584	ℓn 15 = 2.708	3.75 ± 0.10
CHD_3	ℓn 216-ℓn 4 = 3.989	ℓn 22 = 3.091	4.23 ± 0.10

due to an accidental degeneracy of an A and E level, but that explanation requires fuller investigation.

The absence of thermal relaxation processes and the observation that the entropy removed through its Schottky anomaly is less than R ℓn 6, indicate that nuclear spin species conversion likely does not occur in CH_2D_2 (at least not on the time scale of the heat capacity measurements.) The agreement between the present heat capacity results and those of Colwell[76] (whose specimen contained ∿ 0.1% of O_2) indicate that conversion in CH_2D_2 cannot be catalysed by molecular O_2, as is conversion in CH_4.[61,66,68,69]

It is possible that the conversion process in CH_2D_2 has a very long lifetime, if it occurs at all. The intramolecular dipole interaction which gives rise to conversion in CH_4[140], does not couple the different spin states, and therefore cannot provide a viable mechanism in CH_2D_2.[141] The proton-deuteron interactions may couple the different spin states but, even if they did, the relaxation time would be longer than for the proton-proton interactions by roughly the square of the quotient of the proton and deuteron gyromagnetic ratios.[141] This would yield[142] a relaxation time of ∿ 10^3 days for CH_2D_2. A relaxation time of this magnitude would cause perhaps a 1% change in the heat capacity over the 2 weeks that the present sample was kept cold; it would certainly be beneath the limits of detection. Deuteron quadrupolar interactions do not produce spin conversion[143],

and deuteron dipolar interactions will be $\sim 6 \times 10^{-4}$ times that of the weak proton dipolar interactions![141] It therefore appears that conversion in CH_2D_2 is extremely slow.

The ineffectiveness of the proton-deuteron and the deuteron-deuteron interactions in causing spin species conversion also makes it seem unlikely that conversion occurs very quickly in CHD_3. It again appears, based on a comparison with Colwell's measurements[76], that conversion cannot be catalysed by the presence of O_2. Moreover, the structure in the Schottky anomaly indicates the presence of two groups of low-lying energy levels roughly in the proportion 2/3, which is close to the proportion 88/128 = 0.69 of the A and E nuclear spin symmetry species in CHD_3. The contributions of the two groups of levels to the heat capacity are maximized at temperatures which indicate that the energy gap in one set of levels is approximately twice that in the other, as one would expect from theory[76,138] for the A-A and E-E splittings. These results are taken to confirm that conversion did not occur in this methane.

5. The Structure of Phase III

In science, as in all endeavours, Ockham's razor should be invoked in modelling the observed behaviour of a system; that is to say, the model should be no more complex than is necessary to explain the facts at hand. The simplest possible model of phase III of solid methane would be one in

which all the molecules in the solid sit on equivalent sites. However, the residual entropies show that this 1-site model cannot adequately explain the experimental results. If, for example, all the molecules in phase III of solid CHD_3 are at sites corresponding to tetrahedral molecular fields, and if the high temperature proportions of A and E species are assumed, then

$$\frac{S_o}{R} = \frac{88}{216} \ln 22 + \frac{128}{216} \ln 96 - \left(\frac{88}{216} \ln \frac{88}{216} + \frac{128}{216} \ln \frac{128}{216}\right)$$

$$= 4.640 \; ; \qquad (32)$$

if the molecules are all at sites with molecular fields of less than tetrahedral symmetry, and again conversion is assumed not to occur, then

$$\frac{S_o}{R} = \frac{88}{216} \ln 22 + \frac{128}{216} \ln 32 - \left(\frac{88}{216} \ln \frac{88}{216} + \frac{128}{216} \ln \frac{128}{216}\right)$$

$$= 3.989 \; . \qquad (33)$$

Since the observed value of $S_o^{0 \cdot 15}/R$ of 4.23 ± 0.10 does not agree with either of the above results, phase III cannot be a structure which has all of the molecules on sites of the same molecular field symmetry.[144]

The next simplest model of phase III would be one

composed of two sublattices. The CH_3D data can be used, as follows, to calculate possible sublattice proportions. From Figure 26, it can be seen that the degeneracy of the lowest A state in CH_3D is invariant to the molecular field symmetry, while the degeneracy of the lowest E state is not. The residual entropy of CH_3D[79,81] indicated that, in phase III, both complete ordering and complete conversion did not occur; the degeneracies of the lowest A and E states indicate that the additional entropy must be associated with the E species. Of course, in order for the E species to contribute to the entropy at T = 0K, conversion cannot be complete in CH_3D.

There are two possible ways to associate the residual entropy with the E species for CH_3D; the sublattice on which conversion does not take place could have a molecular field of tetrahedral symmetry or one of less than tetrahedral symmetry. To be consistent with the observed residual entropy for CH_3D, these symmetries would lead, respectively, to 1/8 and 1/4 of the molecules retaining their high temperature spin species composition. These possibilities will be examined in turn, making use of the information that is known for CH_2D_2 and CHD_3.

If 1/8 of the molecules in phase III of CH_3D experience tetrahedral molecular fields and do not undergo conversion, then the remaining 7/8 of the molecules can be distinguished as having either molecular fields of tetrahedral

or less than tetrahedral symmetry. The former possibility is ruled out immediately since it is equivalent to a 1-site model for phase III. The latter possibility would give rise to

$$\frac{S_o}{R} = \frac{1}{8}\left(\frac{90}{216}\ln 15 + \frac{126}{216}\ln 63\right) + \frac{7}{8}\left(\frac{90}{216}\ln 15 + \frac{126}{216}\ln 21\right) - \frac{90}{216}\ln\frac{90}{216} - \frac{126}{216}\ln\frac{126}{216}$$

$$= 3.664 \qquad (34)$$

for CH_2D_2, and

$$\frac{S_o}{R} = \frac{1}{8}\left(\frac{88}{216}\ln 22 + \frac{128}{216}\ln 96\right) + \frac{7}{8}\left(\frac{88}{216}\ln 22 + \frac{128}{216}\ln 32\right) - \frac{88}{216}\ln\frac{88}{216} - \frac{128}{216}\ln\frac{128}{216}$$

$$= 4.070 \qquad (35)$$

for CHD_3.

Similarly, if 1/4 of the molecules in phase III of CH_3D have molecular fields of less than tetrahedral symmetry and do not undergo conversion, then the remaining 3/4 must experience molecular fields of tetrahedral symmetry in the 2-site picture. The values of S_o would then be

$$\frac{S_o}{R} = 4.064 \qquad (36)$$

for CH_2D_2, and

$$\frac{S_o}{R} = 4.477 \qquad (37)$$

for CHD_3. The fact that neither of these 2-site schemes fits the experimental values of $S_o^{0 \cdot 15}$ (Table XIV) for both CH_2D_2 and CHD_3 indicates that this concept of phase III is also too simple.

The neutron cross-section measurements indicate that it is likely that more than 3/4 of the molecules undergo conversion in phase III of CH_3D?[79] If the first of the above possibilities is considered (i.e. that 1/8 of the molecules do not convert, and these molecules are on sites with tetrahedrally symmetric molecular fields) then, to account for the observed entropy of CH_2D_2 on the basis of a 3-site model, the remaining 7/8 of the molecules must be split in a 2:5 ratio between molecular fields of tetrahedral and less than tetrahedral symmetries. This model gives the residual entropies (S_o) in Table XVII where the model is summarized; they reproduce adequately $S_o^{0 \cdot 15}$ for CH_3D and CH_2D_2, and convincingly predict that for CHD_3.

In his earlier work on the partially deuterated methanes, Colwell[76] sought to fit experimental heat capacities with models that assumed either tetrahedral or lower than tetrahedral molecular field symmetry. At the time, it was not

Table XVII

Proposed 3-Site Model for Phase III

	Sites			S_o(calc)	$S_o^{0.15}$(expt)
	Type 1	Type 2	Type 3	R	R
Molecular Field Symmetry	tet	tet	< tet		
Mole Fraction	1/8	1/4	5/8		
Conversion:					
CH_3D	no	yes	yes	2.64	2.63±0.10
CH_2D_2	no	no	no	3.79	3.75±0.10
CHD_3	no	no	no	4.24	4.23±0.10

suspected that phase III would have such a complicated sublattice structure. It is interesting that the array deduced in the present study is very similar to a combination of two arrays which Colwell considered (See Figure 13 of Ref. 76).

Several additional points should be noted about the proposed 3-site model. For example, the sublattice proportions in this model of phase III are sensible in relation to the known sublattice structure of phase II. As mentioned previously, Maki et al.[111] have, on the basis of theory, proposed a 3-site model for phase III; the sublattice proportions of their model are also sensible, but all the molecules are supposed to feel tetrahedral molecular fields, and the residual entropy, therefore, does not agree with that estimated from experiment. With the assumptions that (i) the S_4 and C_s molecules experience molecular fields of less than tetrahedral symmetry, (ii) the D_2 sites have tetrahedrally symmetric molecular fields, and (iii) conversion occurs only for the C_s and D_2 molecules of CH_3D, and not at all in CH_2D_2 and CHD_3, the model can be modified to give residual entropies that are in good agreement with the experimental results. However, this model would then require that 1/4 of the CH_3D molecules do not undergo conversion, in contradiction with the results of the neutron cross-section measurements.[79] There is, however, general agreement among the theoretical calculations,[111] optical properties,[115,116] and the present results that phase III of solid methane is composed of a

minimum of 3 sublattices.

Part B: Low-Lying Energy Levels in the Solid Methanes

The present heat capacity measurements and the 3-site model of phase III that is described in Table XVII can be used to estimate the array of tunneling levels for CHD_3. It is assumed that (i) the two types of tetrahedral sites have the same tunnel splittings, and (ii) the molecular field at the non-tetrahedral sites produces an additional splitting for the E species but not for the A species. The array of energy states is shown in Figure 30 where the total degeneracies are given. Since group theoretical arguments[76,138] indicate that the energy level splitting for the E molecules should be half that for the A molecules, the derivation of the energy states can be reduced to a two parameter problem by taking $a = c = 2b = 2e$. The heat capacity data were fitted by linear least squares and the values $a = 1.55K$ and $d = 0.29K$ were found for the two free parameters. The quality of the fit is displayed in Figure 31. It is well within experimental error throughout the entire temperature range.

In principle, the general model evolved here could be used to make estimates of the ground state manifolds of the tunneling states of CH_3D and CH_2D_2. The adoption of the ideas developed with the example of CHD_3 would undoubtedly remove the logical inconsistencies that resulted in the earlier attempts[114,127] to use a two sublattice model to derive the

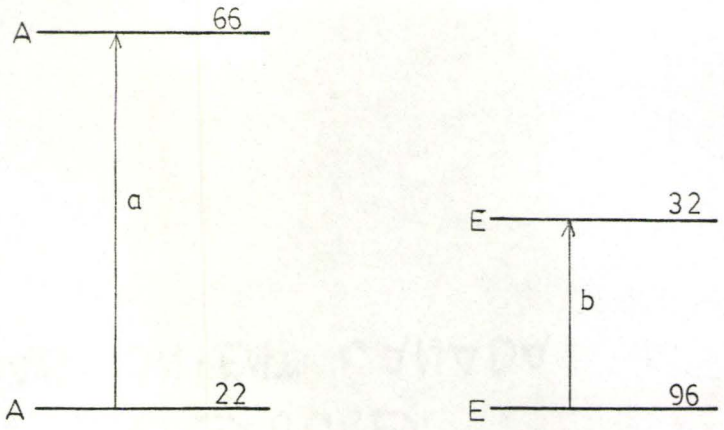

TETRAHEDRAL MOLECULAR FIELD
(mole fraction : 3/8)

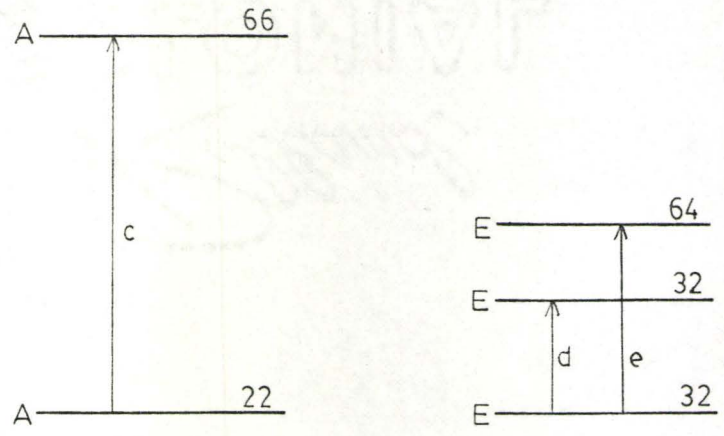

< TETRAHEDRALLY SYMMETRIC
MOLECULAR FIELD
(mole fraction : 5/8)

Figure 30: Model of the Tunneling States in CHD_3.

Figure 31: The Schottky Anomaly Contribution to the Heat Capacity of CHD_3.

The open circles are the present experiment values of the heat capacity with the lattice contribution (as determined from equations (22) and (25)) removed, and the solid line is the heat capacity calculated from the energy level scheme of Figure 30 with a = c = 2b = 2e = 1.55K, and d = 0.29K.

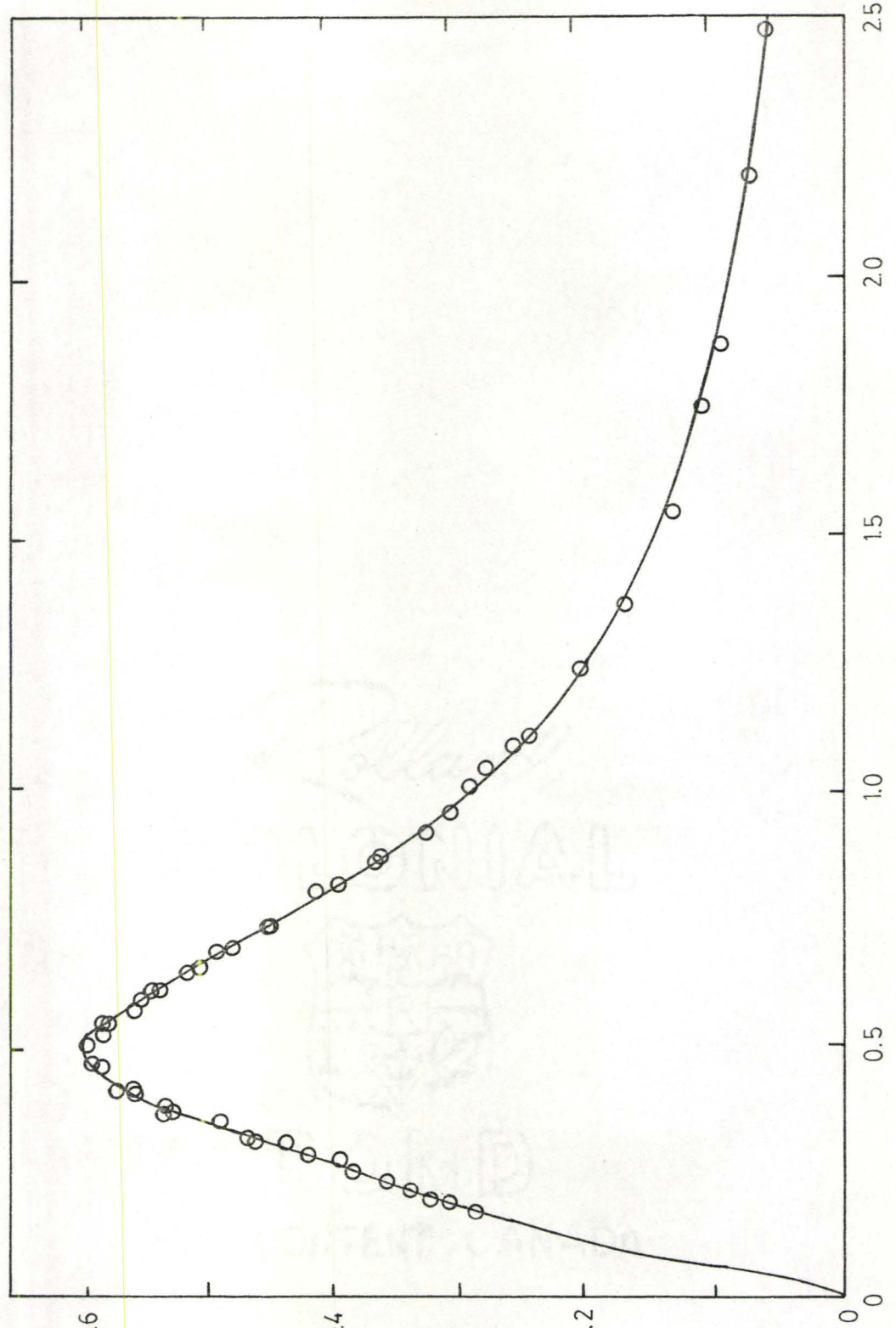
ΔCp/R
0.6
0.4
0.2
0
0.5
1.0
1.5
2.0
2.5
T (K)

energies of the tunneling states. However, the large number of possible levels, in combination with the absence of simplifying relationships between the energy level splittings for the different species and the lack of structure in the Schottky anomalies of CH_2D_2 and CH_3D, would make this an uninviting problem. The uniqueness of any solution derived could not be certain.

The CH_3D and CH_2D_2 measurements can, however, give some information about the energy levels. From the shape and position of the Schottky contribution to the heat capacity, limits can be placed on the level splittings. The thermal depopulation of two energy levels, for example, will give rise to an anomalous heat capacity for which

$$\frac{T_{max}}{\delta} \sim 0.4 \qquad (38)$$

where T_{max} is the temperature at which the maximum heat capacity occurs and δ is the energy separation between the levels (in K).[145] This guide and the observed positions of the heat capacity maxima give approximate values for the major splitting in each of the deuteromethanes: δ(A-E) in $CH_3D \sim 1.3K$, δ(A-A) in $CH_2D_2 \sim 0.6K$, δ(A-A) $CHD_3 \sim 1.3K$. (The last of these has been confirmed by the fit to the heat capacity data, as described above.) The values are to be contrasted with recent theoretical estimates[146] of the tunneling levels; the predicted separations for the above-

mentioned states in CH_3D, CH_2D_2 and CHD_3 are respectively 1.1K, 0.4K and 0.11K. The calculation was based on an estimate of the molecular field strengths for the deuterated methanes relative to that in CH_4 by the same variational method[31] that was used to give the low-lying energy levels in CH_4 that are shown in Figure 6. The present experimental results, however, clearly show that the potential field strengths do not vary greatly within the partially deuterated methanes.

The increase in the CD_4 heat capacity at the lowest observed temperatures indicates that a thermal depopulation of low-lying energy levels takes place in this methane also. The depopulation could take place strictly within the split T levels, or through spin species conversion from the E and T levels to the ground state A level (see Fig. 29.) It appears likely that conversion is involved, since the thermal relaxation time in CD_4 increases in the same region as the heat capacity increases; in addition, the T splitting should be very small relative to the E-T and A-T splittings (which are already predicted to be considerably contracted relative to the splittings of the hydrogenated methanes![146])

From the present measurements, an upper limit can be placed on the tunnel splittings in CD_4 as follows. Hüller estimated[146] that the E and T levels in phase III of CD_4 are nearly degenerate, and therefore the low-lying levels can be modelled as a 2-level system. The heat capacity due to the Schottky anomaly will be given by[145]

$$\frac{C}{R} = \left(\frac{\delta}{T}\right)^2 \frac{g_0}{g_1} \frac{\exp(\delta/T)}{(1+g_0/g_1)\exp(\delta/T))^2} \qquad (39)$$

where g_0 and g_1 are respectively the degeneracies of the lower and upper states (= 15 and 66 here), and δ is the energy separation between the two states. At high temperatures, eqn. (39) can be expanded as an infinite power series in T^{-1}; the Schottky contribution to the heat capacity can be approximated[145] by the truncated expression

$$\frac{C}{R} = \frac{g_0 g_1}{(g_0+g_1)^2} \left(\frac{\delta}{T}\right)^2 + b\, T^{-3} \quad , \qquad (40)$$

that is,

$$\frac{CT^2}{R} = \frac{g_0 g_1}{(g_0+g_1)^2} \delta^2 + b\, T^{-1} \quad . \qquad (41)$$

Therefore, a plot of $T^2\Delta C/R$ (where $\Delta C = C_{\text{expt'l}} - C_{\text{lattice}} - C_{CHD_3}$) against T^{-1} would give a linear relationship in the region of the high temperature tail of a Schottky anomaly, as shown in Figure 32. The intercept, extrapolated from the region $0.15K \leq T \leq 0.50K$, gives a value of $\delta = 0.042 \pm 0.010K$ assuming 0.2 mole % CHD_3. In good agreement with the present results, recent neut inelastic scattering measurements at T = 4.2K showed[147] three or possibly four energy level splittings in the region $\delta < 0.046K$. The search for tunnel splittings at higher energies has yet to be carried out, but the present measurements can clearly put an upper bound of $\sim 0.06K$ on the splittings. The calorimetric and neutron scattering results also agree well

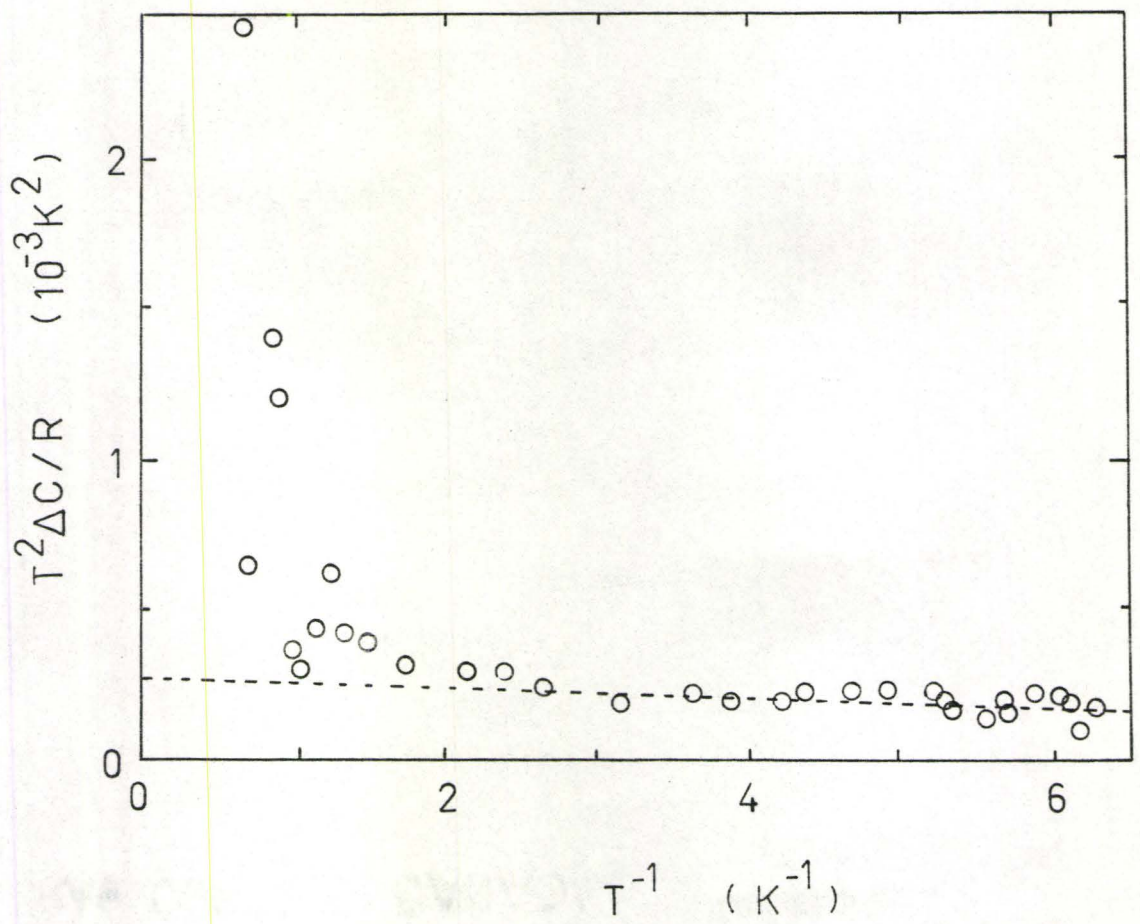

Figure 32: The Schottky Tail in CD_4.

($\Delta C = C_{expt'l} - C_{lattice} - C_{CHD_3}$)

with the splittings that have been theoretically predicted[146] for CD_4 (δ(A-E) $\sim$ 0.04K, δ(A-T) $\sim$ 0.03K).

Part C: Possible Future Investigations

The experimental investigations described in this thesis, in combination with concurrent experimental and theoretical studies, especially the theoretical examinations of Professor T. Yamamoto and his colleagues, yield considerable basic information about the complex behaviour of solid isotopic methanes. However, there is still much to be learned about the following: the crystal structure of phase III; the low-lying tunneling states; mechanisms of conversion between nuclear spin symmetry species; a possible phase IV; mechanisms of phase transitions and orientational ordering; lower dimensional systems and surface phases; intermolecular potentials. These topics will be discussed briefly in turn.

An earlier diffraction study[54] of solid CD_4 could not uniquely establish the structure of phase III since, below the phase II $\rightarrow$ III transition, the tetragonal c-axis was randomly oriented along each of the cubic axes of phase II. It is possible[147] that a neutron diffraction study of a thin crystal of CD_4 could cause growth of the c-axis in a preferred direction, and thereby allow the direct structure determination of phase III. Such a study, if successful, would certainly establish the site symmetries and sublattice proportions in the phase. It would also provide a test for the theoretically

proposed[111] structure of phase III.

Although it would not give direct information about the phase III structure, inelastic neutron scattering experiments would give important information about the low-lying tunneling levels in the partially deuterated methanes. The method would yield the energy splittings of the states involved and, in conjunction with the present heat capacity results which contain information about both the splittings and the degeneracies of the states, such experiments would likely lead to unequivocable tunneling energy level schemes for the partially deuterated methanes. A direct measurement of the tunnel splittings in CHD_3, where the energy levels are quite well defined from the heat capacity, would likely be a useful guide to the interpretation of the CH_2D_2 and CH_3D results.

In order to understand more fully the properties of phase III, detailed investigations of the kinetics and mechanisms of nuclear spin species conversion are also warranted. Although it has been suggested that conversion in CH_3D is facilitated by an accidental degeneracy of an A and an E level[79], no certain causes for the differences in conversion rates in the deuterated methanes have been deduced. A calculation for the heavier methanes, along the lines of the Nijman and Berlinsky[140] calculation for conversion in CH_4 may provide useful information.

Phase III now appears to be a complex multi-sublattice structure that is not classically ordered. It therefore seems

likely that a fully ordered phase exists in a lower temperature or higher pressure domain. The possible existence of a phase IV needs to be carefully investigated; NMR and optical measurements at elevated pressures might probe (and characterize) such a phase.

Thus far, the main subject of this thesis has been the extrapolation of the thermal properties of solid methane to T = 0K; very little emphasis has been placed on the processes which take place near the ordering phase transitions. Further examination of the transition regions, for example through the spin-lattice and spin-spin relaxation times, in search of such processes as critical slowing down, might yield information concerning the mechanisms of the phase transitions and orientational ordering.

Bulk solids are not the only systems to show fascinating orientational order/disorder phenomena, however. Lately, there has been a great deal of interest in the orientational ordering of molecular solids that are adsorbed on well-defined solid substrates. These systems are important not only because they show intriguing properties of their own, but also because, in the limit of thick coverage, they exhibit the properties of the bulk solid. Certainly, further neutron scattering such as that carried out by White[148] for partial coverage of CH_4 on grafoil, in conjunction with corresponding thermodynamic measurements and theoretical calculations will bring an understanding of the ordering processes in the simpler 2-dimensional system.

The results of any theoretical calculations of the properties of either a 2-dimensional or 3-dimensional lattice of solid methane will depend on the intermolecular potential that is chosen for the model, since the interaction is very finely-tuned. Dynamical calculations of the sort started by Klein[149-50] and O'Shea[151] certainly would test the limits of the presently available methane intermolecular potentials, and may also add to the understanding of the mechanism by which orientational ordering takes place. In addition, such a calculation might yield information about the stability of a possible phase IV.

Finally, since much is now known about the processes which take place in solid methane, this information should be applied, where possible, to understand other molecular solids, and other areas of physical chemistry. In the next chapter, the known properties of CH_4 and CD_4 will be used to interpret the thermoluminescent characteristics of these substances.

Chapter V

AN EXPERIMENTAL STUDY OF METHANE THERMOLUMINESCENCE NEAR THE SOLID-SOLID PHASE TRANSITIONS

Part A : Introduction

The luminescence of inorganic solids during and after exposure to ionizing radiation has long been understood[152,153], but the same is not true for the corresponding luminescence, and especially the deferred luminescence, of organic compounds[154]. (The term "deferred luminescence" is used here to denote that which is seen following ionizing irradiation, under the influence of heat, light or an electric field.) In the case of inorganic solids, the deferred luminescence can be treated in terms of band theory; for organic solids, terms such as ions and trapped electrons seem to be more appropriate.

The first evidence for deferred luminescence in an organic solid was the observation of Lewis and Bigeleisen[155] that lithium carbazole and lithium diphenylamine had a very long lifetime in the "phosphorescent state" at a temperature of 90K. This was followed by the observations of Debye and Edwards[156,157] that such long-lived phosphorescence was also present in proteins, aromatic amino acids, aniline and phenol, and that the duration of the luminescence was a

function of temperature. These authors proposed the following model for the deferred luminescence: during irradiation, ionization takes place, and the ejected electrons are trapped; their eventual return to the parent cations takes place by a diffusive mechanism; the recombination results in luminescence. This model is still used to describe thermoluminescence processes in molecular solids.

The radiation which causes ionization and thereby gives rise to trapped electrons can be X-rays, γ-rays, electrons or ultraviolet light, and the detrapping agent can be thermal energy, light or an electric field. The deferred luminescence is known as radiothermoluminescence (RTL), photothermoluminescence(PTL), radiophotoluminescence (RPL), radioelectroluminescence (REL), etc., according to the ionizing radiation (radio = X-rays, γ-rays, electrons, photo = UV light) and the detrapping energy source (thermo = thermal energy, photo = light and electro = electric field). The present work is concerned with radiothermoluminescence and photothermoluminescence.

It is instructive to examine more closely the processes which give rise to deferred luminescence. In PTL, photoionization of a species, A, in the solid takes place such that[158]

$$A + h\nu \rightarrow A^* \rightarrow {}^3A \qquad [1]$$

$${}^3A + h\nu \rightarrow A^{**} \rightarrow A^+ + e^-, \qquad [2]$$

and the electron will be trapped in the solid in such a way as to lower the overall energy. In thermoluminescence, the e^- may be detrapped by thermal energy,

$$e^- + kT \rightarrow e^- \text{ (mobile)} \qquad [3]$$

$$e^- \text{ (mobile)} + A^+ \rightarrow A^{**} \rightarrow A + h\nu_f + h\nu_p \qquad [4]$$

and the result will be recombination of the mobilized electron with the cation, A^+, and fluorescence or phosphorescence that is characteristic of species A. Due to the high ionization energy of pure alkanes, a small amount of aromatic impurity must be added to see thermoluminescence in these matrices; the aromatic compound then serves as species A in the above sequence.

After the irradiation takes place, there is some immediate luminescence before the thermal energy is increased; this is the so-called isothermal luminescence, or ITL. However, the main interest here is in the luminescence as a function of temperature (i.e. the thermoluminescence "glow curve".) There are two distinct processes which can give rise to features of the glow curve, and these will be discussed in turn.

The Randall Wilkins model[159] predicts the shape of glow peaks which are the result of the thermally activated detrapping of electrons. The model assumes that an electron which has been released from a trap has a negligible

probability of being retrapped, and spends a very short time in the mobile state before it recombines with a cation. A kinetic analysis of the model allows the determination of the activation energy and the kinetics of recombination; it also demonstrates that the peaks in the glow curve which correspond to the recombination of thermally activated electrons have a width at half peak height which is 10-20% of the peak temperature. As the thermal energy that is available to the trapped electrons is increased, electrons will be mobilized at temperatures which are characteristic of their trapping energies. A typical activation energy for the release of electrons trapped in an organic solid is $\sim$ 0.1 eV.[154]

Sometimes, peaks which are much sharper than the Randall Wilkins peaks are observed in the glow curves, and it is safe to say that they originate from another process. In this case, the trapped electrons are released when the barrier to recombination is removed by a sudden change in the molecular motion in the matrix, such as that at a solid-solid phase transition, or at the melting point of the solid. Although there have been a few careful studies (one example is the simultaneous observations of RTL and X-ray diffraction of CH_3OH/H_2O mixtures in the region of their glassy phase transitions[160,161]), there is still much uncertainty and contradiction concerning thermoluminescence at phase transitions. As examples, consider the following. There is not always a

one to one correspondence between known phase transitions and the existence of sharp peaks in the glow curve. In cases where a correlation has been observed, peaks have variously been reported at temperatures below[154,160,161], at[154,162], and above[154,162] the temperature of the phase transitions; peaks have also been reported both at the start and end of a phase transition![163] Although a great deal of work has been carried out to determine the effects of sample annealing on the thermoluminescence glow curves[154,160-163], little is known about the effects of the sample size and sample preparation techniques![162] In addition, the effect of added and accidental impurities on the shape of the glow curve is usually assumed to be negligible![154] There has been some general discussion of the processes which allow electrons to be released from traps at solid-solid phase transitions[154] but the exact mechanism is not understood.

The thermoluminescence of solid methane is of interest both because of the polymorphism of the solid and because of the plethora of information concerning the solid phases. The thermoluminescence of CH_4 with 0.1% toluene, after bombardment with 1 MeV electrons, has been reported briefly[162]; the actual glow curve was not shown, but a peak that is 3.2K wide at half height and centred at T = 22.8K is described. (This is to be compared with the phase II→I transition at T = 20.5K.) In this temperature region, however, the heating rate was $\sim$ 20K min^{-1}, which is much too fast to measure thermoluminescence

with any certainty. The experiments which will be described in this chapter report a systematic study of the thermoluminescence of CH_4 and CD_4 with toluene and benzene as added impurities.

Part B: Experimental

1. Sample Purity and Preparation

The CH_4 (Matheson Gas, Whitby, Ontario) that was used in the present study was ultra-high purity grade, with a stated chemical purity of $\geq$ 99.97%. The principal impurities were stated to be N_2 and C_2H_6, and the gas was used without further purification.

On the other hand, the CD_4 (Merck, Sharp and Dohme, Montreal) was only > 99% chemically pure, and ~97% isotopically pure. The gas was not isotopically purified since the phase transition temperatures in CD_4 do not critically depend on small amounts of CHD_3. In some experiments, the cylinder containing the CD_4 was cooled to -78°C (dry ice/acetone) while a specimen was removed. The cooling may have increased the sample purity somewhat due to condensation of trace impurities on the cylinder walls; the experiments in which the CD_4 specimens were prepared in this manner will be identified in the results section.

Reagent grade toluene was dried over anhydrous $CaCl_2$ for 48 hours, and then fractionally distilled at a temperature of 108°C; the first distillation fraction was discarded.

Similarly, reagent grade benzene was fractionally distilled at a temperature of 80°C, and then left to dry over Na metal for several weeks. Both the toluene and benzene samples were subjected to several freeze-pump-melt cycles on a high vacuum line to remove traces of dissolved gases.

The methane and the aromatic impurity, at pressures of P_1 and P_2 respectively, where $P_1 >> P_2$, were allowed to mix for a few minutes in the gas phase before the homogeneous sample was deposited onto a cold target. The samples were handled exclusively on a high vacuum line ($P < 1 \times 10^{-6}$ torr), and contained up to $\sim$ 0.5 mole % of aromatic impurity. The specimen sizes ranged from a few to a few hundred milligrams.

2. The Apparatus

The apparatus that was used for the thermoluminescence experiments will be described in three parts: the cryostat, the irradiation sources and the light detector.

(a) The Cryostat

(i) General Features

The liquid helium cryostat was built by The Oxford Instrument Co. Ltd., and was a modified MD4A model. It is shown schematically in Figure 33. Its principal cryogenic features were a main liquid helium reservoir (capacity $\sim$ 2.8ℓ), a smaller liquid helium pot beneath it (capacity $\sim$ 0.22ℓ) and a liquid nitrogen reservoir (capacity $\sim$ 3.0ℓ); each reservoir was insulated from the others and from the surroundings by a

Figure 33: The Thermoluminescence Cryostat.

a - goniometer
b - to vacuum pumps
c - vacuum insulation space
d - liquid N_2 jacket
e - main liquid He reservoir
f - electrical feedthrough
g - He flow tube to lower reservoir
h - 4.2K shield
i - 77K shield
j - outside vacuum jacket
k - coupling to electron gun
m - Speer resistance thermometer
n - sample block
p - copper-constantan thermocouple
q - to He recovery system
r - needle valve
s - heater wire
t - lower liquid He reservoir
u - quartz optical window

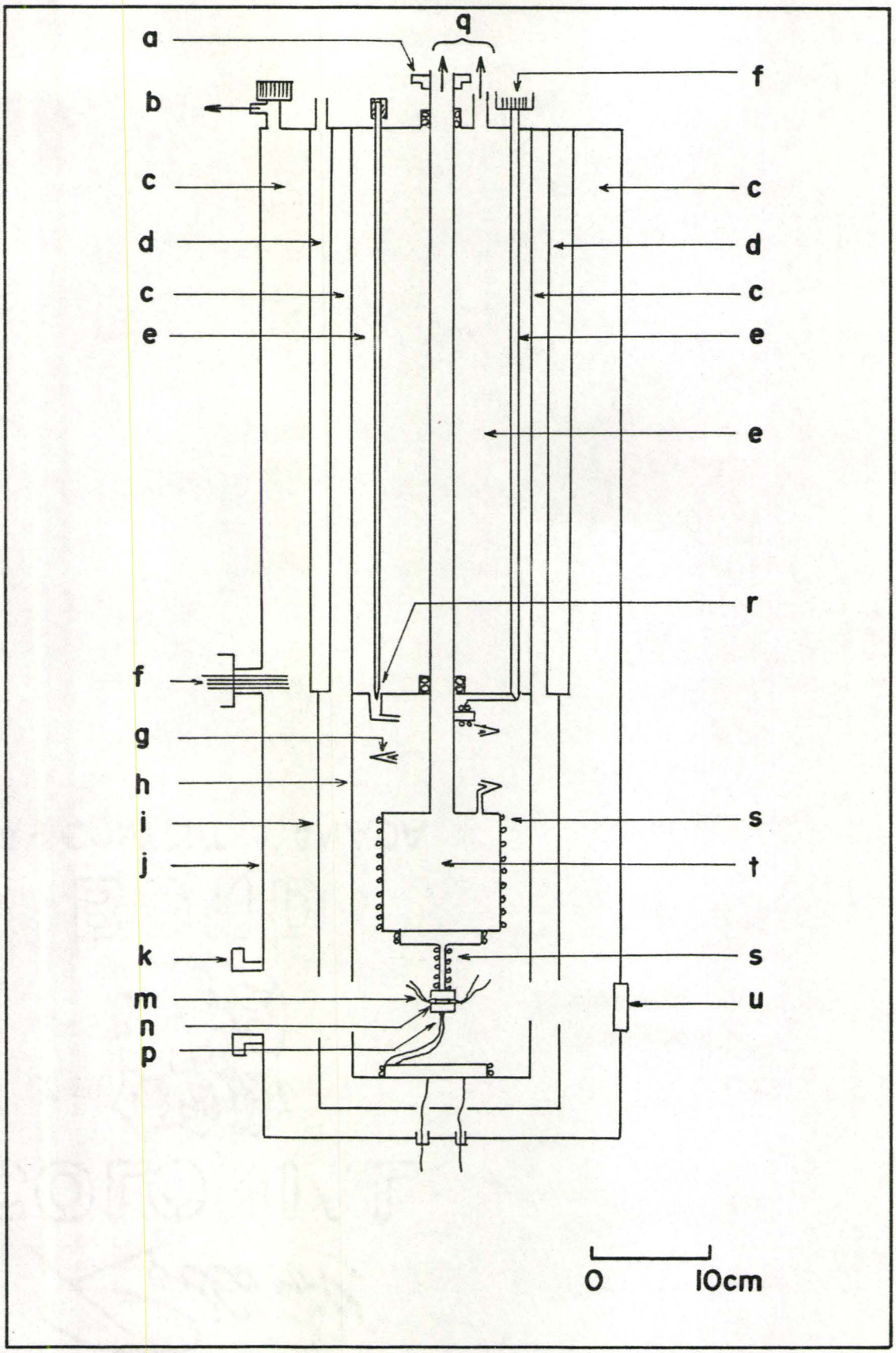
a
q
f
b
c
c
d
d
c
c
e
e
e
r
f
g
h
i
s
j
t
k
s
m
u
n
p
0
10cm

high vacuum space ($P < 1 \times 10^{-6}$ torr). The helium flow from the main reservoir to the smaller pot could be controlled from the top of the cryostat through a needle valve, as shown in Figure 33.

A copper plate of dimensions 20 mm x 20 mm x 2 mm, on which the samples were vapour-deposited, was connected to the lower helium reservoir by a copper rod (d = 2 mm) which provided good thermal contact.

There were four equi-spaced ports in the lower section of the cryostat, in line with the sample deposition block, as shown in cross-section in Figure 34. The ports were made for the electron gun attachment, the sample inlet tube, and the ultraviolet light irradiation and light detection; the fourth port was not used. Some detail about the main ports will be given later in this chapter.

The main modification to the basic MD4A cryostat was the introduction of a rotatable shaft through the main helium reservoir. This insert carried the lower helium pot and the sample block, and was installed to allow the rotation of the sample block to face any of the four ports at any time, without loss of vacuum or refrigerant. (O-ring seals at the top and bottom of the shaft, as shown in Figure 33, made this possible.) The sample block was rotated with a screw mechanism at the top of the cryostat, and its position, as determined on the goniometer, was reproducible to within 1° of arc.

Figure 34: The Tail of the Thermoluminescence Cryostat in Cross-Section.

a - sample inlet port
b - copper-constantan thermocouple
c - heat wires
d - sample inlet tube
e - platinum high voltage feedthrough wire
f - focussing electrode
g - heated filament
h - light detection system
i - high voltage supply to photomultiplier tube
j - output from photomultiplier tube
k - photomultiplier tube
m - mechanical shutter
n - quartz window
p - outside vacuum jacket
q - 77K shield
r - 4.2K shield
s - sample block
t - Speer resistance thermometer
u - spare port
v - vacuum insulation space
w - bellows shutter arrangement
x - electron beam
y - high voltage electrode
z - accelerating electrode
aa - cathode
bb - electron gun

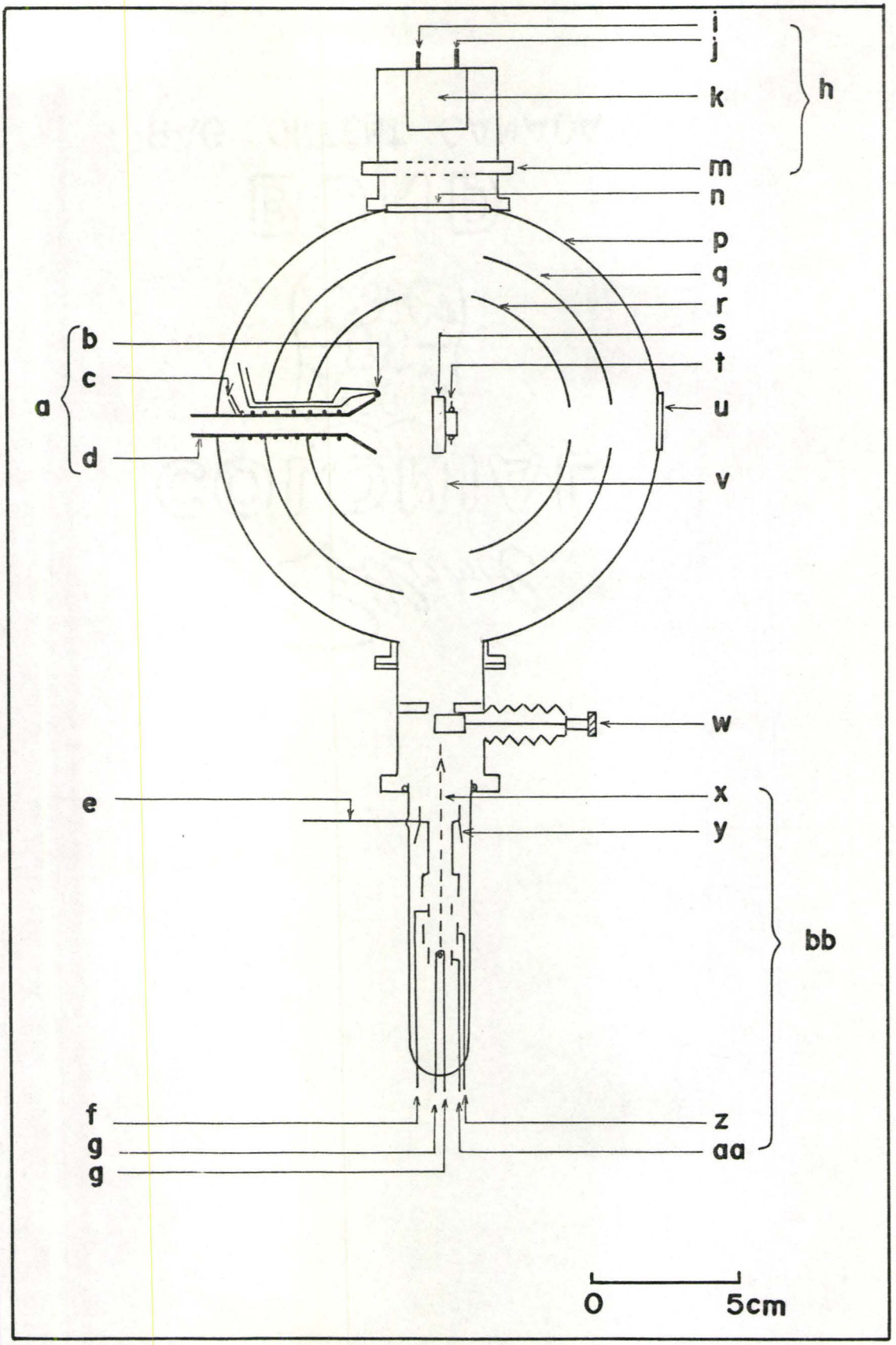
i
j
k
h
m
n
p
q
r
s
t
u
v
b
c
a
d
w
e
x
y
bb
f
g
g
z
aa
0
5cm

(ii) The Sample Deposition Port

The samples were spray-deposited onto the sample block through the sample deposition tube that is shown in Figure 34. The wide-mouthed stainless steel tube was connected via copper tubing to the sample reservoir on the outside of the cryostat and the flow of vapour into the cryostat could be controlled by a needle valve. A copper-constantan thermocouple on the mouth of the sample inlet tube was used to monitor the tube temperature. A heater was wound around the tube to prevent sample solidification in the tube. With no current flowing through its heater, the sample inlet tube temperature was -35°C when the lower helium reservoir was at T = 4.2K (i.e. during deposition conditions).

(iii) Thermometry and Temperature Control of the Sample Block

A carbon resistance thermometer (Speer Carbon Co., St. Marys, Pennsylvania) was attached to the back side of the sample block, and was used to determine the sample temperature during the thermoluminescence measurements. The thermometer was first intercompared with a copper-constantan thermocouple that was attached to the bottom of the block. The thermocouple had been previously calibrated at 4.2K and 77K. This was sufficient to fix the deviation of the emf, characteristic of the particular constantan wire used, from a standard table. The thermocouple and the

thermometer were intercompared over the region 13K $\leq$ T $\leq$ 38K, and gave absolute values of the temperature to within 0.5K, or better. At lower temperatures, copper-constantan thermocouples are rather insensitive, and the resistance of the carbon thermometer was used in the well-known[131] resistance-temperature relationship:

$$\ell n\ R = A + \frac{B}{T} \quad , \tag{42}$$

where R is the resistance, T is the temperature in Kelvin, and A and B are constants of the particular Speer thermometer. Equation (42) was fitted to data for 13K $\leq$ T $\leq$ 20K, and gave the correct temperature down to 4.2K to within 0.5K, or better. The resistance-temperature relationship for the Speer resistor was very reproducible over many coolings.

The lower helium reservoir was usually kept full of liquid helium during the sample deposition and irradiation procedures, in order to maintain the sample block at its lowest temperature. This base temperature, as measured with the carbon thermometer, was approximately 9.5K, rather than 4.2K, due to the large heat input to the block. (The major source of this energy seemed to be the relatively warm sample inlet tube which was less than 2 cm away from the sample block.) As the sample was deposited, the temperature rose to $\sim$ 10K or higher, depending on the deposition rate, due to the heat released on solidification.

To allow the temperature to rise during the thermo-

luminescence measurements, the needle valve to the lower helium pot was closed. When the liquid helium in the pot had evaporated, the temperature of the sample block rose in a regular and reproducible fashion, as shown in Figure 35. A copper heater wire (#36 AWG) was wound around both the lower helium pot and the copper rod connecting the pot to the sample block. After a thermoluminescence experiment, this was used to heat the block and thereby to remove the sample before another was deposited. In addition, careful balance of the current through the heater and the flow of helium into the smaller pot could be used to vary the heating rate from that shown in the figure.

(b) The Irradiation Sources:

Two sources of ionizing radiation were used in the present experiments, and these will be described in some detail.

(i) The Electron Gun

An electron gun, shown schematically in Figure 34, was used to bombard the samples with high energy ($\sim$ 3-25 keV) electrons. Its main element was the gun for a black and white television picture tube (G.T.E. Sylvania, Seneca Falls, New York). The envelope of the tube was made of lead glass, and the principal electrical components were an oxide filament, a cathode, and accelerating, focussing and high voltage electrodes.

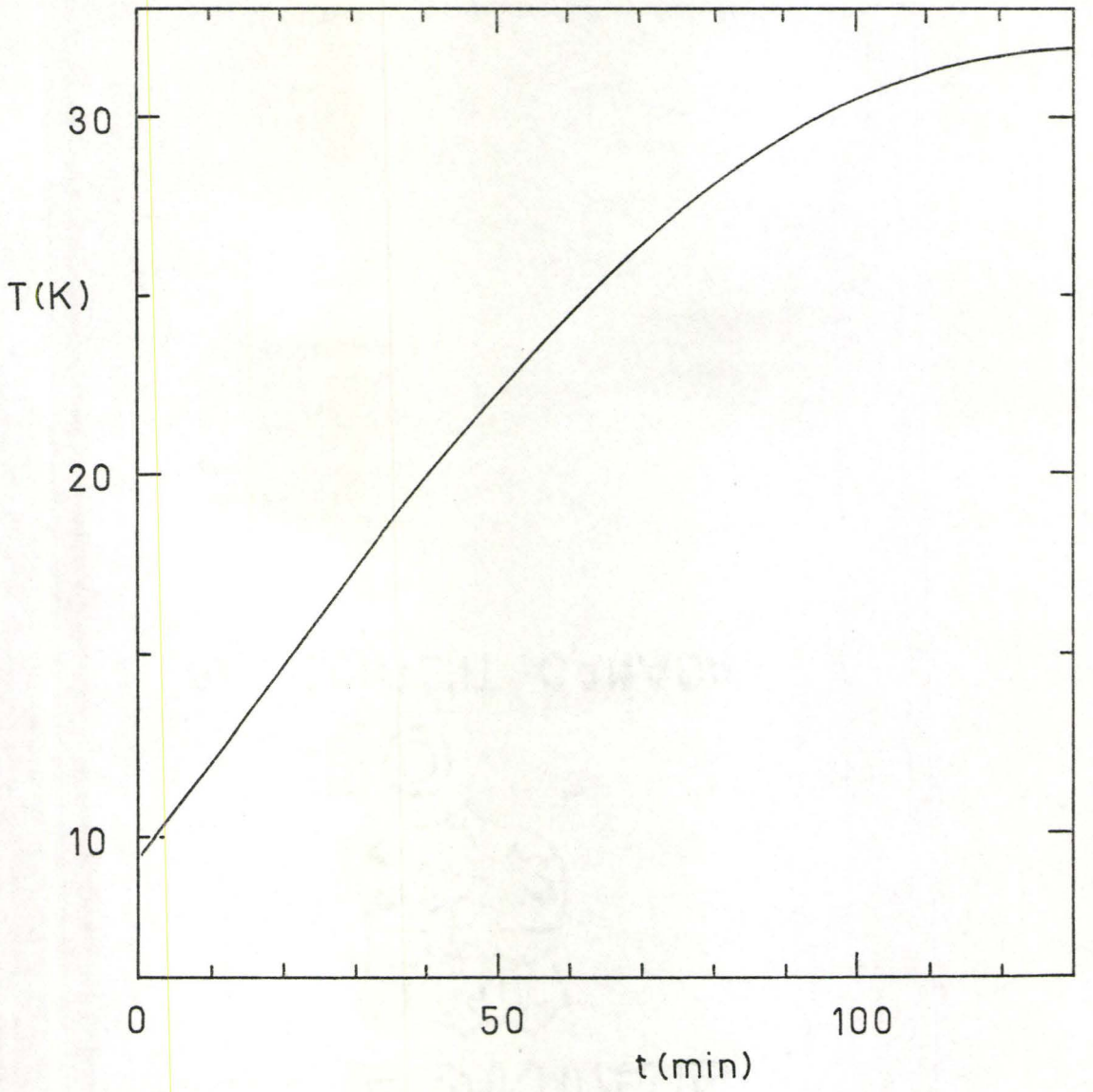

Figure 35: A Typical Heating Curve for a Thermoluminescence Sample.

During its operation, the tube was maintained under high vacuum ($P < 1 \times 10^{-6}$ torr); as shown in Figure 34, the vacuum space was connected with that of the cryostat. The oxide filament was heated with $\sim$ 10V a.c. ($\sim$ 0.5A) applied across it. (As the filament aged, a higher voltage was required to obtain the same beam intensity. The lifetime of a gun was limited by that of the filament, and usually was $\sim$ 100 hr, with several exposures to the atmosphere, each of which severely weakened the filament.) With the cathode grounded, the accelerating, focussing and high voltage electrodes were maintained at + 300V, $\pm$ a few hundred volts and 3-25 kV, respectively, and a beam current of a few μA was obtained.

Before the methane irradiation experiments were carried out, a ZnS phosphor disk was placed over the sample block and the electron beam was aligned on the target. A very broad beam (d $\sim$ 2 cm at the target) was used to give uniform irradiation of the sample.

When the electron beam was not in use, the port to the cryostat was made light tight by a bellows shutter arrangement. (See Figure 34.) The electron gun could easily be detached from the cryostat when it was not required for longer periods of time.

(ii) Irradiation with Ultraviolet Light

A mercury pencil lamp (Spectronics Corp., Westbury,

New York) of principal wavelength 2537 A, and with an intensity of 2×10^{-3} Watt cm^{-2} at a distance of 2.5 cm, was placed at the same optical window which was used for light detection, - approximately 6 cm from the sample block. When the sample had been irradiated with ultraviolet light, the lamp was removed and the light detector was immediately positioned. (The delay between the end of the UV-irradiation and the detection of the emitted light was usually < 30 sec.)

(c) Light Detection

An RCA 6199 head-on photomultiplier tube was used to detect the light from the sample. The tube had its maximum sensitivity in the range $3000A \lesssim \lambda \lesssim 6000A$, with an absolute maximum at $\lambda = 4400A$. It was operated at a voltage of -900V. The tube output ($\sim 10^{-9}$ Amps) was amplified with an electrometer (Kiethley Instruments, Inc., Cleveland, Ohio) and recorded on a chart recorder.

To measure the background response to the photomultiplier tube, a mechanical shutter mounted between the cryostat and the detector was closed and opened intermittently during the luminescence measurements.

Part C: Results and Discussion

Before the luminescence of irradiated methane was measured, a blank experiment was performed to determine the background light levels: a clean sample block was irradiated

and heated, but no emitted light was detected. This showed that the luminescence that was observed in the experiments to be described can be attributed totally to the deposited samples.

1. The Isothermal Luminescence

Immediately following the deposition and irradiation of a methane/aromatic sample, and before the temperature was allowed to increase, luminescence was observed. The light given off was a purple colour ($\lambda \sim 4000$A), and was observed both for samples that had been bombarded with electrons and for those which had been irradiated with UV light. Since the latter samples gave significantly more luminescence, and the light output could be measured within 30 sec of the end of the irradiation (compared with a delay of $\sim$ 2 min for the electron gun irradiation, principally spent to rotate the sample block 180° to face the light detector), only the results for the UV-irradiation will be presented here. (It should be noted, however, that the electron bombardment results were qualitatively similar.)

A typical decay of the isothermal luminescence is shown in Figure 36. These data are for a sample of CH_4 + 0.05 mole % benzene, but a very similar decay curve was observed for CH_4/toluene, CD_4/benzene and CD_4/toluene at various impurity concentrations. The decay can be clearly resolved into two processes - one short-lived and one long-

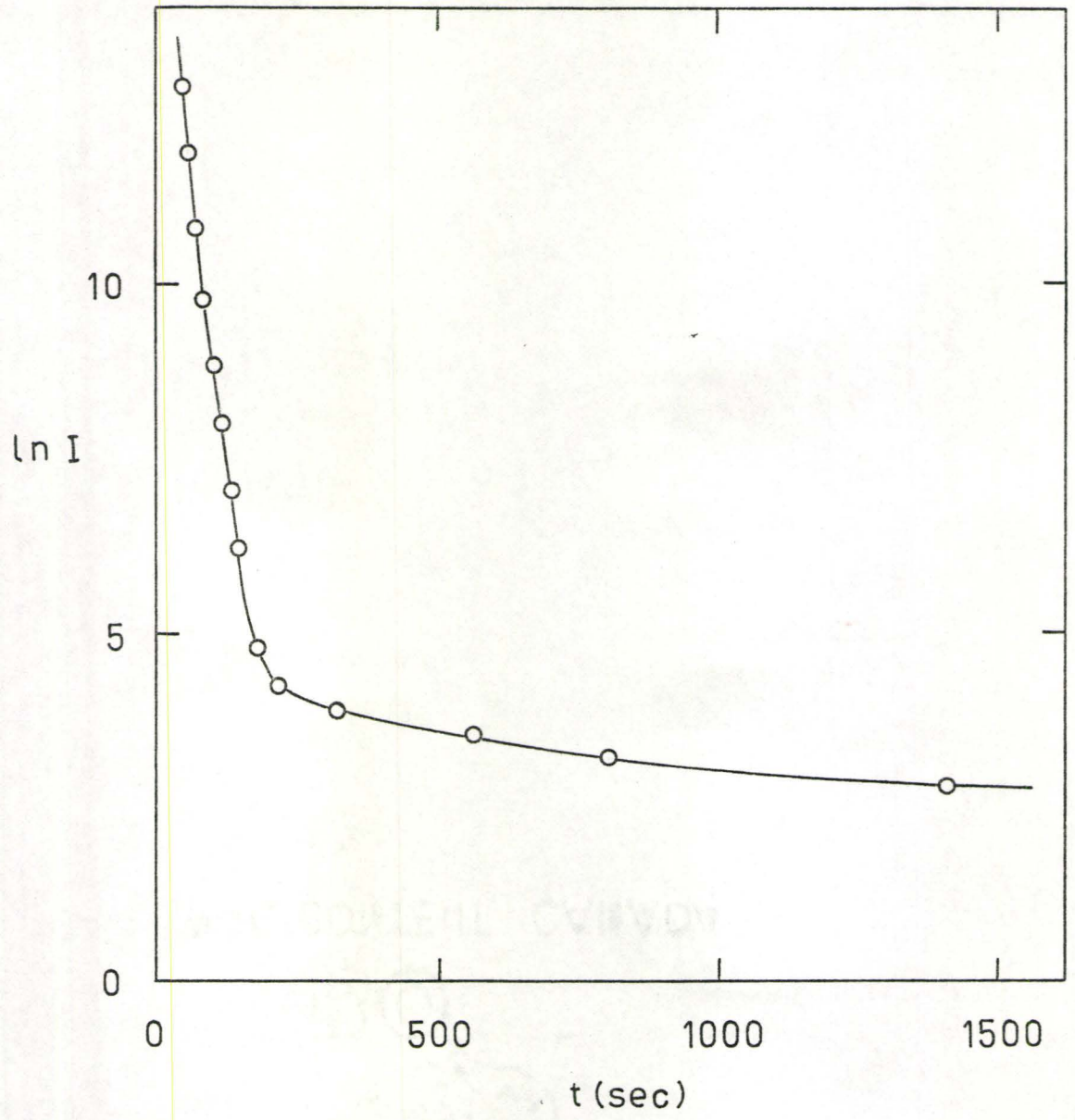

Figure 36: The Decay of Isothermal Luminescence.

The data shown are for 57 mg of CH_4 + 0.05 mole % benzene after 12.0 min of UV-irradiation; $\bar{T}$ = 10.0 K; the luminescence intensity is in arbitrary units.

lived, and these will be examined separately.

(a) The Short-Lived Process ($t \lesssim 120$ sec)

As shown in Figure 37, ℓn I is linear in time for several concentrations of aromatic impurities in CH_4 and CD_4 within approximately the first two minutes after the UV irradiation source was shut off. The lifetime of the process, as derived from the slope of the curves shown in Figure 37, is independent of the matrix (CH_4 or CD_4), but depends on the added impurity (benzene or toluene). The decay is due to solute phosphorescence, and the observed lifetimes (τ = 15 sec for benzene, τ = 12 sec for toluene) are consistent with those reported in the literature.[164]

(b) The Long-Lived Process ($t \gtrsim 200$ sec)

After the solute phosphorescence has decayed sufficiently, a plot of ℓn I against ℓn t gives a linear relationship. (See Figure 38.) The decay of the luminescence intensity can therefore be written as

$$I = k\, t^{-m} \quad , \tag{43}$$

where k is a scaling parameter, and m = 0.72 ± 0.04. The value of m was found to be independent of the nature of the solutes and matrices used here, and also of the solute concentration. A similar decay of the long-lived isothermal luminescence has been observed in many other solute/solvent

Figure 37: The Isothermal Decay of the Short-Lived Luminescence.

◐ 57 mg of CH_4 + 0.05 mole % benzene.

\+ 70 mg of CD_4 + 0.009 mole % benzene.

O 12 mg of CH_4 + 0.008 mole % toluene.

● 55 mg of CD_4 + 0.008 mole % toluene.

All decays were recorded at T = 10.0K after 12.0 min of UV-irradiation, and intensities shown are in arbitrary units.

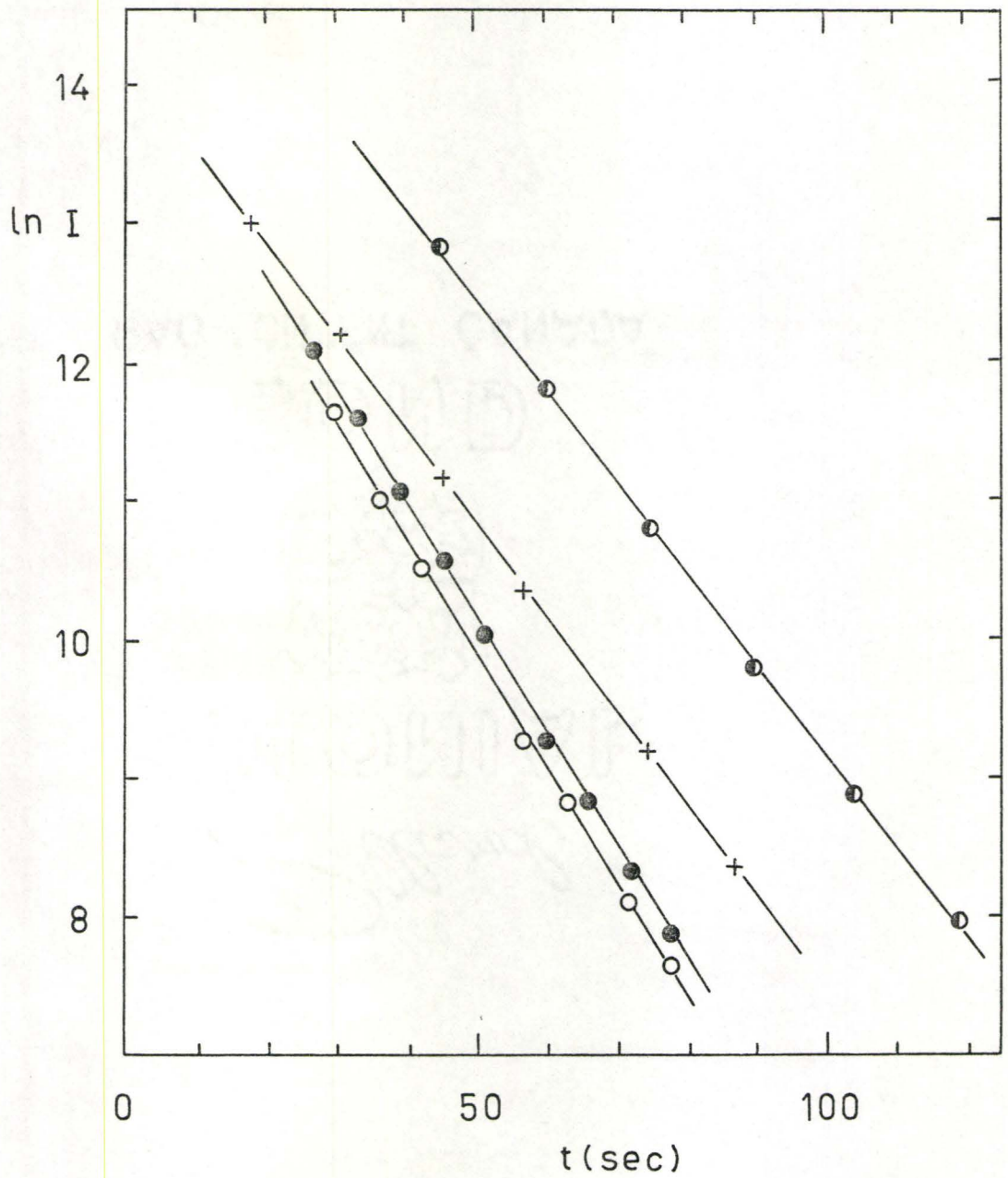
14
ln I
12
10
8
0
50
100
t(sec)

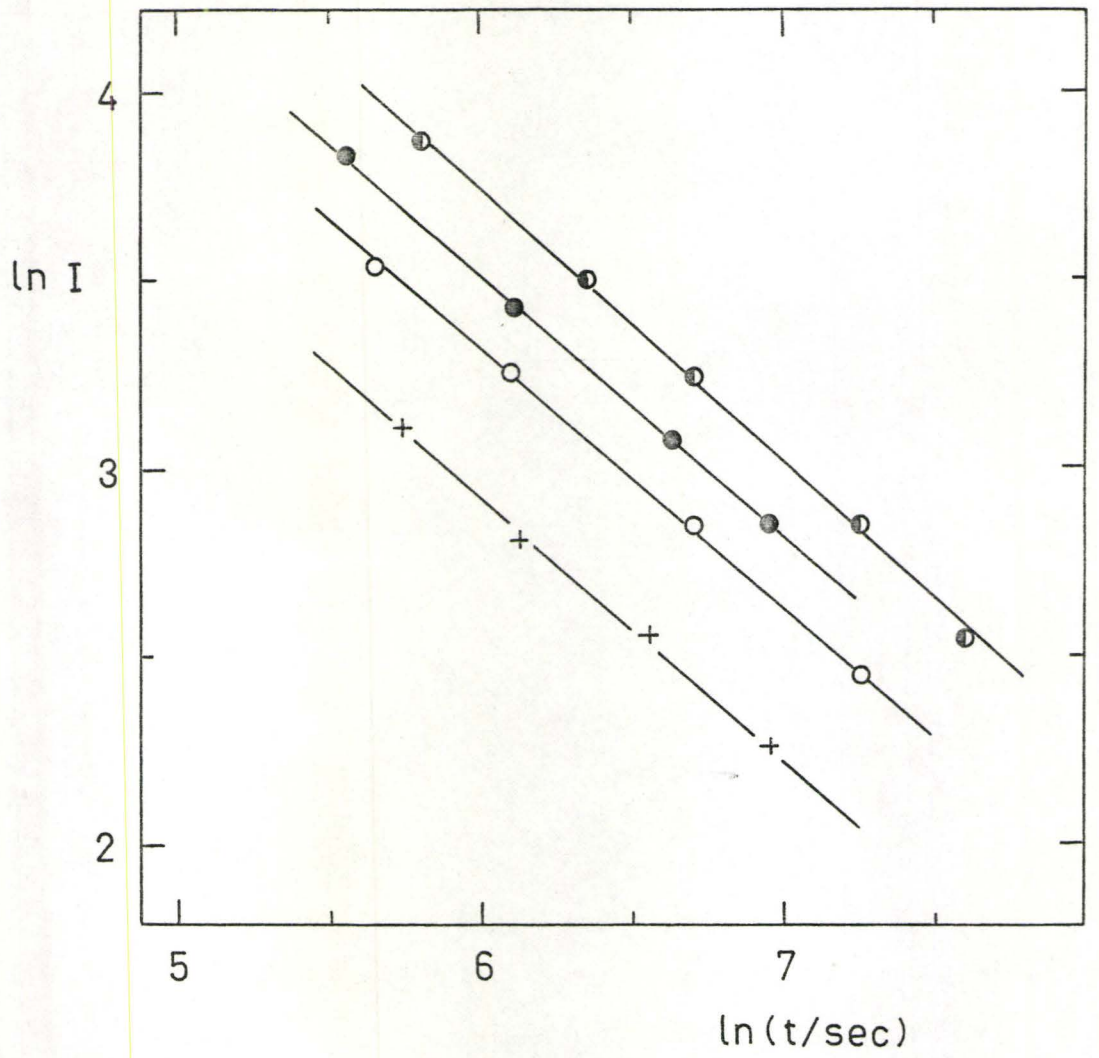

Figure 38: The Isothermal Decay of the Long-Lived Luminescence. (Legend as for Figure 37.)

systems, and is generally accepted to be due to the slow recombination of trapped electrons with cations[157,161,165-70] (vide supra, Section V.A, equations [1] - [4].)

2. Thermoluminescence

(a) Electron Bombardment

As mentioned earlier, the presence of an aromatic solute is essential for the observation of luminescence from saturated alkanes. Even with rather high solute concentrations (∿ 1.0 mole %), only a very small luminescence response was observed after electron bombardment of the methane/aromatic solid solution, primarily due to lack of penetration of the electron beam. (The highest potential used here was ∿ 25 keV, yet the resulting beam would be expected to penetrate the sample to no more than a few thousand Ångstroms, i.e. less than 1% of the sample thickness, assuming that the penetration is similar to that of 25 keV electrons in aluminum.[171])

The luminescence response increased considerably when the electron bombardment was carried out during sample deposition. The sample block was positioned half-way between the usual deposition and electron-irradiation positions, such that the jet of vapour and the electron beam each made a 45° angle with the face of the sample block. However, rather high impurity concentrations (∿ 0.1 mole %) were still required to see a measurable response with this method and a similar response could be obtained with much lower solute

levels ($\lesssim$ 0.005 mole %) with the use of UV-irradiation. For this reason, only the results of samples which have been exposed to UV light will be presented here, although the electron bombardment results show many of the same features.

(b) Results from UV-Irradiation

Many factors, such as the sample size, heating rate and specimen preparation, have been reported to influence the glow curves of molecular solids, but they have not previously been studied systematically and the reproducibility of many of the earlier studies can therefore be questioned. An attempt was made to investigate these factors thoroughly; the present results will show the limitations on the absolute determination of a glow curve for a particular matrix/solute system.

(i) The Isothermal Decay Time

The luminescence from a UV irradiated methane/aromatic sample was usually allowed to decay for $\sim$ 30 min. When it was allowed to decrease for $\sim$ 6 hr, the features of the subsequent glow curve were the same, but the intensity was significantly reduced because many of the electrons had already recombined with cations before the sample was heated. This is illustrated in Figure 39 for CH_4/toluene. (It should be noted here that the positions of the peaks appeared to shift by up to 1K from one sample to another; this was

Figure 39: The Effect of the Isothermal Luminescence Decay Time on the Glow Curve.

- O 54 mg of CH_4 + 0.008 mole % toluene; ITL decayed for 0.5 hr.
- ● 54 mg of CH_4 + 0.007 mole % toluene; ITL decayed for 6.0 hr.; x5 indicates that the intensity shown in 5 times that observed.

(Both samples had been exposed to 12.0 min of UV radiation.)

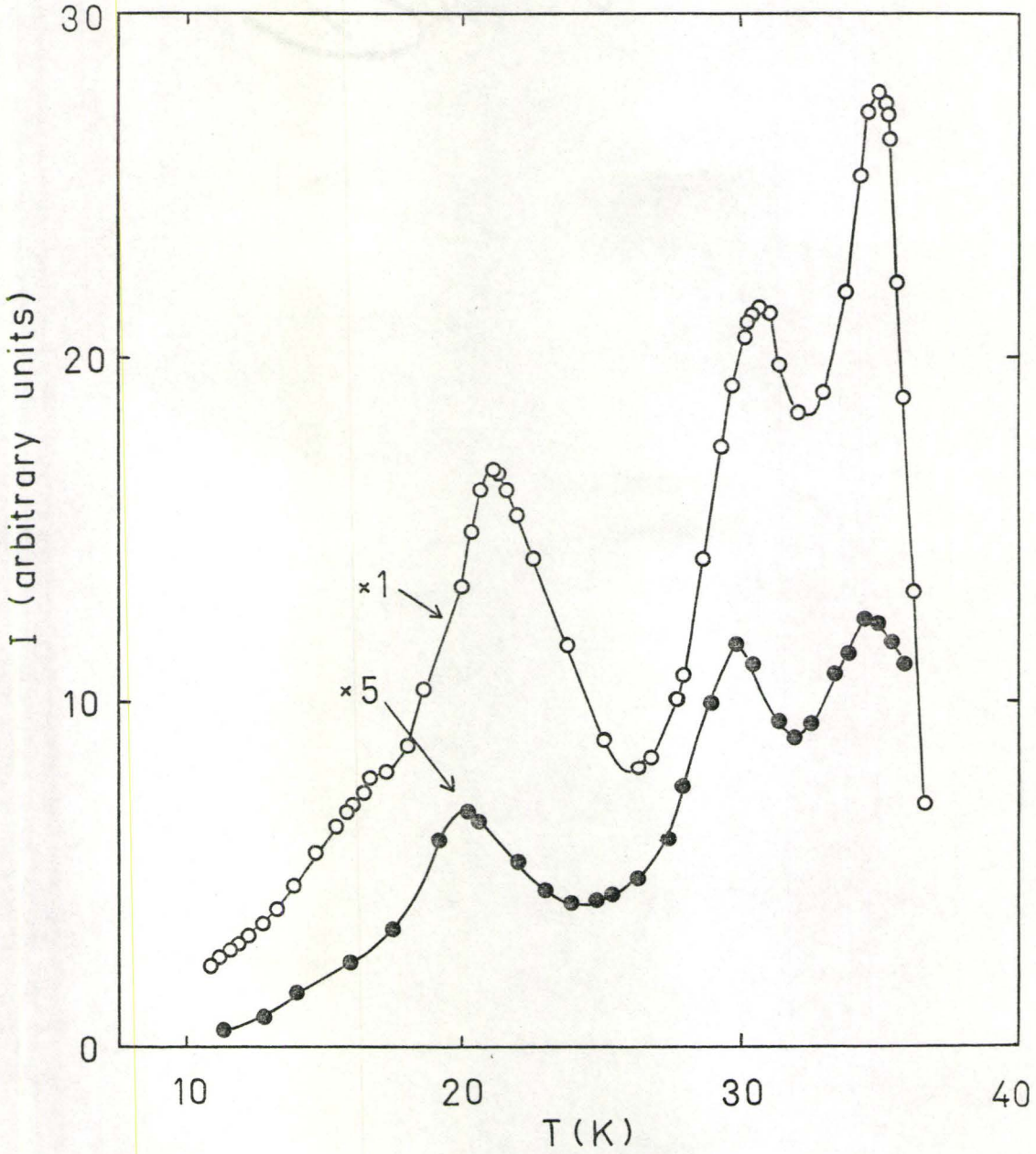
30
20
10
0
I (arbitrary units)
×1
×5
10
20
30
40
T(K)

probably caused by variable thermal contact between the sample and the block.) The luminescence of most samples was allowed to decay at T = 10.0K for 30 min before the thermoluminescence was observed.

(ii) Warming Rates

Kinetic analyses[159,171-2] of the thermoluminescence peaks associated with the recombination of thermally detrapped electrons with positive species, have indicated that the peak positions can shift to higher temperatures as the heating rate is increased. Figure 40 illustrates that the shift of the peaks is insignificant for the variation in heating rates used here. The luminescence intensity appears to be somewhat reduced in the sample which was heated more slowly, but the total intensity (i.e. integrated over time) is similar for the two heating rates.

(iii) The Effect of Sample Size

Sugawara and Tabata[162] reported grossly different thermoluminescence curves for alkane/toluene samples when the size was varied from ∿ 5 mg to ∿ 30 mg. In the current experiments, the shapes of the glow curves for methane/aromatic mixtures are found to be independent of the sample size, from 200 mg to < 2 mg. (Representative glow curves are shown for CH_4/toluene in Figure 41.) A source of irreproducibility in the earlier work[162] might have been

Figure 40: The Glow Curve for Two Different Heating Rates.

- O 54 mg of CH_4 + 0.008 mole % toluene; heating rate as in Figure 35.
- ● 54 mg of CH_4 + 0.008 mole % toluene; heating rate constant at 0.14K min^{-1}.

(Both samples were UV-irradiated for 12.0 min.)

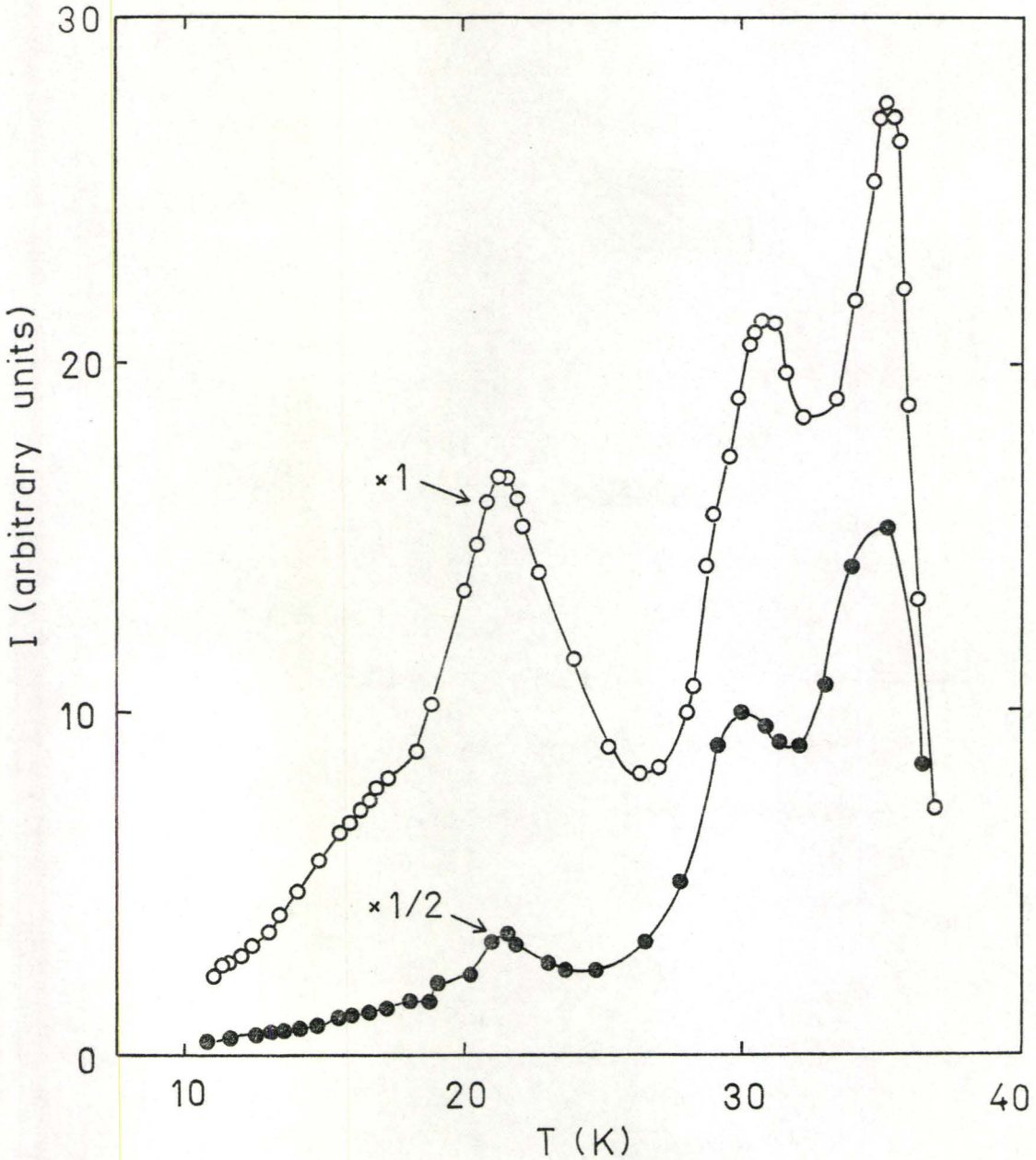
30
20
10
0
I (arbitrary units)
×1
×1/2
10
20
30
40
T (K)

Figure 41: The Effect of the Sample Size and Solute Concentration on the Glow Curve.

O 54 mg of CH_4 + 0.008 mole % toluene.

● 54 mg of CH_4 + 0.0009 mole % toluene.

× 12 mg of CH_4 + 0.008 mole % toluene.

(All three samples were UV-irradiated for 12.0 min.)

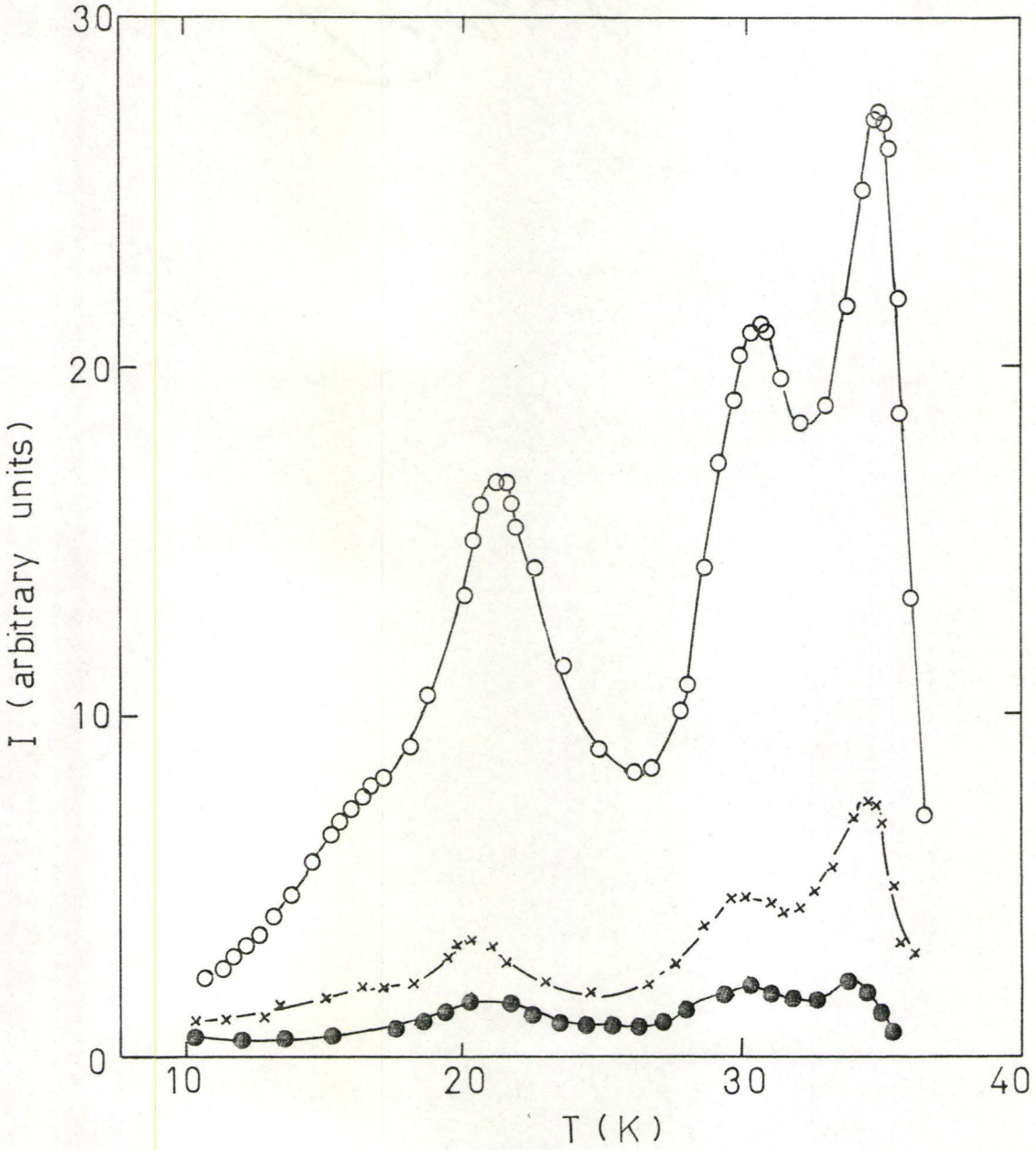
30
20
10
0
I (arbitrary units)
10
20
30
40
T (K)

the extremely rapid heating rate used at low temperatures (as high as $\sim$ 20 K min^{-1} at the start of the glow curve); this, in combination with possible deterioration of thermal contact for the larger samples, may have given rise to their apparent sample size effects.

(iv) Solute Concentrations

As illustrated in Figure 41, the shape of the glow curve of CH_4/toluene was independent of the solute concentration. This was true for all methane/aromatic samples used, over a solute concentration range of 0.001 to 0.5 mole %. In fact, it can be seen from the figure that the luminescence intensities in the present glow curves scale to the total number of moles of solute present.

UV-irradiation has the advantage over electron bombardment that a much lower solute concentration is needed to yield measurable luminescence, and therefore the host lattice structure is less likely to be disrupted. But its disadvantage is that it is so sensitive: when undoped methane was used, the luminescence response indicated the presence of a few ppm of aromatic solute. The impurity was apparently picked up from the walls of the sample inlet system, because, after these were baked out, "pure" methane gave a negligible luminescence response.

(v) The Effect of the Sample Deposition Rate

The vapour deposition method has been used to prepare glassy or non-crystalline samples of CH_3OH and H_2O.[173] It is improbable, however, that glassy methane was formed here, because extremely slow deposition rates were not used. (If the deposition is carried out rapidly, the heat released on solidification will provide sufficient energy to crystallize the sample.)

In the present experiments, the deposition rate was varied by more than a factor of 10 without any change in the main features of the glow curves. (See Figure 42, for example.) This result indicated that the samples used were probably crystalline, and this was confirmed by annealing studies.

(vi) Sample Annealing

Samples which were annealed at T = 40K, i.e. in phase I, showed similar glow curves to those which had not been annealed. (See Figure 43.) In solids which are known to form glasses, such as C_2H_5OH and CH_3OH/H_2O, thermoluminescence is strongly dependent on the thermal treatment of the sample[161,163]; it can therefore be concluded that the present specimens were crystalline.

(vii) The Effect of the Solute on the Glow Curves

Variation of the solute, although not often considered

Figure 42: The Effect of the Sample Deposition Rate on the Glow Curve.

- O 12 mg of CH_4 + 0.008 mole % toluene; deposition rate was ∿ 12 mg min^{-1}.
- ● 21 mg of CH_4 + 0.0007 mole % toluene; deposition rate was ∿ 1.8 mg min^{-1}.

(Both samples were UV-irradiated for 12.0 min.)

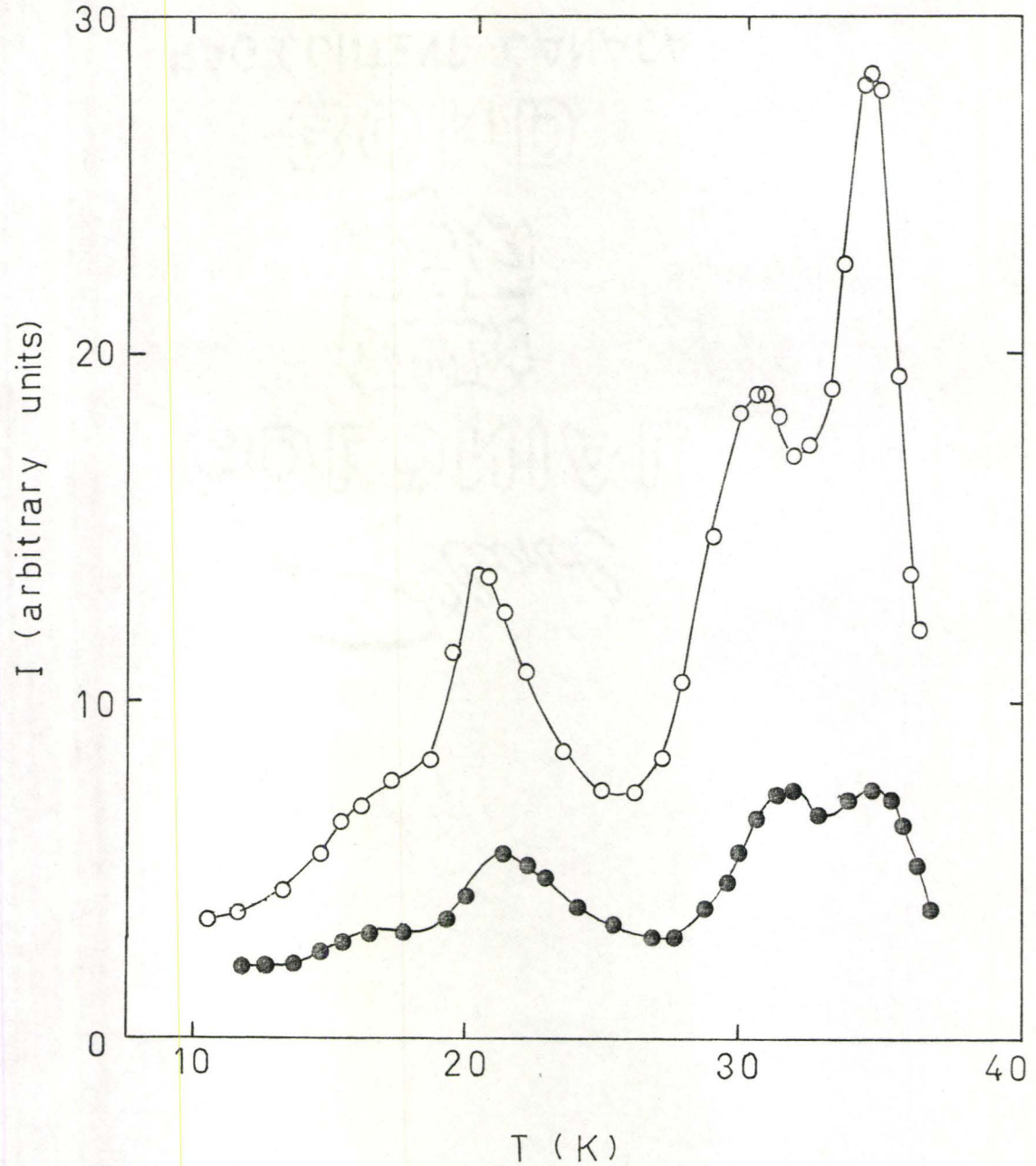
30
20
10
0
I (arbitrary units)
10
20
30
40
T (K)

Figure 43: The Glow Curve Before and After Annealing at T = 40K.

○ 36 mg of "impure" CD_4 + 0.007 mole % toluene after 12.0 min of UV-irradiation and 30 min of ITL decay.

● same sample after annealing at T = 40K, re-cooled and re-irradiated for 12.0 min with UV light.

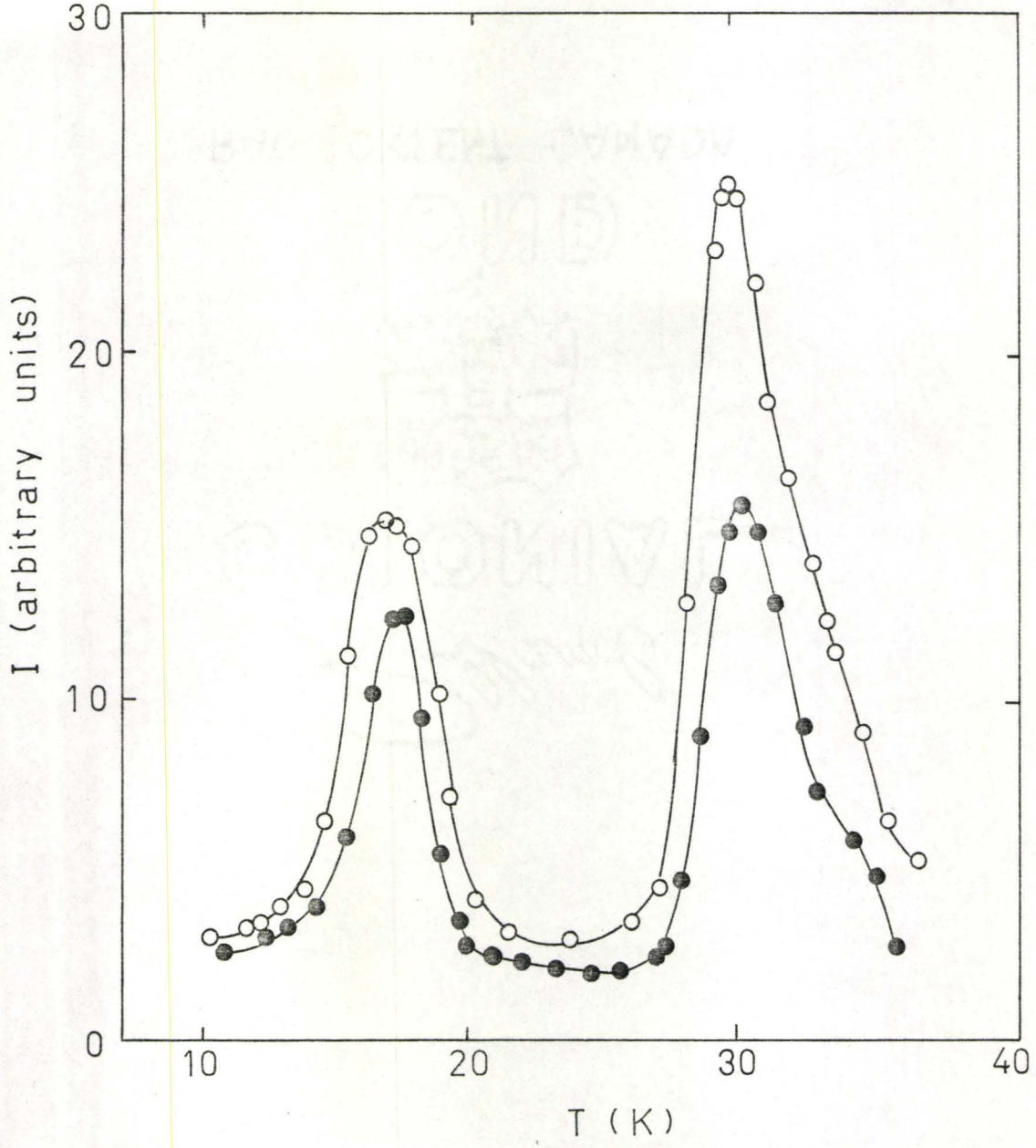
30
20
10
0
I (arbitrary units)
10
20
30
40
T (K)

in thermoluminescence studies, has been shown to have little effect on the shape of the glow curves of squalane[174] and polystyrene[175], as well as many other organic matrices.[154] The prevailing view is that the solute only serves to increase the luminescence, but some specific effects were found in the present experiments.

In Figures 40-42 typical glow curves are shown for CH_4/toluene. The results indicate the presence of 3 or possibly 4 distinct peaks, at temperatures of (16), 20, 30 and 34K. Similarly, Figure 43 shows 2 or possibly 3 distinct peaks for CD_4/toluene; these are at temperatures of 17, 30 and (34)K. It is not surprising to see differences between the glow curves of CH_4/toluene and CD_4/toluene because there are differences in the CH_4 and CD_4 phase diagrams (see Figures 7 and 8), but the change of the thermoluminescence on substitution of benzene for toluene is remarkable.

Figure 44 shows the glow curve of CH_4/benzene. The profile is much different from that of CH_4/toluene. A much sharper peak is observed at T = 20K, and only one other peak is observed (at T = 37K) with benzene as the solute.

When mixed with benzene, CD_4 that has not been treated in any way gives the glow curve that is displayed in Figure 45. At least 2 broad peaks are observed, at T = 20 and 36K. When the CD_4 was treated by cooling, as described in Section V.B.1, the glow curve shown in Figure 46 was observed for 10 of 20 experiments; the others yielded curves such as that illustrated

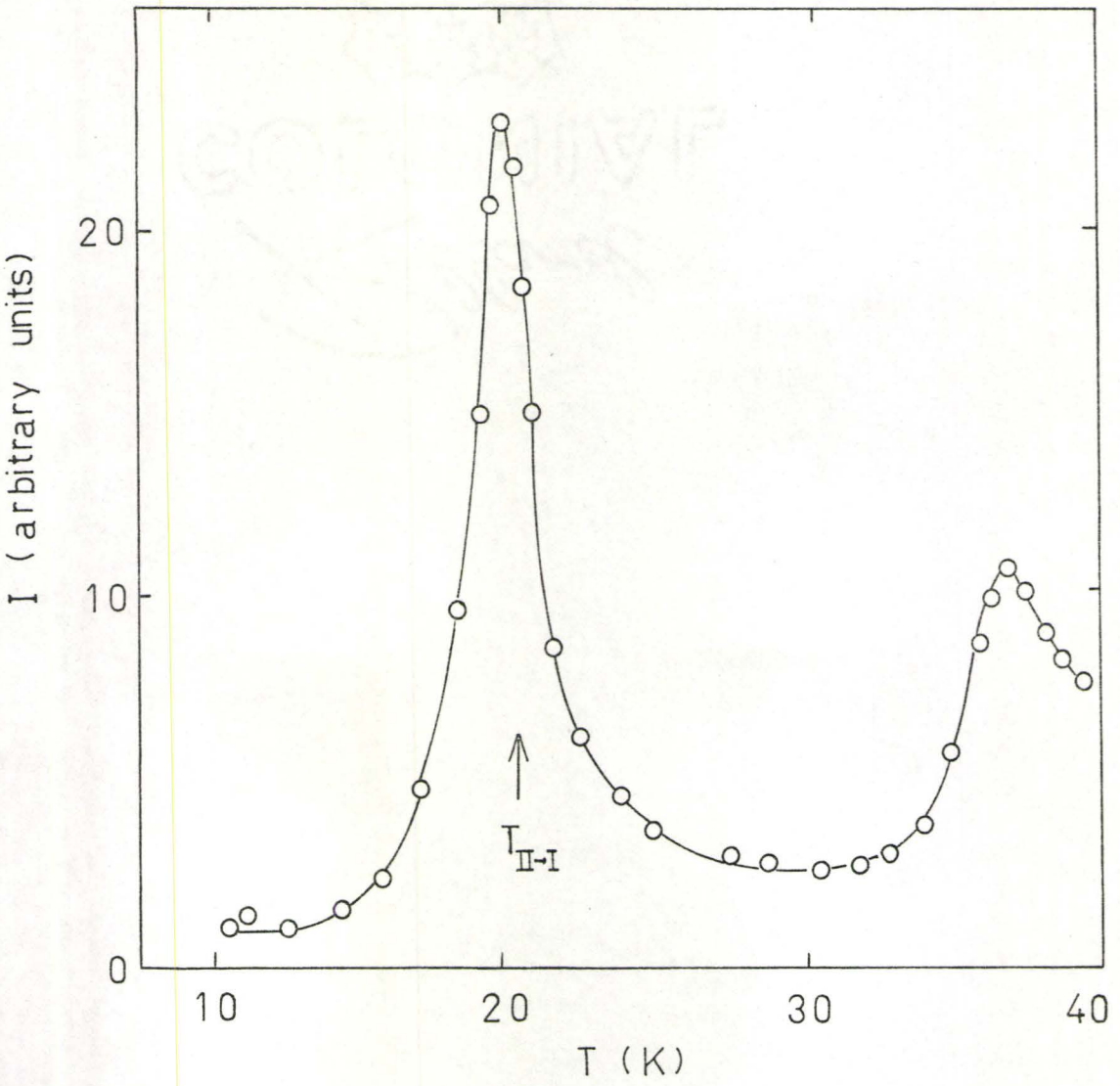

Figure 44: The Glow Curve of CH_4/Benzene.

The data shown are for 57 mg of CH_4 + 0.011 mole % benzene after 12.0 min of UV irradiation.

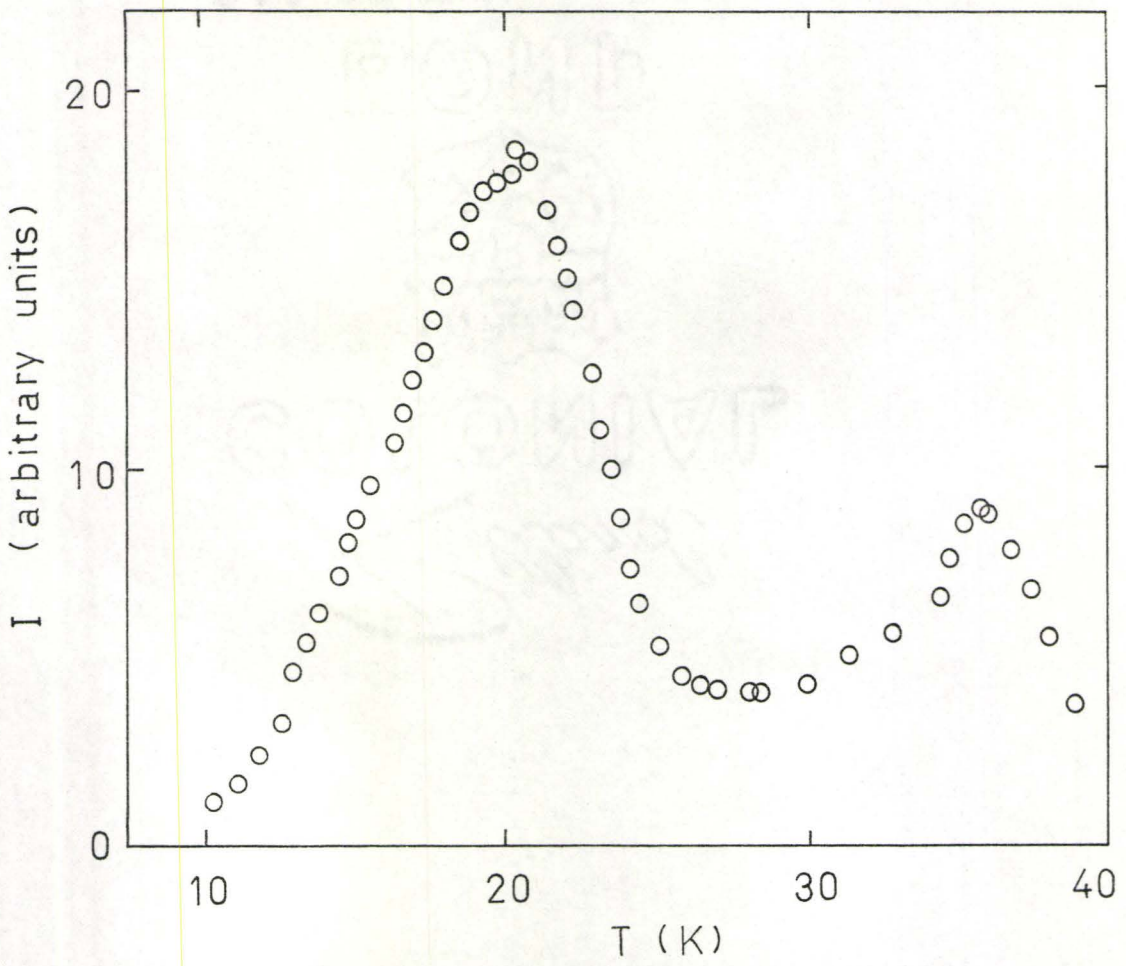

Figure 45: The Glow Curve of "Impure" CD_4/Benzene.

The data shown are for 70 mg of CD_4 (not purified) + 0.05 mole % benzene after 12.0 min of UV-irradiation.

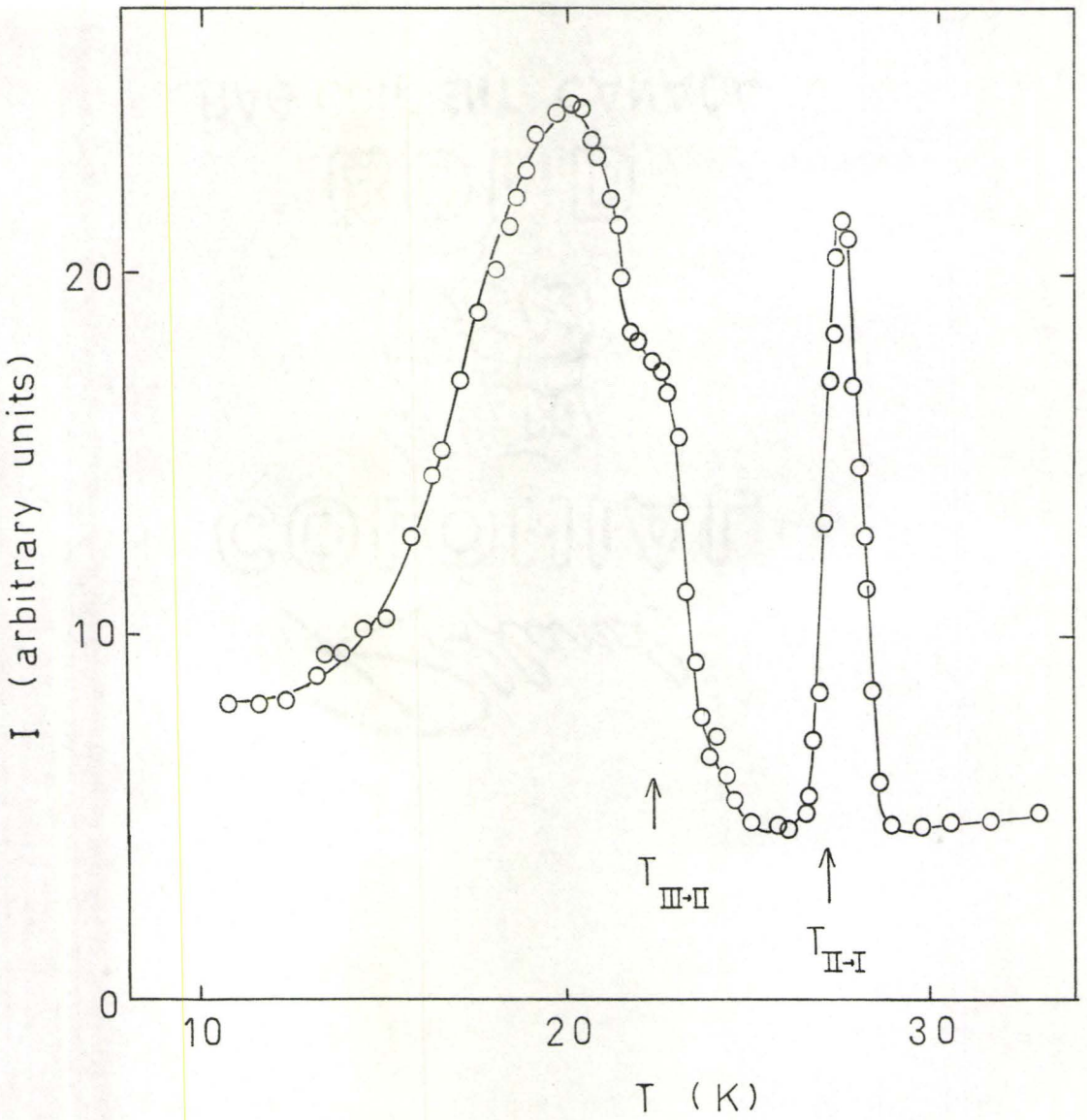

Figure 46: The Glow Curve of "Purified" CD_4/Benzene.

The data shown are for 70 mg of CD_4 (treated as described in Section V.B.1) + 0.05 mole % benzene, after 12.0 min of UV-irradiation.

for "impure" CD_4/benzene (Figure 45). Since the only factor that could have changed was the distribution of impurity in the CD_4, it must be concluded that extremely small amounts of impurity can greatly influence the thermoluminescence profile. The glow curve that was observed for cooled CD_4/benzene displayed a sharp peak at T = 20K, with a shoulder at T = 22K and a very sharp peak at T = 27K. The results show clearly that the glow curve depends not only on the matrix, but also on the nature of the added solute molecules and on very small amounts of accidental impurities.

(c) Discussion of the Thermoluminescence Results

The presence of both sharp and broad peaks in the glow curves indicates that two processes give rise to electron detrapping. Each of the broad peaks can be attributed to one or more Randall Wilkins processes[159], i.e. thermally activated recombination of electrons and cations. The distribution of the electron trap depths and the distance from the trapped electron to the parent cation depends on both the solute (benzene or toluene) and the matrix (CH_4 or CD_4) which were used. It is the sharp peaks, however, which are of more interest at present.

As noted in Chapter II, CH_4 undergoes a phase transition from phase II → I at T = 20.5K. Similarly, CD_4 transforms from phase III → II at T = 22.0K, and from phase II → I at T = 26.9K. The establishment of a correlation

between thermoluminescence peaks and the presence of these solid-solid phase transitions was one of the primary objects of the present experiments. Although it may have an underlying Randall Wilkins component, it is probable that the sharp peak at T = 20K in CH_4/benzene is due to the CH_4 phase transition; similarly, the shoulder at T = 22K and the sharp peak at T = 27K for CD_4/benzene seem to correlate with the phase transitions in CD_4. The results with toluene as the solute are less clear-cut: it is possible that the luminescence from the recombination brought on by the phase II → I transition in CH_4/toluene is masked by processes associated with the thermalization of electrons when they recombine with $C_6H_5CH_3^+$. Sharp peaks from the phase transition-induced luminescence are absent in CD_4/toluene, possibly because of the accidental impurities in the CD_4. (The thermoluminescence of CD_4/toluene was not investigated further because of the interference of processes which are intrinsic to the toluene in this matrix in the same temperature region.) It should be noted that the evidence of sample crystallinity given earlier indicates that the phase transitions still take place in impure CD_4; a possible reason for the absence of the associated thermoluminescence is that the impurities tightly bind electrons that would otherwise be detrapped during any lattice rearrangements at the phase transitions.

Although it has not been as straightforward an experimental investigation as was envisaged, the results

yield evidence for a correlation between the solid-solid phase transitions in CH_4 and CD_4, and sharp peaks in their thermoluminescence glow curves. The results with benzene as a solute will be examined further.

The positions of the sharp peaks correlate with the phase transition temperatures, but the precise peak temperature varied from sample to sample by as much as 1K. In one example, the higher temperature peak in CD_4/benzene was a sharp doublet, and the sample was observed to consist of two distinct flakes on the copper block. The position of the peak with respect to the temperature as measured at the carbon thermometer on the back of the block undoubtedly depends on the thermal contact between the sample and the block. The peak width at half height also varied from one sample to another; it ranged from $\sim$ 0.3K to $\sim$ 1K for the phase II $\rightarrow$ I transition in both CH_4 and CD_4. This could be caused by a series of domain type structures within the sample, with a resulting distribution of phase transitions as a function of time. If the glow curve of a sample at a uniform temperature and in perfect thermal contact with the thermometer could be realized, a correlation between the peak widths and the two-phase coexistence region would be expected. For example, an X-ray diffraction study of CH_4 shows no appreciable coexistence between phases I and II[40], while similar experiments show a range of coexistence of 0.10K for the III $\rightarrow$ II and II $\rightarrow$ I transitions in CD_4.[41] (The differences between CH_4

and CD_4 seem to be attributable to the intrinsic widths of the phase transitions.[41] The temperature gradients across the samples also, unfortunately, preclude the possibility of making an analysis of the kinetics of the transitions as seen through the thermoluminescence peaks.

In order to speculate about their release at the phase transitions, it is important to have a clear picture of the trapped electrons. In a polar matrix, the immobilized electron will be stabilized primarily by its interaction with the permanent dipole moments of the surrounding molecules. In saturated alkane matrices, however, the driving force which stabilizes the trapped electrons must be induced dipole and/or higher moments. The absorption spectra of the trapped electrons would therefore be expected to reflect this stabilization, and this is indeed the case: values of λ of $\sim$ 15000A and $\sim$ 6000A have been observed for electrons trapped in alkanes and in polar organic matrices, respectively.[154] Many experiments have been carried out to determine the mean distance between the cations and the trapped electrons[154]; the result is that an electron is usually trapped at a distance of 20-100A from the parent cation, and will therefore preferentially neutralize it during the recombination process.

Two distinct processes could suddenly lower the barrier to electron-cation recombination at the methane phase transitions: changes in the orientational order of the molecules, and translational motion of the centres of mass.

The latter mechanism would allow facile recombination at phase transitions where there is a major centre of mass rearrangement, but, in the transitions in the methanes, the volume changes are very small ($\sim$ 1%)[48], and in some other cases, such as neopentane, a sharp thermoluminescence peak is seen at a second order phase change![54] If the translational motion was dominant during the phase transformation, it would be expected that the thermoluminescence at the phase transitions would not depend critically on very small amounts of impurities; the molecular jumps would lower the barrier so much that even very deeply trapped electrons would be released. Therefore, it is possible that the orientational changes alone are responsible for the thermoluminescence that is observed at the phase transitions in solid methane, although the exact mechanism of electron detrapping is not at all obvious.

The present investigation has yielded evidence for the correlation of phase transitions with thermoluminescence glow peaks but the experimental circumstances have turned out not to be ideal. The vapour deposition method was developed specifically for electron beam irradiation of low penetration. With ultraviolet radiation it would be possible to consider using bulk specimens - even single crystals. Such a system would have many advantages. The present difficulties associated with thermal gradients and temperature measurement could be overcome and more information could be gained about the absolute shapes and positions of the peaks. This, in turn,

would allow kinetic analysis of the thermoluminescence at the phase transitions. In conjunction with more studies of the actual physical mechanism which takes place at the phase transitions, as called for in the previous chapter, these experiments would lead to a better understanding of the relationships between thermoluminescence and orientational ordering in the solid methanes.

Chapter VI

SUMMARY

In order to make deductions about the nature of phase III, the lowest temperature phase of solid methane, the heat capacities of isotopically purified CH_2D_2, CHD_3 and CD_4 were measured in the region $0.15K \leq T \leq 3.5K$.

The low temperature entropy of the solid, as deduced from the present measurements, indicated that phase III is not classically orientationally ordered. It is concluded that it has a complex structure, with a minimum of three intercollated sublattices, in agreement with the conclusions of recent theoretical calculations[111] and spectroscopic experiments![115-6] A 3-site model that accounts for the thermal properties of the partially deuterated methanes in phase III is presented.

The present results also indicate that, unlike CH_4 and CH_3D, CH_2D_2 and CHD_3 do not show nuclear spin symmetry species conversion. The increase in the thermal relaxation times at very low temperatures in CD_4 suggests that conversion takes place in this methane.

From the positions and shapes of the Schottky heat capacity anomalies, limits are placed on the energy level splittings in these methanes. The results are compared with recent neutron inelastic scattering data for CD_4, and with

theoretical predictions for the others.

In addition, a systematic experimental study of the relationship between the solid-solid phase transitions of the methanes and the thermally-stimulated luminescence of electron- and ultraviolet-irradiated methane (CH_4, CD_4)/ aromatic (toluene, benzene) mixtures in the form of thin films is described. Although a correlation is found between the temperatures of the phase transitions and sharp peaks in the thermoluminescence glow curve, thermal gradients in the samples precluded the possibility of kinetic analysis of the phase transitions by this technique. The results should, however, be a valuable guide for any subsequent studies of thermoluminescence in bulk specimens or single crystals.

REFERENCES

1. A. D. Buckingham and B. D. Utting, Ann. Rev . Phys. Chem. 21, 287 (1970).
2. A. D. Buckingham, Discuss. Faraday Soc. 40, 232 (1965).
3. A. D. Buckingham, Adv. Chem. Phys. 12, 107 (1967).
4. A. D. Buckingham, Phil. Trans. Roy. Soc. Lond. B272, 5 (1975).
5. A. Dalgarno, Adv. Chem. Phys. 12, 143 (1967).
6. F. London, Trans. Faraday Soc. 33, 8 (1937).
7. D. Halliday and R. Resnick, Fundamentals of Physics, John Wiley and Sons, Inc., New York (1970).
8. J. O. Hirschfelder, C. F. Curtiss and R. B. Bird, Molecular Theory of Gases and Liquids, John Wiley and Sons, Inc., New York (1954).
9. B. M. Axilrod and E. Teller, J. Chem. Phys. 11, 299 (1943).
10. R. A. Aziz and H. H. Chen, J. Chem. Phys. 67, 5719 (1977).
11. S. A. Rice and P. Gray, Statistical Mechanics of Simple Liquids, Interscience, New York (1965).
12. J. A. Barker and D. Henderson, Ann. Rev . Phys. Chem. 23, 439 (1972).
13. D. Chandler, J. Chem. Phys. 60, 3500 (1974).
14. D. Chandler, J. Chem. Phys. 62, 1358 (1975).
15. A. I. Kitaigorodskii, Molecular Crystals and Molecules, Academic Press, New York (1973).

16. D. E. Williams, J. Chem. Phys. 45, 3770 (1966).

17. H. M. James and T. A. Keenan, J. Chem. Phys. 31, 12 (1959).

18. J. Timmermans, J. Chim. Phys. 35, 331 (1938).

19. W. Mandema and N. J. Trappeniers, Physica 76, 73 (1974).

20. K. H. Michel, J. Chem. Phys. 58, 142 (1973).

21. K. H. Michel, J. Chem. Phys. 58, 1143 (1973).

22. L. Pauling, Phys. Rev. 36, 430 (1930).

23. H. F. King and D. F. Hornig, J. Chem. Phys. 44, 4520 (1966).

24. S. C. Jain and V. K. Tewary, J. Phys. C6, 1999 (1973).

25. See F. Lüty, Phys. Rev. B10, 3667 (1974) and references therein.

26. W. E. Bron and R. W. Dreyfus, Phys. Rev. 163, 304 (1967).

27. R. Windheim and H. Kinder, Phys. Lett. 51A, 475 (1975).

28. H. Glättli, A. Sentz and M. Eisenkremer, Phys. Rev. Lett. 28, 871 (1972).

29. W. Press and A. Kollmar, Solid State Commun. 17, 405 (1975).

30. B. Alefeld, A. Kollmar and B. Dasannacharya, J. Chem. Phys. 63, 4415 (1975).

31. A. Hüller and D. M. Kroll, J. Chem. Phys. 63, 4495 (1975).

32. I. N. Levine, Quantum Chemistry, Allyn and Bacon, Inc., Boston, 2nd edition (1974).

33. L. D. Landau and E. M. Lifshitz, Quantum Mechanics, Addison Wesley Ltd., Reading, Mass. (1958).

34. K. Clusius, Z. Physik. Chem. B3, 41 (1929).

35. A. Kruis, L. Popp and K. Clusius, Z. Elektrochem. 43, 664 (1937).

36. K. Clusius and L. Popp, Z. Physik. Chem. B46, 63 (1940).

37. E. Bartholomé, G. Drikos and A. Eucken, Z. Physik. Chem. B39, 371 (1938).

38. A. Sperandio, Ph.D. Thesis, University of Zurich (1961).

39. J. H. Colwell, E. K. Gill and J. A. Morrison, J. Chem. Phys. 39, 635 (1963).

40. D. R. Aadsen, Ph.D. Thesis, University of Illinois (1975).

41. D. R. Baer, B. A. Fraas, D. H. Riehl and R. O. Simmons, J. Chem. Phys. 68, 1411 (1978).

42. Private communication from 1963 work of Colwell, Gill and Morrison[39].

43. O. Trapeznikowa and G. A. Miljutin, Nature 144, 632 (1939).

44. R. Stevenson, J. Chem. Phys. 27, 656 (1957).

45. J. W. Stewart, J. Phys. Chem. Solids 12, 122 (1959).

46. A. J. Nijman, Ph.D. Thesis, University of Amsterdam (1977).

47. M. S. Constantino and W. B. Daniels, J. Chem. Phys. 62, 764 (1975).

48. A. Schallamach, Proc. Roy. Soc. A171, 569 (1939).

49. J. T. Thomas, N. L. Alpert and H. C. Torrey, J. Chem. Phys. 18, 1511 (1950).

50. M. F. Crawford, H. L. Welsh and J. H. Harrold, Can. J. Phys. 30, 81 (1952).

51. G. E. Ewing, J. Chem. Phys. 40, 179 (1964).

52. A. Anderson and R. Savoie, J. Chem. Phys. 43, 3468 (1965).

53. H. Kapulla and W. Glässer, in Inelastic Scattering of Neutrons in Solids and Liquids, IAEA, Vienna, p.841 (1973).

54. W. Press, J. Chem. Phys. 56, 2597 (1972).

55. A. A. Thiele, W. M. Whitney and C. E. Chase, Low Temperature Physics, LT9, J. G. Daunt et al. eds., Plenum Press, Inc., New York, Pt. B, p. 1122 (1965).

56. G. A. de Wit and M. Bloom, Can. J. Phys. 47, 1195 (1969).

57. D. N. Bol'shutkin, V. M. Gasan, A. I. Prokhvatilov and A. I. Érenburg, Zhur. Strukt. Khim. 12, 336 (1971). (J. Struct. Chem. 12, 313 (1971).)

58. W. Press, B. Dorner and G. Will, Phys. Lett. 31A, 253 (1970).

59. W. F. Giauque, R. W. Blue and R. Overstreet, Phys. Rev. 38, 196 (1931).

60. A. Frank and K. Clusius, Z. Physik. Chem. B36, 291 (1937).

61. J. H. Colwell, E. K. Gill and J. A. Morrison, J. Chem. Phys. 36, 2223 (1962).

62. R. P. Wolf and W. M. Whitney, Proceedings of the Ninth Low Temperature Conference, Plenum Press, New York p. 1118 (1965).

63. H. P. Hopkins, Jr., P. L. Donoho and K. S. Pitzer, J. Chem. Phys. 47, 864 (1967).

64. K. P. Wong, J. D. Noble, M. Bloom and S. Alexander, J. Magn. Resonance 1, 55 (1969).

65. P. van Hecke, P. Grobert and L. van Gerven, J. Magn. Resonance 7, 117 (1972).

66. G. J. Vogt and K. S. Pitzer, J. Chem. Thermodynamics 8, 1011 (1976).

67. E. B. Wilson, Jr., J. Chem. Phys. 3, 276 (1935).

68. R. F. Code and J. Higinbotham, Can. J. Phys. 54, 1248 (1976).

69. K. J. Lushington and J. A. Morrison, Can. J. Phys. 55, 1580 (1977).

70. E. A. Ballik, D. J. Gannon and J. A. Morrison, J. Chem. Phys. 58, 5639 (1973).

71. W. Press and A. Hüller, Proceedings of the NATO Advanced Study Institute on Anharmonic Lattices, Structural Phase Transitions and Melting, Geilo, Norway, 1973, T. Riste ed., Noordhoff, Leiden, p. 185 (1974).

72. E. Arzi and E. Sándor, Acta Cryst. A31, S188 (1975).

73. K. Clusius, L. Popp and A. Frank, Physica 4, 1105 (1937).

74. J. H. Colwell, E. K. Gill and J. A. Morrison, J. Chem. Phys. 42, 3144 (1965).

75. W. Schottky, Physik. Z. 23, 448 (1922).

76. J. H. Colwell, J. Chem. Phys. 51, 3820 (1969).

77. T. Nagamiya, Prog. Theor. Phys. 6, 702 (1951).

78. J. Higinbotham, R. F. Code and B. M. Wood, Phys. Rev. B14, 4773 (1976).

79. K. J. Lushington and J. A. Morrison, J. Chem. Phys. 69, 4214 (1978).

80. J. A. Morrison and P. R. Norton, J. Chem. Phys. 56, 1457 (1972).

81. E. P. Jones, J. A. Morrison and E. L. Richards, Can. J. Phys. 53, 2546 (1975).

82. T. Yamamoto and Y. Kataoka, J. Chem. Phys. 48, 3199 (1968).

83. T. Yamamoto and Y. Kataoka, Phys. Rev. Lett. 20, 1 (1968).

84. Y. Kataoka and T. Yamamoto, Prog. Theor. Phys. Suppl. 436 (1968).

85. H. Yasuda, T. Yamamoto and Y. Kataoka, Prog. Theor. Phys. 41, 859 (1969).

86. K. Nishiyama, Y. Kataoka and T. Yamamoto, Prog. Theor. Phys. 43, 1121 (1970).

87. T. Yamamoto and Y. Kataoka, Prog. Theor. Phys. 46, Suppl., 383 (1970).

88. D. C. Heberlein and E. D. Adams, J. Low Temp. Phys. 3, 115 (1970).

89. T. Yamamoto, Y. Kataoka and K. Okada, J. Chem. Phys. 66, 2701 (1977).

90. Y. Kataoka, Prog. Theor. Phys. 43, 1132 (1970).

91. A. Cabana, G. B. Savitsky and D. F. Hornig, J. Chem. Phys. 39, 2942 (1963).

92. H. Yasuda, Prog. of Theor. Phys. 45, 1361 (1971).

93. L. S. Bartell, J. Chem. Phys. 32, 827 (1960).

94. J. B. Hendrickson, J. Am. Chem. Soc. 83, 4537 (1961).

95. A. I. Kitaigorodskii, Tetrahedron 14, 230 (1961).

96. A. I. Kitaigorodskii and K. V. Mirskaya, Soviet Phys. Cryst. 6, 408 (1962).

97. K. Maki, Y. Kataoka, K. Okada and T. Yamamoto, Soviet J. Low Temp. Phys. 1, 348 (1975).

98. Y. Kataoka, K. Okada and T. Yamamoto, Chem. Phys. Lett. 19, 365 (1973).

99. K. Nishiyama and T. Yamamoto, J. Chem. Phys. 58, 1001 (1973).

100. A. Chamberland, R. Belzile and A. Cabana, Can. J. Chem. 48, 1129 (1970).

101. K. Kobashi, Y. Kataoka and T. Yamamoto, Can. J. Chem. 54, 2154 (1976).

102. C. Chapados and A. Cabana, Can. J. Chem. 50, 3521 (1972).

103. B. Dorner and H. Stiller, Inelastic Scattering of Neutrons, Vol. 2, IAEA, Vienna, p. 291 (1965).

104. Y. D. Harker and R. M. Brugger, J. Chem. Phys. 46, 2201 (1967).

105. H. Kapulla and W. Gläser, Phys. Lett. 31A, 153 (1970).

106. Ö. Runolfsson and S. Mango, Phys. Lett. 28A, 254 (1968).

107. H. Glättli and A. Sentz in Magnetic Resonance and Related Phenomena, ed.V. Hovi, North-Holland, Amsterdam,p.212(1973).

108. R. Kahn, Phys. Lett. 54A, 285 (1975).

109. The T splitting is calculated to be 0.01K.[89]

110. K. Maki, Y. Kataoka, K. Okada and T. Yamamoto, Acta Cryst. A31, S188 (1975).

111. K. Maki, Y. Kataoka and T. Yamamoto, J. Chem. Phys.70, 655 (1979).

112. Y. A. Sataty, A. Ron and F. H. Herbstein, J. Chem. Phys. 62, 1094 (1975).

113. M. Atoji and W. N. Lipscomb, Acta. Cryst. 7, 597 (1954).

114. M. A. White, K. J. Lushington and J. A. Morrison, J. Chem. Phys. 69, 4227 (1978).

115. F. D. Medina and W. B. Daniels, J. Chem. Phys. 70, 2688 (1979).

116. J. Obriot, F. Fondère, Ph. Marteau, H. Vu and K. Kobashi, Chem. Phys. Lett. 60, 90 (1978).

117. P. L. Gant and K. Yang, J. Am. Chem. Soc. 86, 5063 (1964).

118. A. Di Corcia, D. Fritz and F. Bruner, J. Chromatog. 53, 135 (1970).

119. P. R. Norton, J. Chromatog. Sci. 8, 411 (1970).

120. A. Di Corcia and F. Bruner, J. Chromatog. 49, 139 (1970).

121. L. Szepesy, Gas Chromatography, Iliffe Books Ltd., and Publishing House of the Hungarian Academy of Sciences, Budapest (1970).

122. Private communication from F. Bruner (1976).

123. H. S. Sandhu, J. Lees and M. Bloom, Can. J. Chem. 38, 493 (1960).

124. G. T. Armstrong, F. G. Brickwedde and R. B. Scott, J. Research Nat. Bur. Stand. 55, 39 (1955).

125. S. H. Castles and E. D. Adams, Phys. Rev. Lett. 30, 1125 (1973).

126. M. A. White and J. A. Morrison, Phys. Rev. Lett. 40, 1574 (1978).

127. M. A. White and J. A. Morrison, J. Chem. Phys. 70, 5384 (1979).

128. Private communication from E. D. Adams in Ref. 79.

129. O. P. Bansal, J. A. Morrison and E. L. Richards, Z. Physik. B32, 379 (1979).

130. M. F. Wood, Advanced Cryogenics, C. A. Bailey ed., Plenum, New York, p. 245 (1971).

131. G. K. White, Experimental Techniques in Low Temperature Physics, Oxford University Press, Oxford, 2nd. edition (1968).

132. T. H. Frederking, Chem. Eng. Prog. Symp., Ser. 64, No. 87, 21 (1968).

133. T. H. K. Barron and J. A. Morrison, Can. J. Phys. 35, 799 (1957).

134. J. G. Aston and J. J. Fritz, Thermodynamics and Statistical Thermodynamics, John Wiley and Sons, Inc., New York (1959).

135. M. Blackman in Handbuch der Physik, Vol. VII, pt. 1, Crystal Physics, ed. by S. Flügge, Springer-Verlag, Berlin, p. 325 (1955).

136. Derived in Ref. 76 from the data of Ref. 39.

137. T. L. Hill, Introduction to Statistical Thermodynamics, Addison-Wesley, Reading (1960).

138. H. P. Hopkins, Jr., J. V. V. Kasper, K. S. Pitzer, J. Chem. Phys. 46, 218 (1967).

139. M. Bloom and J. A. Morrison, in Surface and Defect Properties of Solids, Specialist Periodical Reports of The Chemical Society, Vol. 2, p. 140 (1973).

140. A. J. Nijman and A. J. Berlinsky, Phys. Rev. Lett. 38, 408 (1977).

141. Private communication from M. Bloom (1978).

142. Based on an unpublished relaxation time of $\sim$ 40 days for CH_4 in phase III, as measured by A. J. Nijman, and privately communicated by R. F. Code (1978).

143. M. Bloom, P. Beckmann and B. C. Sanctuary, Can. J. Phys. 54, 2209 (1976).

144. The contribution to the entropy at T = 0K due to different molecular field symmetries was first considered by Vogt and Pitzer[66] for CH_4.

145. E. S. R. Gopal, Specific Heats at Low Temperatures, Plenum Press, New York (1966).

146. Private communication from A. Hüller (1979).

147. Private communication from W. Press (1979).

148. M. W. Newbery, T. Rayment, M. V. Smalley, R. K. Thomas and J. W. White, Chem. Phys. Lett. 59, 461 (1978).

149. T. G. Gibbons and M. L. Klein, J. Chem. Phys. 60, 112 (1974).

150. K. Kobashi, M. L. Klein and V. Chandrasekharan, J. Chem. Phys. 71, 843 (1979).

151. S. F. O'Shea, J. Chem. Phys. 68, 5435 (1978).

152. D. Curie, Luminescence Cristalline, Dunod, Paris (1960).

153. G. F. J. Garlick in Handbuch der Physik, Springer-Verlag, Berlin, 26, p. 1 (1958).

154. F. Kieffer and M. Magat in Actions Chimiques et Biologiques des Radiations, Vol. 14, ed. by M. Haissinsky, Masson, Paris, p. 135 (1970).

155. G. N. Lewis and J. Bigeleisen, J. Amer. Chem. Soc. 65, 2424 (1943).

156. P. Debye and J. O. Edwards, Science 116, 143 (1952).

157. P. Debye and J. O. Edwards, J. Chem. Phys. 20, 236 (1952).

158. W. A. Gibbons, G. Porter and M. I. Savadatti, Nature 206, 1355 (1965).

159. J. T. Randall and M. H. F. Wilkins, Proc. Roy. Soc. A184, 366 (1945).

160. J. Kroh, J. Mayer, W. Roszak, Z. Galdecki, Z. Górkiewicz and B.Ptaszyński, Int. J. Radiat. Phys. Chem. 5, 59 (1973).

161. J. Kroh and J. Mayer, Int. J. Radiat. Phys. Chem. 6, 423 (1974).

162. I. Sugawara and Y. Tabata, Chem. Phys. Lett. 41, 357 (1976).

163. J. Bullot, A. Déroulède and F. Kieffer, J. Chim. Phys. 63, 150 (1966).

164. M. R. Wright, R. P. Frosch and G. W. Robinson, J. Chem. Phys. 33, 934 (1960).

165. J. Bullot and A. C. Albrecht, J. Chem. Phys. 51, 2220 (1969).

166. J. B. Gallivan and W. H. Hamill, J. Chem. Phys. 44, 1279 (1966).

167. T. Sawai , J. Nucl. Sci. Tech. 8, 431 (1971).

168. F. Kieffer, C. Meyer and J. Rigaut, Chem. Phys. Lett. 11, 359 (1971).

169. J. Moan, J. Lumin. 6, 256 (1973).

170. F. Kieffer, N. V. Klassen and C. Lapersonne-Meyer, J. Lumin. 20, 17 (1979).

171. H. Schwartz in Proceedings of the First International Conference on Electron and Ion Beam Science and Techno-

171. logy, ed. by R. Bakish, John Wiley and Sons, Inc., New York, p. 158 (1965).

172. R. J. Fleming, J. Polym. Sci. A-2, 6, 1283 (1968).

173. O. Haida, H. Suga and S. Seki, Thermochim. Acta 3, 177 (1972).

174. I. Boustead and A. Charlesby, Proc. Roy. Soc. Lond. A315, 271 (1970).

175. L. F. Pender and R. J. Fleming, J. Phys. C10, 1571 (1977).